Mapping Age- and ALS-Related Changes in the Sensorimotor Cortex with Multivariate 7T-fMRI Analyses

Dissertation

zur Erlangung des Grades eines
Doktors der Naturwissenschaften

der Mathematisch-Naturwissenschaftlichen Fakultät
und
der Medizinischen Fakultät
der Eberhard-Karls-Universität Tübingen

vorgelegt
von

Avinash Kalyani
aus Narar, Indien

2025

Tag der mündlichen Prüfung: 20.10.2025

Dekan der Math.-Nat. Fakultät: Prof. Dr. Thilo Stehle
Dekan der Medizinischen Fakultät: Prof. Dr. Bernd Pichler

1. Berichterstatter: Prof. Dr. Esther Kuehn
2. Berichterstatter: Prof. Dr. Oliver Speck

Prüfungskommission: Prof. Dr. Esther Kuehn
PD Dr. Marc Himmelbach
Prof. Dr. Martin Giese
Prof. Dr. Oliver Speck

Erklärung / Declaration:

Ich erkläre, dass ich die zur Promotion eingereichte Arbeit mit dem Titel:

"Mapping Age- and ALS-Related Changes in the Sensorimotor Cortex with Multivariate 7T-fMRI Analyses"

selbständig verfasst, nur die angegebenen Quellen und Hilfsmittel benutzt und wörtlich oder inhaltlich übernommene Stellen als solche gekennzeichnet habe. Ich versichere an Eides statt, dass diese Angaben wahr sind und dass ich nichts verschwiegen habe. Mir ist bekannt, dass die falsche Abgabe einer Versicherung an Eides statt mit Freiheitsstrafe bis zu drei Jahren oder mit Geldstrafe bestraft wird.

I hereby declare that I have produced the work entitled "Mapping Age- and ALS-Related Changes in the Sensorimotor Cortex with Multivariate 7T-fMRI Analyses", submitted for the award of a doctorate, *on my own (without external help), have used only the sources and aids indicated and have marked passages included from other works, whether verbatim or in content, as such. I swear upon oath that these statements are true and that I have not concealed anything. I am aware that making a false declaration under oath is punishable by a term of imprisonment of up to three years or by a fine.*

Tübingen, den ....

Datum / Date Unterschrift / Signature

Declaration of Contributions to the Dissertation:

The dissertation work was carried out at the Otto-von-Guericke University Magdeburg and the Graduate Training Centre of Neuroscience of the Eberhard-Karls-Universität Tübingen under the supervision of Prof. Dr. Esther Kuehn.

Chapter 4: Functional Changes in Aging

Study design: The study design was developed by Prof. Dr. Esther Kuehn as part of a larger cohort dataset (SenseMap Project).

Data acquisition: The data was collected as part of the SenseMap Project prior to the start of my involvement.

Analysis strategy: The data analysis strategy was developed by me with support from Prof. Dr. Esther Kuehn, Oliver Contier, and Dr. Christoph Reichert.

Formal analyses: I performed all data preprocessing, statistical analyses, and figure preparation independently.

Writing and editing: I wrote the manuscript draft and adapted the figures and results in this chapter from the published version in *NeuroImage* (2023; DOI: 10.1016/j.neuroimage.2023.120430), with editorial contributions from: Oliver Contier, Lisa Klemm, Dr. Elena Azañon, Prof. Dr. habil. Stefanie Schreiber, Prof. Dr. Oliver Speck, Dr. Christoph Reichert, and Prof. Dr. Esther Kuehn.

Chapter 5: Amyotrophic Lateral Sclerosis-Related Functional Changes

Study design: The study design was developed by Dr. Alicia Northall, Prof. Dr. habil. Stefanie Schreiber, and Prof. Dr. Esther Kuehn.

Data acquisition: The data was acquired by Alicia Northall, Jascha Brüggemann, Prof. Dr. habil. Stefanie Schreiber, Dr. Stefan Vielhaber, Marwa Al Dubai, and Abrar Benramadan.

Analysis strategy: The data analysis strategy was conceptualized by me with input from Prof. Dr. Esther Kuehn.

Formal analyses: I performed all data preprocessing, statistical modeling, and figure preparation.

Writing and editing: I wrote the manuscript draft and adapted the figures and results in this chapter from the paper now provisionally accepted for publication in *Brain Communications* (2025), which was previously available as a preprint on *bioRxiv*, with editorial contributions from Dr. Alicia Northall, Prof. Dr. habil. Stefanie Schreiber, Prof. Dr. Oliver Speck, Dr. Hendrik Mattern, Dr. Christoph Reichert, and Prof. Dr. Esther Kuehn.

I confirm that I wrote the original drafts of both manuscripts myself, under the supervision of Prof. Dr. Esther Kuehn, and that any additional sources of information have been duly cited.

I would like to dedicate this thesis to my loving parents ...

Acknowledgements

First and foremost, I want to express my deepest gratitude to my supervisor, Prof. Dr. Esther Kuehn. Esther, you've been an incredible mentor. Whenever I felt lost in the details of my research, you were there to help me see the bigger picture. Your patience, understanding, and constant belief in me made all the difference. Thank you for everything.

I also extend my heartfelt thanks to Dr. Christoph Reichert. Your willingness to accommodate last-minute meetings and discussions, coupled with your invaluable methodological insights and constructive feedback, were crucial to my work. Your support and guidance throughout this journey are truly appreciated.

I am grateful to my thesis committee members, Prof. Dr. Oliver Speck and Prof. Dr. Martin Giese, for their valuable feedback and support during my PhD journey.

To my "three Musketeers"—my colleagues and now lifelong friends—Alicia Northall and Peng Liu: thank you. You became my family here, and your support made the tough times of the PhD so much easier to bear. I'm so grateful for our friendship.

A big thank you to Julianne Doehler, Susanne Stoll, and Christoph Knoll for teaching me something new every day. Susanne, I especially loved our brainstorming sessions and hope we can keep that going!

To my friend and sister, Anwesha, thanks for all the coffee, the lunches we cooked, and for always being there to listen to my rants. Bankim, thanks for being a great friend and for stepping up as a mentor when I really needed it. Aditya, thank you for all the weekend machine learning sessions, I learned a lot from you.

I would also like to thank my friends back home especially Olga, and Lokesh, who have been my pillars of support. Your encouragement and belief in me have been invaluable.

Finally, I want to thank my mum, Nilesh Singh, and dad, Vimal Kumar Singh, my first teachers. Mum, I learned to be brave from you, and Dad, to stay humble, grateful, and work hard. You've always taught me to be strong and never give up. Seeing how proud you are of even my smallest achievements truly motivates me. And to my sister, Stuti, thanks for just being you and for teaching me to go easy on myself sometimes.

And, to everyone else who supported me along the way, thank you. Your encouragement meant the world, and I appreciate everything you've done.

Abstract

Functional Magnetic Resonance Imaging (fMRI), particularly at ultra-high-field strengths such as 7-Tesla (7T), has revolutionized neuroscience by enabling detailed exploration of the human brain's functional architecture. This thesis leverages the advanced spatial resolution of 7T-fMRI to investigate the sensorimotor cortex, focusing on age-related changes and disease-specific alterations associated with Amyotrophic Lateral Sclerosis (ALS). While the unprecedented resolution of 7T-fMRI allows for the analysis of fine-grained features, such as cortical columns and laminar structures, the high dimensionality and complexity of the data necessitate sophisticated analytical methods.

This work employs 7 T task-based fMRI with advanced multivariate techniques, including Robust Shared Response Modeling (rSRM), Columnar Shared Response Modeling (C-SRM) (introduced as a novel method), and Partial Least Squares Regression (PLSR), to address the challenges posed by high-dimensional fMRI data. SRM and C-SRM are utilized to align functional data across participants and examine fine-scale neural organization, particularly at the columnar level, while PLSR links neural activity to clinical and behavioral outcomes. These approaches enable the identification of both shared and individual-specific neural patterns, offering a nuanced understanding of functional changes in the sensorimotor cortex.

In the context of aging, rSRM and C-SRM show that the hierarchical layout of Brodmann areas (BA) 3b $\rightarrow$ 1 $\rightarrow$ 2 is preserved in older adults, yet digit representations become less precise. In BA1, the optimal number of functional columns drops relative to young adults, indicating enlarged, less selective columns; while BA3b remains stable. These findings reveal a subtle dedifferentiation—blurred maps but an intact hierarchy—consistent with compensatory pooling of sensory inputs.

In ALS, rSRM combined with PLSR distinguishes patients from controls with high accuracy based on task-evoked BOLD patterns. Connectivity-derived latent variables outperform activation maps in clustering disease onset site and staging, and they exhibit an *atopographic* signature: foot and face regions of MI track progression regardless of the initial symptom locus. The data suggest an early, network-wide hyper-connective compensation that collapses as degeneration advances.

Together, these results validate advanced alignment and dimensionality-reduction strategies for extracting fine grained insights from 7 T data. They establish enlarged columns as a fingerprint of healthy ageing and identify network-level connectivity markers for ALS staging—outcomes that

can guide larger multicentre, multimodal studies and inform therapeutic efforts aimed at preserving sensorimotor function across the lifespan and in neurodegenerative disease.

Table of contents

List of figures

List of tables

Abbreviations

Acronyms

SII	Secondary Somatosensory Cortex
AA	Anatomical Alignment
ALS	Amyotrophic Lateral Sclerosis
ALSFRS-R	ALS Functional Rating Scale Revised
ANOVA	Analysis of Variance
BA	Brodmann Areas
BOLD	Blood Oxygenation Level Dependent
C-SRM	Columnar Shared Response Model
cSRM	Connectivity Shared Response Modeling
DTI	Diffusion Tensor Imaging
EEG	Electroencephalogram
EPI	Echo-Planar Imaging
fMRI	Functional Magnetic Resonance Imaging
GE-EPI	Gradient Echo-EPI
GLM	General Linear Model
ICA	Independent Component Analysis
LMN	Lower Motor Neuron

LOSO	Leave-One-Subject-Out
MI	Primary Motor Cortex
MRI	Magnetic Resonance Imaging
MVPA	Multivoxel Pattern Analysis
PCA	Principal Component Analysis
PE	Phase-Encoding
PLSR	Partial Least Squares Regression
PRF	Population Receptive Field
PSF	Point Spread Function
PUMNS	Penn Upper Motor Neuron Score
ROI	Regions of Interest
rSRM	Robust Shared Response Model
SD	Standard Deviation
SEM	Standard Error of Mean
SI	Primary Somatosensory Cortex
SMS	Simultaneous Multi-Slice
SNR	Signal to Noise Ratio
SRM	Shared Response Model
sSRM	Searchlight Shared Response Modeling
SVM	Support Vector Machine
SWI	Susceptibility-Weighted Imaging
T	Tesla
TMS	Transcranial Magnetic Stimulation
UHF	Ultra High Field
UMN	Upper Motor Neuron

Chapter 1

Overview

1.1 Thesis Rationale

Understanding how the human sensorimotor system reorganizes in response to aging and neurodegeneration remains a central question in cognitive and clinical neuroscience. Over the past decades, numerous structural and functional imaging studies have provided insights into age- and disease-related alterations in the brain [58, 57, 71]. Structural magnetic resonance imaging (MRI) findings have consistently documented cortical thinning, changes in gyrification, and white matter degeneration across both normal aging and neurodegenerative disorders such as Amyotrophic Lateral Sclerosis (ALS) [58, 105, 22]. Functional imaging, predominantly using resting-state functional-MRI (fMRI), has further revealed disruptions in large-scale brain networks, including the sensorimotor, default mode, and frontoparietal systems [97, 98, 104]. These findings have significantly advanced theoretical models of dedifferentiation, compensation, and network-level reorganization in aging and disease.

However, a major limitation in the current literature is the predominance of resting-state functional imaging, which—although valuable for capturing intrinsic connectivity—lacks the spatial and temporal specificity to probe how specific sensorimotor processes are affected. Resting-state paradigms often conflate task-irrelevant fluctuations with meaningful reorganization, and they cannot directly capture how the brain responds to external stimuli or performs motor/sensory tasks. This is particularly limiting when studying fine-grained somatotopic representations and dynamic functional responses, which are crucial for understanding subtle sensorimotor dysfunction. For example, a study [87] focused on the functional characterization of the motor cortex, found that the sensitivities of resting-state and task-based fMRI were comparable, but with a good spatial correspondence with the task-based fMRI activity estimates.This suggests that task-based fMRI may be more sensitive to the specific functional organization of the sensorimotor system, as it directly engages the neural circuits involved in sensory and motor processing.

In light of this gap, the present thesis aims to directly investigate sensorimotor cortical function in aging and ALS by leveraging task-based fMRI at ultra-high-field (UHF) (7 Tesla (T)). By moving beyond passive resting scans to active task paradigms, this approach enables assessment of how neural circuits respond during actual motor and sensory behavior, providing more direct insight into sensorimotor processing deficits. Specifically, a set of simple sensorimotor tasks is employed to engage multiple aspects of the sensorimotor system, including tactile processing and motor execution, in two separate studies. This allows for a more nuanced understanding of how aging and ALS affect the organization and dynamics of sensorimotor networks.

UHF fMRI offers unprecedented spatial resolution and sensitivity for mapping the human sensorimotor system [42]. At 7T, neural representations can be resolved at a mesoscopic scale that remains blurred at lower field strengths. For example, high-resolution 7T fMRI can delineate separate representations for individual fingers within primary somatosensory cortex (SI) [90, 57, 106, 49] and has even revealed columnar patterns of tactile input processing in area 3b of SI [39, 110]. This fine-grained imaging capability is critical for detecting subtle somatotopic reorganizations or losses of specificity that may accompany aging and early neurodegeneration [42].

While UHF imaging dramatically enhances spatial resolution, it also introduces analytical challenges (i.e.*with great detail comes great complexity*). The 7T datasets are exceedingly high-dimensional (due to smaller voxels and larger image matrices) and can suffer from increased physiological noise and variability. For instance, physiological fluctuations and motion artifacts contribute substantially to signal variance at 7T [81], and inter-subject differences in functional connectivity patterns can become more pronounced at higher field strength [50]. Extracting meaningful information from such complex data therefore requires advanced multivariate analysis techniques. Accordingly, this thesis applies sophisticated multivariate methods to the 7T fMRI results to improve sensitivity to distributed activation patterns and subtle changes that might evade conventional univariate analyses [96]. By combining UHF imaging with robust data-driven analytics, the work aims to achieve a more nuanced characterization of sensorimotor cortical dysfunction in aging and ALS. This rationale thus lays the foundation for the specific aims and hypotheses addressed in the following section.

1.2 Thesis Aims and Hypotheses

Building on the above motivation, the central aim of this thesis is to combine UHF (7T) fMRI with advanced multivariate analysis techniques in order to deepen our understanding of fine-grained sensorimotor cortical organization and how it is altered by both healthy aging and ALS. In particular, the work seeks to develop and apply novel analytical methods to 7T fMRI datasets to characterize fine-scale sensorimotor maps and their changes in aging and disease. By linking these cutting-edge

tools with key neuroscientific questions, this research demonstrates how high-resolution imaging coupled with tailored data analysis can reveal new insights into sensorimotor function and improve the detection of meaningful neural patterns amid complex, high-dimensional data.

To address this aim, a series of specific hypotheses were formulated, focusing on how aging and ALS affect sensorimotor representations and what analytical approaches can best capture these effects :

1. **Study 1: Aging in Somatosensory Cortex**

    - *H1: Aging diminishes representational precision of digit maps in SI.* Older adults will display less distinct, more diffuse digit representations in Brodmann Areas (BA) 1 and 3b compared to younger adults, due to the age-related decline in inhibitory processing of tactile inputs.
    - *H2: Aging widens columnar-scale organization in SI.* Older adults will engage fewer cortical columns for each digit's representation, exhibiting broader tuning that is consistent across BA1 and BA3b.
    - *H3: Robust Shared Response Modeling (rSRM) enhances inter-subject comparisons over conventional preprocessing.* rSRM will outperform anatomical alignment in digit classification accuracy across age groups, especially in BA1 and BA3b, with reduced Euclidean distances between neighboring digit representations in older adults.

2. **Study 2: ALS-Related Functional Disruptions**

    - *H4: (a)ALS patients are distinguishable from healthy controls by sensorimotor activity patterns, (b)led by the first-affected region.* rSRM-based classification will separate ALS patients from healthy controls, with the initial affected region yielding the highest classification scores.
    - *H5: Connectivity outperforms activation in Modeling ALS severity.* Connectivity matrices in ALS patients will correlate more strongly with ALSFRS-R scores than activation patterns assessed using PLSR.

These hypotheses drive the experimental studies in later chapters. Chapter 4 focuses on healthy aging, employing high-resolution 7T fMRI with rSRM and columnar-SRM (C-SRM) analyses to test H1–H3 by examining age-related changes SI digit maps and columnar organization. Chapter 5 is devoted to ALS, using Partial Least Squares Regression (PLSR) and connectivity analyses to test H4–H5 by comparing patients and controls and linking brain measures to clinical scores. Together, these studies illustrate the power of advanced multivariate methods in leveraging 7T-fMRI's spatial

detail to reveal sensorimotor cortical alterations in aging and disease. In the next chapter, we detail the theoretical background and methodological frameworks that underlie these experiments, before presenting the results of the aging (Chapter 4) and ALS (Chapter 5) studies.

1.3 Organization and Contribution of the Thesis

Following this introduction, the thesis is organized into several chapters, each addressing a specific set of questions and collectively advancing the overarching aim. **Chapter 2** provides a broad literature review of the sensorimotor system and its perturbations in aging and ALS. It covers the anatomical and functional organization of primary sensorimotor cortices, surveys known age-related changes in sensorimotor function, and reviews the neuropathology and prior imaging findings in ALS. This background establishes the context and rationale for the subsequent experimental work. **Chapter 3** then introduces the methodological frameworks employed in this thesis. In particular, it details the multivariate analysis techniques – notably the Shared Response Model (SRM) and PLSR – that are applied to the 7T fMRI data. By explaining these tools, Chapter 3 provides the necessary foundation for understanding how we handle the high-dimensional neural data. **Chapter 4** presents the first empirical study, focusing on healthy aging. Using high-resolution 7T fMRI in combination with SRM and a novel columnar-SRM approach, this chapter investigates how aging affects fine-grained SI representations (testing H1–H3). **Chapter 5** is devoted to the ALS study, examining how functional brain measures relate to clinical state in ALS. Here, PLSR and connectivity analyses are used to test H4–H5, evaluating whether brain connectivity changes serve as biomarkers of ALS severity. **Chapter 6** concludes the thesis with a general discussion, synthesizing the findings from both studies, considering their theoretical and clinical implications, and outlining directions for future research. Overall, each chapter contributes a vital piece to the dissertation's goal of mapping and understanding age- and ALS-related changes in the sensorimotor cortex with advanced 7T-fMRI analytics.

Chapter 2

General Introduction

2.1 Sensorimotor System : Primary Somatosensory(SI) and Motor Cortex(MI)

The execution and perception of movement in humans rely fundamentally on the tightly integrated functions of the SI and the primary motor cortex (MI). These two critical cortical regions are situated on opposing banks of the central sulcus: SI resides in the postcentral gyrus of the parietal lobe, while MI occupies the precentral gyrus in the frontal lobe [74]. A defining characteristic of both areas is their striking *somatotopic* organization, famously depicted by the sensory and motor homunculi (Figure 2.1), which represent the body's surface and musculature across the cortical sheet [47]. This mapping is not a simple reflection of physical size; instead, the cortical territory allocated to a body part is proportional to the density of its sensory innervation (in SI) or the precision of its motor control (in MI). Consequently, areas like the hands, fingers, lips, and tongue command disproportionately large cortical representations due to their functional significance in fine manipulation and communication [74].

Anatomically, SI is subdivided into BA3a, BA3b, BA1, and BA2, each receiving specific thalamic inputs and contributing to a detailed somatosensory map. Area 3b is a primary tactile receiving area, while BA3a is more responsive to proprioception. Areas 1 and 2 process higher-order features like texture, size, and shape [47, 43]. These subdivisions are arranged in parallel, creating multiple representations of the body within SI. MI (BA-4) is characterized by large Betz cells in layer V, which project directly to spinal motor neurons. While famously mapped via stimulation, the motor map exhibits more overlap and distributed networks than often portrayed, particularly for complex movements [74]. The functional integration of SI and MI is further facilitated by shared inputs

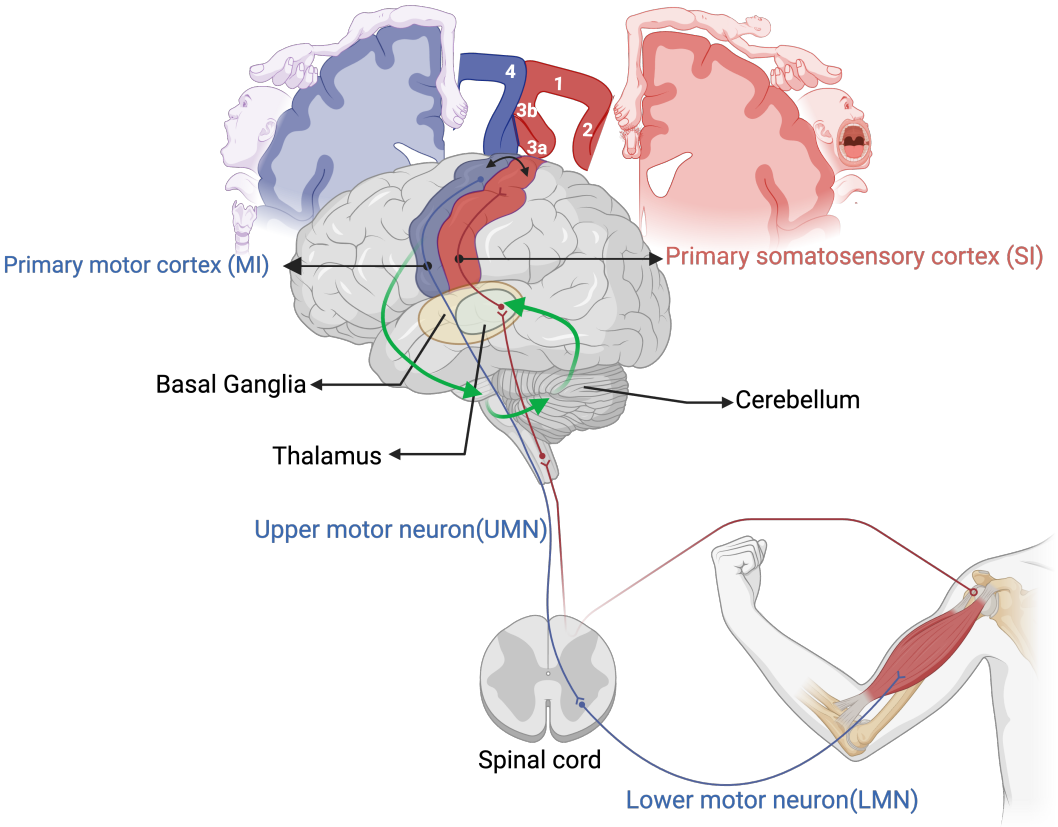

Figure 2.1 Schematic representation of the sensorimotor system illustrating the key neural structures and pathways involved in voluntary movement and sensory processing. The primary motor cortex (MI, blue) sends motor commands via descending pathways to the spinal cord, controlling muscle activity. Sensory feedback from muscles and skin travels through ascending pathways to the primary somatosensory cortex (SI, red). Basal ganglia, thalamus and cerebellum form parallel processing hubs that refine both descending motor commands and ascending sensory feedback (green). The homunculus diagram (at the top) illustrates the somatotopic organization of SI and MI, where adjacent body parts are represented in a topographically ordered manner[1].

from secondary cortical areas and thalamic nuclei, ensuring continuous information flow crucial for sensorimotor function.

2.2 Impact of Aging on Sensorimotor Function

Normal aging brings small but cumulative changes that weaken touch and movement control. Older adults routinely report higher detection thresholds, slower manual tasks, and less steady grip. MRI work links these behavioural shifts to gradual cortical thinning in frontal and parietal lobes, in-

[1]Figure:2.1 is generated using Biorender [https://app.biorender.com].

cluding the hand zones of **SI** and **MI** [31]. Thinner cortex is one sign of broader micro-structural change—dendritic loss, reduced myelination, and altered neurotransmission—that can erode the sharp borders of the somatotopic maps that support fine motor skills.

A recurring finding is *representational dedifferentiation*: digit or limb maps that are clear and separate in young adults begin to blur together with age [23, 57]. Much of this blurring is traced to declining inhibition. Spectroscopy and paired-pulse TMS show that GABA levels and short-interval intracortical inhibition drop after mid-life [76, 116]. With fewer inhibitory brakes, excitation spreads more easily, producing broader receptive fields and weaker surround inhibition—one finger stimulus leaks into neighbouring digit columns [86]. The sensory consequence is poorer tactile acuity; the motor consequence is less precise muscle recruitment and, at times, unwanted co-contractions [38].

Brain-wide activity patterns also shift. Task-based fMRI reveals that older adults often co-activate homologous regions in the opposite hemisphere or engage extra premotor and parietal areas—behaviour captured by the HAROLD model of reduced lateralisation [10]. Resting-state work adds that connectivity within the sensorimotor network can either lose specificity or become globally stronger, indicating network-level reorganisation [83].

Data used later in this thesis echo these trends (used in Chapter 4). A recently published study using population receptive-field (PRF) mapping shows that finger-map amplitude and surface area in SI are largely preserved with age, yet the fingerprints of individual digits overlap more than in youth. The smaller distance between index and middle-finger representations (D2–D3) correlates with poorer tactile individuation but, interestingly, with steadier gross grip [57]. These results hint that some dedifferentiation may be compensatory, trading fine precision for broader, more robust motor output.

In short, aging tilts the excitation–inhibition balance, flattens somatotopic detail, and reshapes network interactions in SI and MI. These baseline changes are important for two reasons. First, they frame the hypotheses tested in **Study 1**. Second, they set a reference against which the more aggressive cortical disruption seen in ALS (next section) can be evaluated. Quantifying such subtle age effects demands both high-resolution imaging and analytic tools that can detect distributed pattern changes—methods introduced in the next chapter on methodological frameworks.

2.3 Cortical Changes in Amyotrophic Lateral Sclerosis (ALS)

ALS is a neurodegenerative disease primarily affecting the motor system, distinguished by the progressive loss of upper motor neurons (UMN) in the MI and lower motor neurons (LMN) in the brainstem and spinal cord. While the defining clinical feature of ALS is muscle weakness and atrophy due to motor neuron death, there is growing recognition that ALS involves widespread cortical

changes, even beyond the motor strip. In the cortex, one prominent finding in ALS patients is cortical thinning, particularly of MI and adjacent frontal regions. High-resolution structural MRI studies report that ALS patients exhibit significantly reduced thickness of the precentral gyrus (where MI resides) compared to age-matched controls [18]. This thinning reflects underlying neuropathology such as loss of large pyramidal neurons (e.g., Betz cells) and their axons, as well as dendritic retraction and gliosis. Notably, cortical atrophy in ALS is not uniform: the degree of MI atrophy can correlate with the extent of upper motor neuron signs clinically, and some studies find additional thinning in premotor, temporal, or even parietal areas as the disease advances [2]. These structural changes underscore that ALS, though traditionally viewed as a pure motor neuron disease, has a cortical signature of neurodegeneration.

Beyond structural atrophy, cortical hyperexcitability has emerged as an important pathophysiological hallmark of ALS. Even at early or pre-symptomatic stages, patients show evidence of increased cortical excitability and reduced inhibition in Transcranial Magnetic Stimulation (TMS) studies [73, 108, 102]. For example, ALS patients often have a shortened cortical silent period and reduced motor threshold, indicating that their motor cortex neurons are more easily excited. This hyperexcitability is thought to result from a combination of mechanisms: degeneration of inhibitory interneurons, changes in glutamate neurotransmission and uptake, and altered intrinsic excitability of surviving neurons [108, 113]. In essence, as ALS progresses, the delicate balance of excitation/inhibition in the motor cortex tilts towards unchecked excitation, which may drive further neuronal damage through excitotoxicity. Clinically, markers of cortical hyperexcitability have predictive value: they often precede the onset of overt motor symptoms and have been associated with faster disease progression [72, 108]. This supports the “dying-forward” hypothesis, which posits that ALS pathology might start in the motor cortex (upper motor neurons) and then propagate downstream [72, 27].

Functional and connectivity changes accompany these structural and excitability alterations. Disrupted functional connectivity within sensorimotor networks is frequently reported in ALS. Paradoxically, many neuroimaging studies have observed increased functional connectivity (sometimes termed hyperconnectivity) in the brains of ALS patients, both in motor networks and across distributed networks [1, 16]. Using fMRI and electroencephalogram (EEG), researchers have found that ALS patients can show stronger synchrony between MI and other cortical regions at rest compared to controls, possibly due to loss of normal inhibitory modulation [66, 61]. Two not mutually exclusive interpretations exist: one is that the brain is recruiting additional regions (e.g., adjacent premotor or contralateral motor areas) to compensate for the failing MI; another is that reduced inhibitory control leads to a pathological increase in correlated activity (i.e., desynchronized inhibition allows normally independent regions to fluctuate together) [108]. In motor tasks, ALS patients often exhibit an abnormal activation pattern, such as excessive activation of secondary motor areas and diffuse

patterns that likely reflect compensatory effort to perform movements with a compromised motor system. Over the course of ALS, connectivity studies suggest a progression: early in the disease, increases in connectivity are observed (due to disinhibition or compensation), but in later stages, as neurons and connections are lost, connectivity may eventually drop [104].

Together, these structural and functional shifts paint ALS as an accelerated, more destructive version of the age-related changes outlined earlier: inhibition collapses, maps loosen, and networks rewire, but here the process is rapid and ultimately degenerative. Quantifying this progression—especially the early hyper-excitable stage targeted in **Study 2**—requires the spatial detail of 7T MRI and analysis methods that can detect subtle shifts in MI activation and connectivity.

2.4 7T MRI for Fine-Scale Cortical Mapping

UHF MRI at 7T offers significant advantages for studying the fine-scale organization of the cerebral cortex, making it ideal for investigating subtle changes in SI and MI. The substantially increased signal-to-noise ratio (SNR) at 7T compared to 3T [100] allows for acquiring images with higher spatial resolution (below 1 mm^3), approaching the scale of cortical layers and columns. This is crucial for resolving detailed somatotopic maps and visualizing thin cortical structures with less partial volume averaging [100, 18, 109].

7T also enhances blood-oxygenation-level-dependent (BOLD) contrast-to-noise ratio, providing greater sensitivity and potentially better spatial specificity for functional activation detection, less affected by large draining veins [109]. This enables the differentiation of signals from superficial versus deep cortical layers using specialized sequences, offering insights into cortical circuit dynamics previously inaccessible at lower fields [39, 40].

Further advantages include improved MR spectroscopy for quantifying neurotransmitters like GABA and glutamate with greater accuracy [116], and enhanced visualization of cortical myeloarchitecture using quantitative imaging, potentially revealing sublayers or demyelination [55, 57, 24, 71]. Faster imaging or multi-band techniques at 7T also allow high-resolution whole-brain coverage with sufficient temporal resolution. While technical challenges exist (e.g., artifacts, field inhomogeneities), methodological advancements have largely mitigated these for cortical imaging. Thus, 7T MRI acts as a magnifying lens, enabling mesoscopic-scale study of the sensorimotor system crucial for characterizing age and disease effects.

In the context of this thesis, the choice of 7T MRI is motivated by the need to detect fine and potentially subtle changes in cortical organization that occur with aging and ALS. The higher fidelity images from 7T provide greater power to observe differences in cortical thickness, map delineation, and activation magnitude that might escape detection at lower field strengths. In essence, 7T acts

as a magnifying lens on the cortex, allowing us to study the sensorimotor system's architecture and function at a mesoscopic scale. This capability is key for precisely characterizing how aging and disease modify the brain, as it enables us to see where and how cortical representations are shifting or degrading.

2.5 Challenges in High-Dimensional Neuroimaging Data

The leap to higher-resolution and multi-faceted neuroimaging data (such as those obtained at 7T) brings with it a significant challenge: the curse of dimensionality. Modern MRI datasets can contain hundreds of thousands of voxels per brain volume, with each voxel time course serving as a separate feature in functional analyses. When combined with multiple subjects, conditions, or imaging modalities, the data space becomes overwhelmingly large. Traditional univariate analysis approaches in fMRI—examining each voxel independently with statistical tests—face limitations in such contexts. Not only do univariate tests suffer from heavy corrections for multiple comparisons (increasing the risk of false negatives), they also ignore the multivariate structure of the data that could carry important information (for example, patterns across voxels that collectively distinguish conditions even if single voxels do not). Moreover, in studies of aging or ALS, the inter-subject variability in functional anatomy can be high, meaning the exact location of a functional area or the extent of cortical thinning differs across individuals. Standard group analyses that rely on one-to-one voxel correspondence (after stereotaxic normalization) may fail to capture homologous signals if fine-scale features are misaligned between subjects.

Another analytical hurdle is integrating complex data types and finding meaningful lower-dimensional representations of the data. High-dimensional neuroimaging data are noisy and often collinear, which makes straightforward application of regression or classification techniques problematic due to overfitting. In our case, we are not only dealing with high spatial dimensionality, but also potentially multiple conditions (e.g., different task stimuli, multiple finger movements) and multiple subject groups (young vs. old, or healthy vs. ALS). Making sense of such rich data requires methods that can reduce dimensionality while preserving the essence of the signals of interest. It also requires approaches to align data across subjects in a way that does not rely purely on anatomical correspondence, since anatomy alone may not guarantee functional correspondence at a sub-millimeter scale [37].

To address these challenges, researchers have increasingly turned to multivariate analysis techniques and sophisticated statistical learning methods. Rather than examine each feature in isolation, multivariate methods consider the simultaneous relationship between all features, capturing distributed patterns that correspond to cognitive or disease states. These methods can discover latent variables or

components that summarize the data, often improving SNR by leveraging covariance patterns. In the context of this thesis, two such approaches have been implemented: the SRM and PLSR. Each tackles a different aspect of the high-dimensional data problem discussed in the next chapter (Chapter 3).

In summary, this chapter has identified the major theoretical and methodological challenges: aging and ALS likely induce subtle, distributed changes in sensorimotor brain function, and detecting these requires both ultra-high-resolution data (to see the changes) and multivariate analysis (to interpret them). The following chapter turns to the tools that will meet these challenges – introducing how we align data across subjects and how we relate neural patterns to external variables, thereby connecting the “what” and “why” from this literature review to the “how” of our experimental approach.

Chapter 3

Methodological Frameworks

3.1 Multivariate Analysis in Neuroimaging

The previous chapter ended with a central problem: modern 7T fMRI delivers millions of voxel-wise measurements per participant, yet the neural effects we care about—age-related shifts in SI or ALS-driven changes in MI—are subtle and spatially distributed. Mass-univariate statistics struggle in this setting: they ignore the covariance structure of the data, require heavy multiple-comparison correction, and can miss patterns that emerge only when voxels are considered together. What we need, therefore, are methods that (i) compress the data into a few informative dimensions, (ii) align those dimensions across subjects, and (iii) link them to behaviour or clinical state.

Multivariate analysis meets these requirements by treating each brain volume as a pattern rather than a collection of independent voxels. Instead of asking whether, voxel 'X' is different between groups, we ask whether, a pattern 'P'-a weighted combination of many voxels—distinguishes groups or predicts an external measure [36, 68]. Because the analysis lives in pattern space, it is naturally more sensitive to weak, distributed signals and far less vulnerable to the curse of dimensionality.

By modeling covariation across voxels or selecting informative combinations of voxels, multivariate methods can capture distributed signals that are too subtle to detect univariately [35, 64]. In this view, brain activation is characterized by patterns (vectors) in a high-dimensional voxel space [35].

Classical Multivariate Techniques

Several foundational techniques exemplify these ideas. Principal Component Analysis (PCA) rotates the data into orthogonal axes that capture the greatest variance, letting fMRI time-series be summarised by a few spatial or temporal components [93, 62]. Independent Component Analysis (ICA) adds a statistical twist: it extracts spatial maps that are maximally independent, separating functional

networks from noise and revealing resting-state systems without prior models [64]. Both PCA and ICA are often used as feature-extraction steps—retain the strongest components or voxels, then carry those lower-dimensional features into further tests [35, 45].

Multivoxel Pattern Analysis (MVPA) moves to supervised learning. Each multi-voxel pattern is an observation; classifiers or regressors ask whether two conditions have reliably different "fingerprints." Early work showed that ventral-temporal patterns discriminate object categories [35], and searchlight MVPA now outperforms univariate maps when signals are weak but widespread [12].

Importantly, PCA/ICA/MVPA laid the groundwork for more sophisticated multivariate models. They demonstrated the power of learning low-dimensional representations of brain activity. For instance, PCA/ICA showed that brain-wide covariance can be summarized by a few components, and MVPA showed that these components can predict experimental conditions.

This set the stage for group and multimodal extensions of multivariate analysis with two key takeaways : (i) information in fMRI is often spread across many voxels, and (ii) reducing that high-dimensional space to a handful of latent patterns increases power and interpretability.

Keeping these principles in mind, we now turn to two specific multivariate methods that will be used in this thesis: SRM and PLSR. These methods are designed to address the challenges of high-dimensional fMRI data, particularly in the context of 7T imaging, where spatial resolution is high but inter-subject variability is also pronounced.

3.2 Shared Response Modeling for Ultra-High-Field Neuroimaging

UHF 7T neuroimaging offers unparalleled spatial resolution, enabling the study of fine-scale functional structures like cortical layers and columns—key to understanding processes like aging and neurodegeneration, as outlined in Chapter 2. Yet this very high resolution amplifies challenges, particularly the substantial anatomical and functional variability between individuals. Even after standard anatomical registration, two different brains may not align at the level of fine-grained functional organization. Traditional approaches like heavy spatial smoothing or averaging across subjects risk blurring or erasing the very fine-scale details that make 7T data valuable [68]. In other words, conventional inter-subject alignment can fail to capture subtle somatotopic shifts or columnar patterns, prompting the need for methods that perform *functional alignment* rather than relying solely on anatomy.

SRM addresses this need by aligning subject-specific fMRI data at the functional level, seeking a common representational space that each brain's data can be projected into [36, 15]. Conceptually, SRM builds on the idea that a common time-varying stimulus (e.g. a repeated tactile stimulation

sequence) will evoke *shared neural response patterns* across individuals, even if the exact voxel responses differ due to idiosyncratic anatomy or functional layout. The goal is to find a set of latent features that capture the stimulus-driven variance shared by all subjects, while separating out subject-specific activity. This approach is akin to prior "hyperalignment" method proposed by Haxby and colleagues [34, 37, 15], which also compute a transformation of individuals' fMRI data into a common high-dimensional space where corresponding dimensions reflect analogous neural signals across brains. By performing such functional alignment, SRM preserves fine-grained information (since minimal or no spatial smoothing is needed) and improves across-subject correspondence of neural representations.

Mathematically, SRM assumes each subject's data can be factorized into a set of k shared latent time courses and subject-specific spatial weights. Let $X_i \in \mathbb{R}^{v\times d}$ denote the fMRI data matrix for subject i, where v is the number of voxels and d the number of time points. SRM seeks a shared feature space of dimension k (with $k \ll v$) and subject-specific basis matrices that project each subject's data into that space. The procedure involves three main steps:

1. **Learn subject-specific bases:** For each subject i, estimate a basis matrix $W_i \in \mathbb{R}^{v\times k}$ that maps that subject's voxel space to a k-dimensional latent feature space. In practice, W_i can be thought of as k spatial maps (one per latent feature) for subject i. Applying the basis to the data gives $W_i^\top X_i$, a $k \times d$ representation of subject i's data in the latent space.

2. **Derive the shared response:** Combine the projected data from all subjects to identify a single $k \times d$ matrix S (the "shared response") that captures temporal patterns common to everyone. S can be viewed as k time courses (one per latent feature) that are common across subjects. Intuitively, while each subject's original time series X_i is different, after projection by W_i the resulting time series $W_i^\top X_i$ should all approximately match S.

3. **Apply to new data:** For a new subject or a new dataset X_i', project it into the learned shared space using that subject's basis: $S_i' = W_i^\top X_i'$. This yields a representation S_i' in the common space, which can then be used for further analysis (e.g. cross-subject comparisons or machine learning). In effect, any individual's data (even data not used to train the model) can be aligned into the shared feature space via its W_i.

In summary, SRM finds a set of subject-specific linear transformations W_i and a shared time-series matrix S such that $X_i \approx W_i S$ for all subjects i. Equivalently, one can write the data of subject i as:

$$X_i = W_i S + E_i,$$

where:

$$W_i \in \mathbb{R}^{v\times k}, \quad S \in \mathbb{R}^{k\times d}, \quad E_i \in \mathbb{R}^{v\times d}.$$

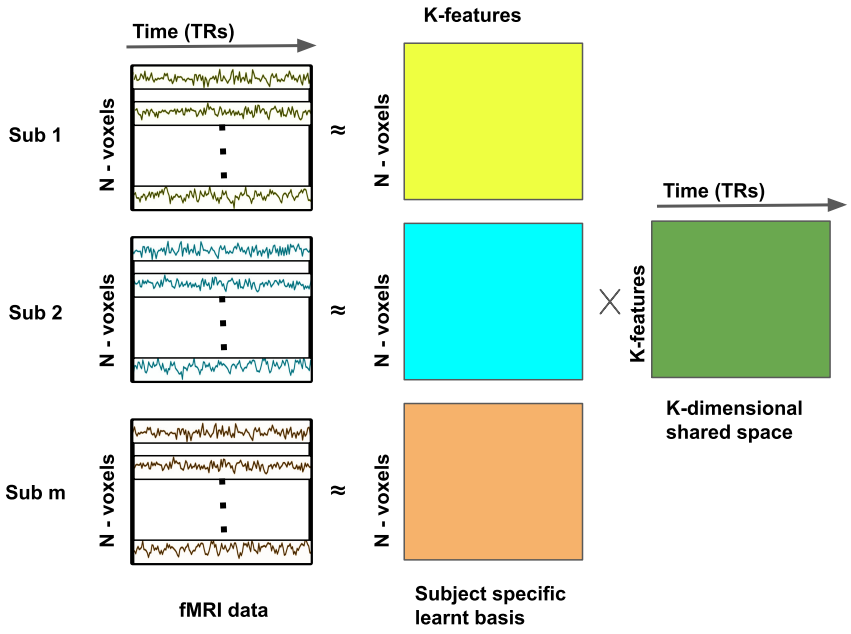

Figure 3.1 **Illustration of the shared response framework.** The observed fMRI time-series can be viewed as a linear combination of shared latent time courses (S) weighted by subject-specific bases (W_i).

where E_i is residual subject-specific activity not captured by the shared response. The W_i and S are optimized (often iteratively) to maximize the across-subject correlation or alignment in the latent space. By modeling each X_i as the sum of a reconstructed shared response (W_iS) and individual-specific residual E_i, SRM explicitly separates stimulus-driven common signals from idiosyncratic noise or other effects. The optimization problem can be expressed as:

$$\min_{W_i,S} \sum_{i=1}^{m} \|X_i - W_i S\|_F^2 \quad \text{subject to} \quad W_i^\top W_i = I_k.$$

An alternating optimization updates S and W_i until convergence. Once trained, new data X_i' are projected into the shared space via $S' = W_i^\top X_i'$. Crucially, this is achieved without needing to average or blur data across brains; alignment happens in feature space, thus preserving the fine spatial granularity of each subject's 7T data.

Figure 3.1 illustrates the SRM framework. Each subject's observed fMRI time series is modeled as a linear combination of a set of shared latent time courses (S) weighted by that subject's basis W_i. Through SRM, the latent features in S come to represent functionally corresponding activity patterns across subjects (e.g. a particular latent feature might correspond to a specific finger's stimulation

response in SI for all individuals, even if the exact voxel pattern differs per person). As a result, data can be aggregated or directly compared in the shared feature space, greatly facilitating group analyses of high-dimensional data.

Several variants of SRM have been proposed to address specific challenges and to tailor the alignment to different use cases. For example, *Robust SRM (rSRM)* includes regularization to reduce the influence of noisy or outlier voxels, thereby improving reliability when some subjects' data are particularly noisy [99]. *Connectivity SRM (cSRM)* aligns not raw fMRI responses but functional connectivity patterns, which can be useful if one is more interested in network correspondence than stimulus-locked time courses [67]. *Columnar SRM (C-SRM)* is designed for sub-millimeter fMRI, aiming to align data at the level of cortical columns (critical for 7T studies focusing on cortical microstructure) [45]. *Searchlight SRM (sSRM)* applies SRM in a local, searchlight fashion to capture regionally localized shared structure [114]. These adaptations are valuable for 7T data where retaining precise spatial detail is paramount—each variant makes trade-offs between sensitivity to shared signals and specificity to fine-scale anatomy.

It is important to acknowledge the limitations of SRM as well. First, SRM (in its basic form) is a linear method: each subject's data is assumed to be a linear transform of the shared features. Nonlinear differences between individuals' functional organization (for example, idiosyncratic distortions of representational geometry) may not be fully corrected by a linear alignment. Extending SRM with nonlinear mappings (e.g. via kernel methods or neural network mappings) is a potential future direction to capture more complex correspondences.

Second, SRM requires that subjects share the same time-locked stimulus or task events. If individual subjects respond to different stimuli or if timing is misaligned, the model cannot find a common S. This means SRM is best suited for experiments with a common protocol (as in our case); it is less applicable to resting-state data unless one uses a variant like cSRM for connectivity patterns.

Third, SRM's focus on shared variance means that individual-specific signals are pushed into the residual E_i and essentially ignored. If those idiosyncratic patterns are of interest (for example, unique compensatory activations in older adults), SRM alone will not analyze them. One must either examine the residuals separately or use complementary methods. Despite these limitations, SRM provides a powerful framework for functional alignment. Some of these concerns were mitigated by using the robust variant (to handle noise) and by validating that SRM alignment actually improves the ability to decode and interpret the data (for example, using Support Vector Machine (SVM) based classification as a validation step). In summary, SRM offers a principled way to align high-dimensional fMRI data across individuals, preserving the fine detail of 7T imaging and laying a foundation for group-level analyses that are sensitive to subtle neural representation changes.

In this thesis, rSRM is applied to facilitate cross-subject comparisons in the somatosensory aging experiment (in Chapter 4). By preserving fine-scale details and aligning variable datasets, SRM not

only overcomes key limitations of traditional approaches but also sets the stage for complementary methods like PLSR. The next section explores PLSR, which builds on SRM's aligned representations to link neural patterns with behavioral and clinical outcomes, further advancing our understanding of brain function in health and disease.

3.3 Partial Least Squares Regression for Linking Neural Activity to Behavior

While SRM aligns high-dimensional fMRI data across subjects to uncover shared neural responses, PLSR offers a distinct approach by relating neural activity directly to external variables such as behavioral or clinical measures. Originally developed in the fields of econometrics and chemometrics, PLS methods were introduced to neuroimaging by McIntosh and colleagues as a way to uncover relationships between brain data and experimental design or performance measures [63, 51]. In essence, PLSR asks: what patterns in the brain data X best predict or correspond to changes in an outcome measure Y? Here X might be a matrix of fMRI measures (e.g. voxel activation levels, or connectivity metrics) and Y could be a vector or matrix of behavioral scores, clinical ratings, or experimental variables.

Intuitively, each PLS component can be thought of as a weighted combination of voxels (for X) that is most strongly correlated with a weighted combination of behavioral/clinical variables (Y). By finding these coupled weight vectors, PLSR effectively filters the data to isolate brain patterns that are most relevant to the behavior of interest. A critical advantage of this approach is that it can handle situations where X has many more variables than observations (e.g. tens of thousands of voxels but only dozens of subjects). Rather than trying to fit thousands of independent univariate models or risking overfit by including all voxels in a single massive regression, PLSR reduces the problem to a smaller set of components. These components capture the major covariation trends, thus improving statistical power and interpretability.

In the context of neuroimaging, PLSR has been successfully used to identify distributed neural patterns linked to cognitive performance, to differentiate patient groups based on brain-behavior correlations, and to relate connectivity patterns to clinical symptoms. Importantly, unlike purely predictive machine learning approaches, PLSR yields a bi-directional mapping: one can project the brain data to obtain component scores, but also project the latent components back into the original voxel space to visualize the spatial pattern associated with a particular brain–behavior mode. This means the results of PLSR can be interpreted in terms of brain regions—e.g., a map of voxel weights indicating which areas contribute most to a component that tracks symptom severity. In summary, PLSR provides a balance between dimensionality reduction and interpretability: it finds compact

representations of the data that are maximally behaviorally relevant, and those representations can be translated back into brain images.

To illustrate how PLSR works, consider an application in this thesis: an analysis of patients with ALS. Here, we have brain imaging data X (for example, measures of functional connectivity between motor regions, or activation levels during a task) and clinical ratings Y (e.g. the ALS Functional Rating Scale Revised (ALSFRS-R), which quantifies disease severity). PLSR will seek a set of latent variables such that, say, the first latent variable captures the pattern of brain connectivity that covaries most with ALSFRS-R scores across individuals. In practical terms, PLSR might find that a connectivity pattern involving MI and brainstem nuclei strongly tracks patients' motor scores: patients with weaker connectivity in that network have worse clinical scores. This would emerge as a first PLS component with high weights on those connections and a corresponding weight on the ALSFRS-R variable. Subsequent components would capture remaining covariance (for example, a second component might relate a different network or perhaps an activation pattern to another clinical measure), each orthogonal to the previous ones. By testing these components' significance (through cross-validation) we can ensure the findings are robust.

Figure 3.2 depicts the PLSR framework in a neuroimaging context. The high-dimensional brain data matrix X is decomposed into latent variables (weighted combinations of voxels) that best predict the external variables in Y. This process yields pairs of latent components: one in the brain data space and one in the behavioral space, which are maximally correlated. For example, one such pair might be "component 1: widespread frontal and parietal activation increase" in X paired with "component 1: high cognitive score" in Y, indicating that subjects with that activation pattern tend to have better cognitive performance.

Formally, if X is an $n \times p$ matrix (e.g. n subjects, p voxel features) and Y is $n \times q$ (e.g. q behavioral measures), PLSR finds weight vectors w_x (length p) and w_y (length q) such that the projections $u = Xw_x$ and $v = Yw_y$ have maximal covariance. These u and v are the scores for the first latent component in each domain. After extracting this component, residual covariance is analyzed to find the next component, and so on, typically up to a number of components that explain most covariance but not beyond what the data can support (to avoid overfitting). Notably, if Y is univariate (one outcome measure), PLSR reduces to finding components of X that best predict that measure, somewhat analogous to a multivariate regression but with the benefit of dimensionality reduction. If Y contains multiple measures, PLSR finds common components influencing all of them. This flexibility makes PLSR a powerful technique for exploring complex brain-behavior datasets [63].

In this thesis, PLSR is used in the ALS study (Chapter 5) to uncover patterns of brain activity and connectivity that relate to disease severity. Specifically, we apply PLSR in two ways: (1) to find spatial patterns of functional activation (during motor tasks) that correlate with patients' ALSFRS-R scores, and (2) to find network connectivity patterns that correlate with ALSFRS-R. This allows us to

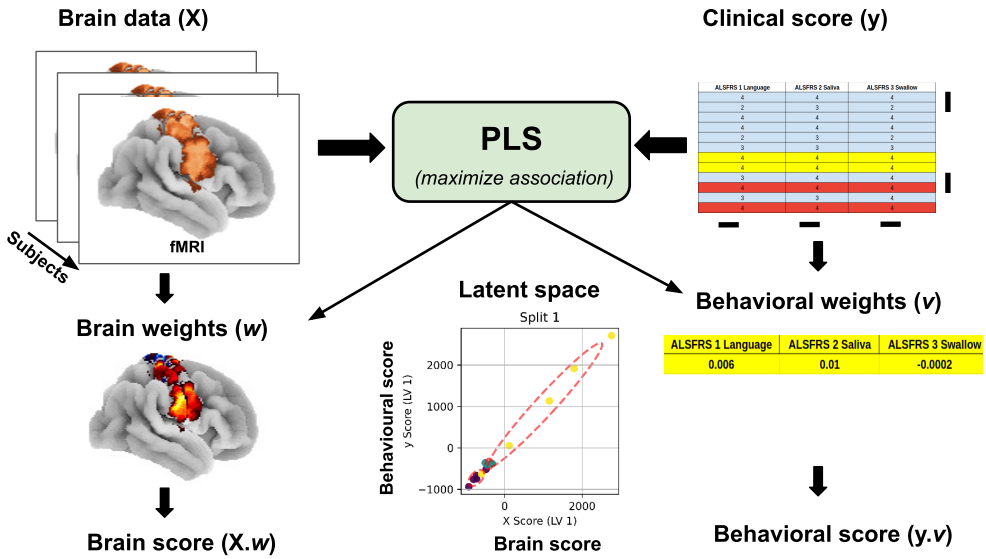

Figure 3.2 **Illustration of the PLSR framework.** Brain data (X) are decomposed into latent variables that best predict behavior/clinical variables (Y).

test H5, which posits that connectivity patterns might be more sensitive indicators of ALS progression than activation magnitudes. By using PLSR, we can directly compare which domain (activation vs connectivity) yields a stronger brain–clinical correlation. Moreover, PLSR's latent variables provide a convenient summary: for each subject, a single PLS component score can summarize "disease-related brain pattern expression," which can then be compared or tracked.

In conclusion, the methodological frameworks presented in this chapter – SRM (with its variants) and PLSR – equip us to effectively analyze the multivariate 7T-fMRI data and to test the thesis hypotheses. SRM will allow us to share information across subjects and isolate fine-scale common patterns (crucial for evaluating H1–H4), while PLSR will allow us to link brain patterns to clinical metrics (crucial for H5). Armed with these tools, we proceed in the next chapters to the empirical studies of aging (Chapter 4) and ALS (Chapter 5), where we will apply SRM and PLSR to real data and report the results in light of the hypotheses and literature discussed so far.

Chapter 4

Functional Changes in Aging

4.1 Introduction

Decoding tactile inputs in the somatosensory cortex is fundamental to sensory processing, with the SI and secondary somatosensory cortex (SII) forming an interconnected network. SI, encompassing BA 3 (subdivided into 3a and 3b), 1, and 2, acts as the primary hub, receiving direct thalamic input that relays bodily sensory signals [43, 74]. Within SI, BA3b excels in fine touch discrimination by processing the bulk of this input, BA1 integrates broader sensory patterns, and BA2 handles higher-order perception [32, 54].

High-resolution 7T fMRI has illuminated SI's voxel-level patterns and columnar organization, achieving precise classification of finger-specific responses in younger adults [89]. SII, situated in the parietal operculum, enhances this system by integrating bilateral inputs and supporting tactile memory and learning, with projections to SI, the insula, and motor areas aiding sensory-motor coordination [32]. These findings, detailed in Chapter 2, underscore SI's role in maintaining distinct tactile representations—critical for the precision targeted in this thesis.

Aging disrupts this organization, challenging neuroscience to unravel its implications. In older adults, SI's representational specificity decreases, with fMRI revealing less distinct digit activation patterns, especially in BA3b, compared to younger cohorts [8, 84]. This decline manifests as increased overlap between sensory maps—potentially from weakened inhibitory control, as adjacent finger representations co-activate more often and reduced processing efficiency [7]. Reorganization, more evident in BA3b due to its fine tactile role, may stem from signal compensatory shifts or precision loss, impacting tactile acuity, sensory speed, and motor coordination [77]. Chapter 1's hypotheses (H1-H3) frame these changes as testable shifts in representational precision (H1) and columnar scale (H2), necessitating high-resolution tools like 7T fMRI along with advanced multivariate analysis approach to detect them (H3).

Such subtle differences in SI digit topography are hard to discern individually but emerge through group-level analysis, where aggregating data enhances statistical power. Yet, aligning high-resolution 7T fMRI across subjects is complex, traditional anatomical normalization and smoothing often obscure fine-scale features like columnar units, undermining 7T's strengths. Robust-SRM, introduced briefly in Chapter 3, overcomes this by aligning responses in a low-dimensional shared space, preserving variance while reducing noise. Here we extend rSRM with a columnar variant (C-SRM) that systematically varies column width, allowing us to ask whether ageing widens the functional "grain" of SI.

This chapter aims to:

1. Test H1 by assessing age-related shifts in finger-specific response precision across SI (BA3b, BA1, BA2) and motor areas (BA4a, BA4p, BA6) using decoding accuracy.

2. Validate C-SRM for tactile finger differentiation, exploring how optimal columnar scales vary between younger and older adults (tests H2).

3. Evaluate rSRM's alignment superiority over conventional preprocessing in 7T fMRI, by measuring classification performance (tests H3).

These objectives harness rSRM and C-SRM to reveal age-driven functional differences in SI, tackling aggregation and dimensionality challenges (described in Chapter 2) in 7T fMRI. Focused on tactile maps, this framework extends to other regions, complementing Chapter 5's ALS study. The following sections outline the experimental design, data acquisition, and analyses, testing H1-H3 to clarify aging's impact on SI's architecture and its wider significance.

4.2 Population and Study Design

4.2.1 Participants

A total of 38 healthy participants were recruited for the study, divided into two age groups: younger adults (n = 19, mean age 25 ± 0.49 years, range 21–29, 9 females) and older adults (n = 19, mean age 72.2 ± 0.81 years, range 65–78, 9 females). Participants were recruited from the database of the Deutsches Zentrum für Neurodegenerative Erkrankungen (DZNE) in Magdeburg, Germany. All participants were screened for standard 7T-MRI exclusion criteria, including metallic implants, active medical devices (e.g., pacemakers, neurostimulators), permanent makeup, tinnitus, or other hearing impairments. Written informed consent was obtained before participation, and participants were compensated for their time. The study was approved by the Ethics Committee of the Otto-von-Guericke University Magdeburg.

4.2.2 MRI Scanning Protocol

UHF-MRI data were acquired using a whole-body 7 Tesla Siemens MRI scanner (Siemens Healthcare, Erlangen, Germany) equipped with a 32-channel Nova Medical head coil. The scanning protocol began with the acquisition of a whole-brain MP2RAGE sequence with the following parameters: voxel resolution of 0.7 mm isotropic, 240 slices, a field of view (FoV) of 224 mm, TR = 4800 ms, TE = 2.01 ms, inversion times TI1/2 = 900/2750 ms, and GRAPPA acceleration factor of 2 in the sagittal orientation. Shimming was performed prior to functional scans to optimize the magnetic field homogeneity. Additionally, two echo-planar imaging (EPI) volumes with opposite phase-encoding (PE) polarity were acquired to correct for geometric distortions.

Functional imaging was conducted using a gradient-echo EPI (GE-EPI) sequence with a voxel resolution of 1 mm isotropic, FoV of 192 mm, TR = 2000 ms, TE = 22 ms, GRAPPA factor of 4, interleaved acquisition, and 36 slices. This functional sequence was employed consistently across all experimental tasks. On a separate day, structural MRI data were acquired using a Philips 3T Achieva dStream MRI scanner at the in-house facility of the Leibniz Institute for Neurobiology (LIN), Magdeburg. A standard structural 3D MPRAGE sequence was used, with the following parameters: voxel resolution of 1.0 mm isotropic, TI = 650 ms, echo spacing = 6.6 ms, TE = 3.93 ms, flip angle = 10°, bandwidth = 130 Hz/pixel, FoV = 256 mm × 240 mm, slab thickness = 192 mm, and 128 slices.This scanning protocol provided high-resolution structural and functional data, enabling the detailed analysis of fine-grained cortical features, particularly in the SI, while maintaining compatibility across imaging modalities.

4.2.3 Stimulus and Experimental Design

Tactile stimulation was applied to individual fingers (D1–D5) of the right hand using an MR-compatible piezoelectric stimulator (Quaerosys, Schotten, Germany). Five independently controlled piezoelectric modules were used, each corresponding to one digit: D1 (thumb), D2 (index finger), D3 (middle finger), D4 (ring finger), and D5 (little finger). During stimulation, participants lay in the 7T-MRI scanner, with each fingertip secured to its respective module using a custom-built, metal-free applicator. This applicator was designed for flexibility, allowing the modules to be adjusted for individual hand and finger sizes to ensure precise positioning of the stimulator pins under each fingertip. The stimulator array consisted of 8 pins arranged in a 2 × 4 layout along the proximo-distal axis of the finger, covering a skin area of 2.5 × 9 mm^2 (see Figure 4.1A). Vibrotactile stimulation was delivered at a frequency of 16 Hz, with only two pins activated at any given time to prevent sensory adaptation [88]. The stimulation frequency followed a continuous sinusoidal pattern, and the intensity was individually calibrated to 2.5 times the tactile detection threshold for each subject and

finger. Detection thresholds were determined on a separate day, with younger adults showing a mean threshold of 0.80 ± 0.04 g and older adults showing a threshold of 1.37 ± 0.07 g [57].

Cyclic Runs

The experimental protocol included two cyclic runs, each consisting of 20 cycles with a duration of 25.6 seconds per cycle. In each cycle, each fingertip received 5.12 seconds of stimulation in sequence, repeated 20 times. Stimulation was applied either in a forward order (D1 to D5) or a reverse order (D5 to D1), randomized across participants and age groups to balance any potential order effects. Each run consisted of 256 scans (TR = 2 seconds), lasting a total of 8 minutes and 31 seconds, with a 1-minute rest period between runs. Cyclic designs have been shown to be particularly effective for detecting precise topographic maps of finger representations in BA3b [48, 53].

Random-Design Runs

Two random-design runs were included as localizers for defining regions of interest (ROIs) for decoding analyses in the cyclic runs. In these runs, each of the five fingers was stimulated for 5.12 seconds, similar to the cyclic design, but the stimulation order followed a pseudo-random sequence. This ensured that no finger was stimulated more than twice consecutively. Rest intervals of 2 seconds (70% of trials) or 6 seconds (30% of trials) were interspersed between stimulations. Each finger was stimulated 10 times per run, with each run lasting 6 minutes and 56 seconds (210 scans). Random designs are ideal as localizers since they eliminate bias from stimulation order [48]. The experimental design is illustrated in Figure 4.1.

Additional Considerations

To ensure participants remained attentive during the experiment, small 180 ms gaps were randomly introduced into the 5.12-second stimulation intervals. Participants were instructed to count the number of gaps in each block and verbally report their count after each run. These gaps were pseudo-randomly distributed to ensure each finger received an equal number of gaps throughout the experiment. This task served as an additional measure to maintain participant focus on the tactile stimuli.

While the study primarily employed cyclic and random-design runs, including a cyclic design with a different fixed stimulation order (e.g., D1, D3, D5, D2, D4) could have controlled for potential order effects more comprehensively. However, due to the already lengthy scanning protocol, additional functional blocks were not included.

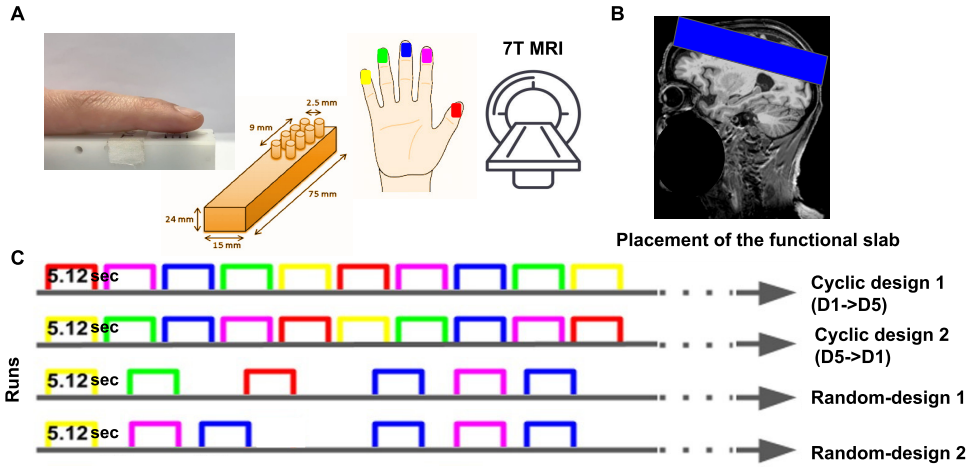

Figure 4.1 **Experimental Design Overview**. This figure illustrates the experimental setup used in the 7T-MRI study. (A) A piezoelectric stimulator was employed to deliver controlled fingertip stimulation. (B) The blue-highlighted region marks the location of the acquired slab image on an example participant's T1-weighted structural scan. (C) The rows represent different experimental conditions: the first two rows correspond to cyclic-design paradigms (Forward: D1 to D5, Reverse: D5 to D1), while the last two rows depict random-design paradigms. Each color represents stimulation of a specific finger of the right hand, as indicated in (A). *(Adapted from Kalyani et al. [45])*

4.3 Methods

4.3.1 Preprocessing

The preprocessing pipeline for 7T fMRI data was designed to mitigate motion artifacts and geometric distortions—prevalent challenges in UHF imaging while preserving the spatial resolution critical for testing age-related changes in SI. The following steps ensured data quality for rSRM and C-SRM analyses:

1. Distortion Correction: To counteract geometric distortions caused by participant movement and magnetic field inhomogeneities, two EPI volumes with opposite phase-encoding (PE) polarity were acquired before the functional scans. Distortion correction was performed using a point spread function (PSF) mapping method, as described by [41]. This method corrects the geometric distortions in both the forward and reverse PE datasets, creating distortion-corrected images for each polarity.

A weighted combination of the distortion-corrected images was then applied to maximize the spatial information content in the final corrected images. This approach capitalizes on the differing spatial information captured by the two opposite PE datasets, ensuring a high-fidelity representation of the functional data.

2. Motion Correction: To address motion artifacts, the EPI images from the functional blocks were corrected for motion relative to the initial time point ($t_0 = 0$). This step minimized the impact of participant movement during the scan and ensured temporal consistency across the functional volumes. Following motion correction, the extended PSF method was applied to the acquired and motion-corrected images. This step provided geometrically accurate image reconstruction, further enhancing the spatial integrity of the data, which is critical for for voxel-level decoding and columnar modeling.

3. Slice Time Correction: To correct for temporal differences in slice acquisition during the interleaved EPI sequence, slice-timing correction was performed using `SPM8` (Statistical Parametric Mapping, Wellcome Department of Imaging Neuroscience, University College London, UK)[4]. This ensured that all slices within a volume were temporally aligned, facilitating accurate downstream analyses.

The preprocessing pipeline effectively addressed the challenges posed by motion artifacts and geometric distortions inherent to 7T MRI data acquisition. By combining advanced distortion correction techniques with motion correction, slice-timing correction, and geometrically accurate reconstruction, the final preprocessed data provided a robust foundation for subsequent multivariate analyses. These preprocessing steps preserved the high spatial resolution of the UHF data, enabling precise investigation of SI's functional architecture across age groups, as detailed in the following sections.

4.3.2 Decoding Analyses

To investigate tactile representations in SI, first-level fixed-effects models were computed per participant using the General Linear Model (GLM) in `SPM8`. Two random-design runs modeled five regressors for digits D1–D5, with linear contrasts (e.g., [4 -1 -1 -1 -1] for D1) estimating individual finger responses. No group alignment, smoothing, or normalization was applied, preserving 7T fMRI's fine-scale resolution. This random-design dataset served as an independent localizer, defining finger-specific ROIs, with its randomized stimulation sequence, optimizing individual digit localization [107].

For rSRM analysis, a cyclic design ensured a consistent stimulation order (D1–D5) across participants (as it requires a time locked stimulus to generate a shared representational space), matching SI's assumed topographic sequence. Forward and backward runs controlled for order effects, while the random-design localizer identified significant voxels (500–3000 voxel thresholds, based on the β maps) for decoding cyclic data. This approach, balanced statistical power and spatial specificity.

ROI-based analyses targeted seven sensorimotor areas (BA1, BA2, BA3a, BA3b, BA4a, BA4p, BA6) in the contralateral hemisphere (left, for right-hand stimulation), with the ipsilateral side as a control. `Freesurfer v.6.0.0` parcellated 3T MPRAGE structural data via "`recon-all`" [30], co-registered manually with 7T EPI functional data (both 1 mm isotropic) using `ITK-SNAP v.3.8` [112] and `ANTs v.2.1` [5]. This precise alignment avoided morphological discrepancies, supporting voxel-level decoding.

To maintain consistency and optimize decoding performance, the top 500 voxels were selected for analysis from each ROI, as this number yielded the highest decoding accuracy across regions and age groups. For columnar-based analyses, attention was directed toward the detailed functional representations of somatosensory finger maps within BA1 and BA3b in the hemisphere contralateral to stimulation. These analyses aimed to uncover fine-grained tactile representations while preserving the spatial specificity provided by UHF imaging.

4.3.3 Robust Shared Response Modeling (rSRM)

Similar to SRM, rSRM aims to identify a shared, lower-dimensional representation of stimulus responses across participants who are presented with the same stimulus during scanning (e.g., synchronized finger stimulation). In addition to capturing the shared neural activity, rSRM also models the individual components of brain responses that are not represented in the shared space. These individual components encapsulate subject-specific variability, making rSRM a powerful tool for detecting differences between individuals and groups.

The mathematical framework of rSRM represents the data from each subject as a combination of a shared response, subject-specific mappings, and individual components. Let the data from the i-th subject be denoted as $\mathbf{X}_i \in \mathbb{R}^{N\times t}$, where N is the number of voxels and t is the number of scanned time points. The shared response is represented by $\mathbf{R} \in \mathbb{R}^{K\times t}$, where K is the number of shared features. Each subject has a subject-specific basis matrix $\mathbf{W}_i \in \mathbb{R}^{N\times K}$, which projects the shared response into the subject's voxel space. Additionally, an individual residual term $\mathbf{S}_i \in \mathbb{R}^{N\times t}$ captures variance that is not shared across subjects. The data representation can be expressed as:

$$\mathbf{X}_i = \mathbf{W}_i\mathbf{R} + \mathbf{S}_i, \quad i = 1,\ldots,m,$$

where m is the total number of subjects.

The shared response $\mathbf{R}$ is estimated such that it captures the variance common across subjects, while the subject-specific basis matrices $\mathbf{W}_i$ and the individual residual terms $\mathbf{S}_i$ allow for flexibility

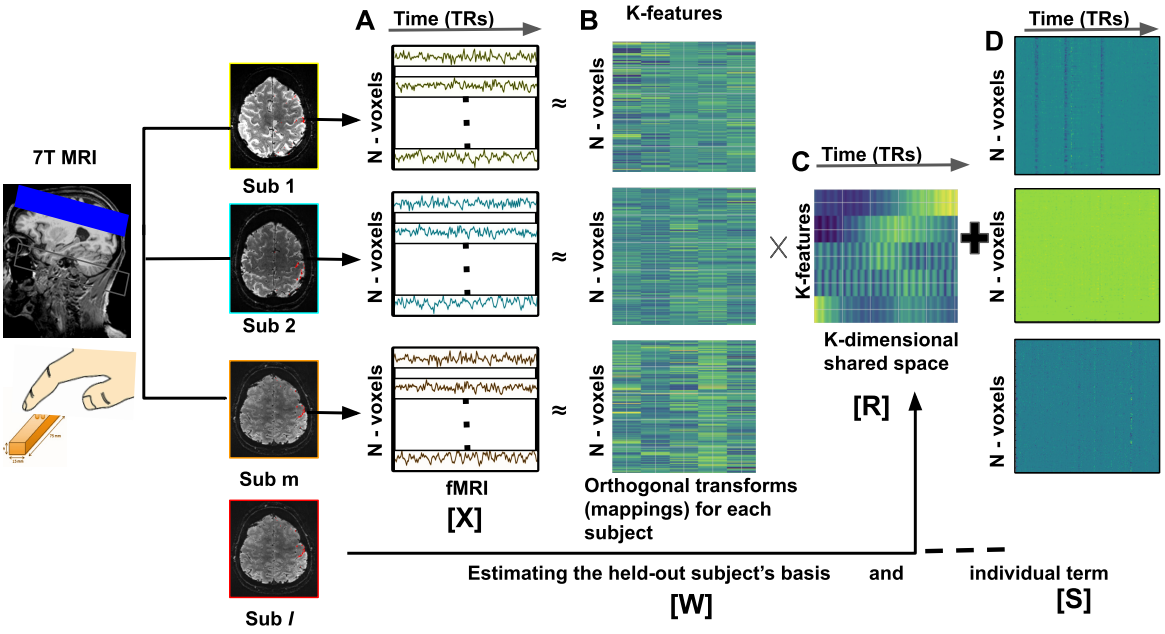

Figure 4.2 **Framework of Robust Shared Response Modeling (rSRM)** This figure illustrates the step-by-step process of rSRM applied to fMRI data analysis. (A) Cyclic stimulation (D1–D5 or D5–D1) ensures a common input structure, with $\mathbf{X}_i$ representing each subject's voxel-wise BOLD signal. (B) Subject-specific basis $\mathbf{W}_i$ (N voxels × K features) maps responses to a shared space. (C) Shared response $\mathbf{R}$ (K × t) captures common neural activity. (D) Individual residual $\mathbf{S}_i$ isolates subject-specific variance not in $\mathbf{R}$.*(Reproduced from Kalyani et al. [45])*

in representing individual variability. The residual term $\mathbf{S}_i$ is particularly useful when inter-subject variability is high, as it isolates this individual-specific information from the shared representation.

A key component of rSRM is the regularization parameter λ_i, which controls the sparsity of the individual term $\mathbf{S}_i$. This parameter determines the balance between shared and individual components in the model. In this study, the default value of $\lambda_i = 1.0$ was used, following the approach described in [99].

Subsequent sections detail rSRM's use in classifying age groups and digit-specific responses. The shared response $\mathbf{R}$ drove these classifications, leveraging its robustness to inter-subject variability, while individual residuals $\mathbf{S}_i$ were excluded to focus on shared tactile representations rather than subject-specific noise. This approach ensured that the classifier learned from the shared neural activity, enhancing its ability to generalize across subjects and age groups. The rSRM framework for leave-one-subject-out (LOSO) approach is illustrated in Figure 4.2.

[0]Figure:4.2 Reproduced from [45], with permission from Elsevier.

Digit Classification Using rSRM

To decode finger-specific tactile responses and assess rSRM's alignment capabilities, we employed a two-step process integrating shared response modeling and classification, utilizing a LOSO cross-validation framework for both stages (see Figure 4.3).

In the first step, rSRM estimated a shared response space across all but one subject (l) using data from the first cyclic run. For the $m-1$ training subjects ($i \in \{1,\ldots,m\} \setminus l$), where $m = (19young, 19old)$:

- A shared representation $\mathbf{R} \in \mathbb{R}^{K \times t}$ captured common neural responses to cyclic D1–D5 stimulation, with K as the number of shared features and t as the scanned time points.
- Subject-specific basis matrices $\mathbf{W}_i \in \mathbb{R}^{N \times K}$ projected $\mathbf{R}$ into each subject's voxel space, where N denotes the number of voxels.
- Individual residual terms $\mathbf{S}_i \in \mathbb{R}^{N \times t}$ modeled variance unique to each subject, not represented in the shared space.

During *training*, rSRM leveraged the cyclic design's consistent sequence to identify patterns shared across subjects. For the held-out subject (l), the basis matrix $\mathbf{W}_l$ and residual $\mathbf{S}_l$ were computed using the trained $\mathbf{R}$ as a template. Test data from the second cyclic run were then transformed via $\mathbf{W}_l$ into a reduced-dimensional shared response $\mathbf{R}_l \in \mathbb{R}^{K \times t}$. The residual $\mathbf{S}_l$, reflecting subject-specific variability, was excluded to focus on shared tactile representations. This LOSO process iterated across all subjects and both runs, ensuring robust cross-validation aligned with H3's objectives [99].

In the *second step*, a linear SVM was trained and tested on the $\mathbf{R}_l$ data. The LOSO framework prevented test subject data from influencing the shared response estimation, maintaining independence for unbiased performance evaluation. Each volume's K-dimensional projection from $\mathbf{R}_l$ served as input features, labeled by the stimulated digit (D1–D5). A one-vs-rest classification approach decoded each digit against the others, with decoding accuracy and standard error derived from two-fold cross-validation across cyclic runs and LOSO across subjects. This rigorous validation tested rSRM's ability to align high-resolution 7T fMRI data while preserving digit-specific precision. The digit classification workflow is illustrated in Figure 4.3.

The achieved decoding accuracy served as an estimate of rSRM's alignment capability under different voxel selection methods, including BAs and columnar units. Digit classification was performed separately for younger and older adults, resulting in two independent LOSO cross-validation analyses. For ROI-based analyses, regions in BAs 1, 2, 3a, 3b, 4a, 4p, and 6 in the left hemisphere (contralateral to right-hand stimulation) were analyzed, with the right hemisphere serving as a control. The top 500 voxels from each ROI were selected for optimal decoding performance. The chance

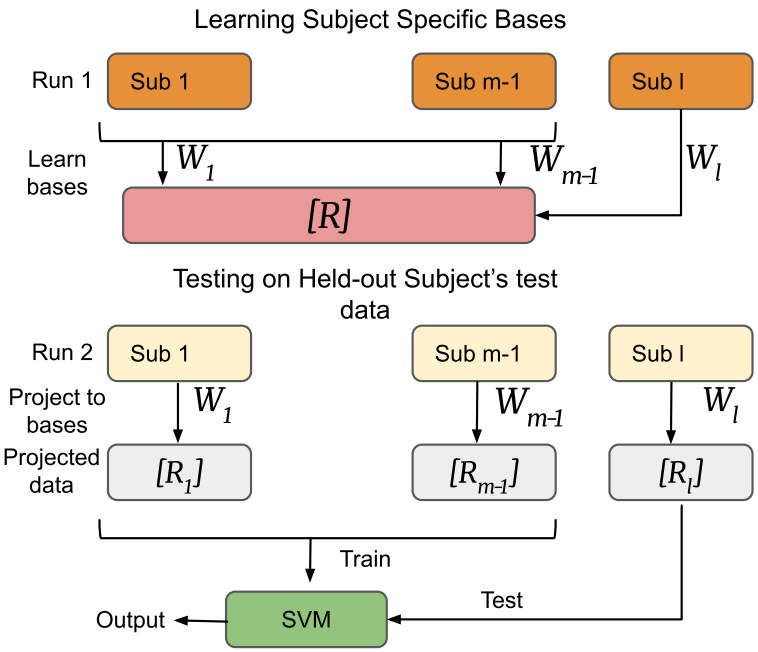

Figure 4.3 **Analytical Workflow for Digit Classification Using rSRM:** Training on $m-1$ subjects the model learns the shared response $\mathbf{R}$ and subject-specific bases $\mathbf{W}_i$ from the first cyclic run. For the held-out subject (l), $\mathbf{W}_l$ is estimated using $\mathbf{R}$ and their first-run data. Training subjects' second-run test data are projected into $\mathbf{R}_i$ via $\mathbf{W}_i$, and the held-out subject's second-run test data are projected into $\mathbf{R}_l$ via $\mathbf{W}_l$. An SVM then classifies digits from these shared responses, ensuring independence via LOSO cross-validation. *(Adapted from Chen et al. [15]).*

accuracy ($A_c(\text{chance}) = 0.2$) reflected five-digit classification, and exceeding this threshold underscored rSRM's effectiveness in aligning 7T fMRI data and decoding SI representations across both age groups.

Age Group Classification Using rSRM

To classify participants into younger (Y) and older (O) age groups and evaluate rSRM's ability to capture group-specific neural responses, we trained two distinct rSRM models—rSRM_1 for younger adults and rSRM_2 for older adults—each utilizing K latent features to derive shared representations. This approach, extending rSRM framework, generated $\mathbf{R}^{\text{young}}$ and $\mathbf{R}^{\text{old}}$ to reflect each group's unique SI tactile response patterns, supporting the focus on age-related representational differences across the 19 younger and 19 older subjects.

For rSRM_1, the first cyclic run data ($[Y_i]^{\text{train}}$) from 17 younger subjects trained $\mathbf{R}^{\text{young}}$, while for rSRM_2, $[O_i]^{\text{train}}$ from 17 older subjects trained $\mathbf{R}^{\text{old}}$. In each iteration, the 18th subject from each group (e.g., $(Y_i, i = l)$ for younger, denoted l_Y) had their first-run data ($[Y_l]^{\text{train}}$) projected into both

$\mathbf{R}^{\text{young}}$ and $\mathbf{R}^{\text{old}}$ to estimate $\mathbf{W}_{l_Y}^{\text{young}}$ and $\mathbf{W}_{l_Y}^{\text{old}}$, with residuals ($\mathbf{S}_Y$, $\mathbf{S}_O$) discarded. Their second-run data ($[Y_l]^{\text{test}}$) were transformed via these bases into $\mathbf{R}_{yl}^{\text{young}}$ and $\mathbf{R}_{yl}^{\text{old}}$, iterated over 18 subjects per group to build SVM training sets labeled "young" or "old" (green and red boxes in Figure 4.4). This process leveraged rSRM's alignment capabilities.

For each novel test subject (the 19th, denoted T), their first-run ($[T]^{\text{train}}$) and second-run ($[T]^{\text{test}}$) data were projected onto $\mathbf{R}^{\text{young}}$ and $\mathbf{R}^{\text{old}}$ using bases $\mathbf{W}_T^{\text{young}}$ and $\mathbf{W}_T^{\text{old}}$, yielding $[\mathbf{R}_T]^{\text{young}}$ and $[\mathbf{R}_T]^{\text{old}}$. These were concatenated into feature vectors for a linear SVM. The SVM was trained on the 18-subject projections and tested on each 19th subject within a leave-one-subject-out (LOSO) cross-validation framework, iterating across all 38 subjects (19 per group). The test subject's age group served as the class label, and accuracies were averaged across iterations to assess rSRM's performance, ensuring test data independence from rSRM training [99]. Individual residuals were excluded to prioritize group-specific shared responses, enhancing the SVM's focus on age-related neural differences over subject-specific variability.

4.3.4 Columnar-Shared Response Modeling (C-SRM)

The sensory and motor cortices can be segmented into columnar units, offering a framework to detect fine-grained topographic maps with the high spatial precision of 7T fMRI. In this study, we aimed to determine the optimal number of cortical columns required to decode sensory responses to passive tactile stimulation of individual fingers (D1–D5) in younger and older adults, testing H2's prediction of age-related changes in columnar organization within SI. Given the 16 distinct pin combinations per finger, the smallest functional unit may correspond to tactile representations of one or more pins rather than a single finger, necessitating a columnar approach to capture these subtleties.

We targeted contralateral BA1 and BA3b (left hemisphere for right-hand stimulation), regions known for detailed tactile representations, within the sensorimotor system. ROIs obtained from `Freesurfer` were divided into approximately equi-volume columnar units ranging from 10 to 400, with the maximum constrained by voxel size (1 mm isotropic). This segmentation was performed using the `LAYNII2` software package's `LN2_COLUMNS` command [40], which generates columns based on the middle gray matter segment derived from `LN2_LAYERS`. Structural-to-functional registration aligned T1-MRI images with 7T EPI data, defining columns *anatomically* within BA1 and BA3b's gray matter for all participants across both cyclic runs.

Post-segmentation, the mean time-series values of thresholded voxels within each column were computed, forming a columns-by-time matrix (Figure 4.5). This matrix, varying in column size with the number of divisions (10 to 400), served as input for subsequent modeling. Leveraging rSRM framework for *digit classification*, we trained C-SRM on this matrix within a cross-validation framework [15]. To identify the optimal columnar configuration, linear SVM-based LOSO decoding

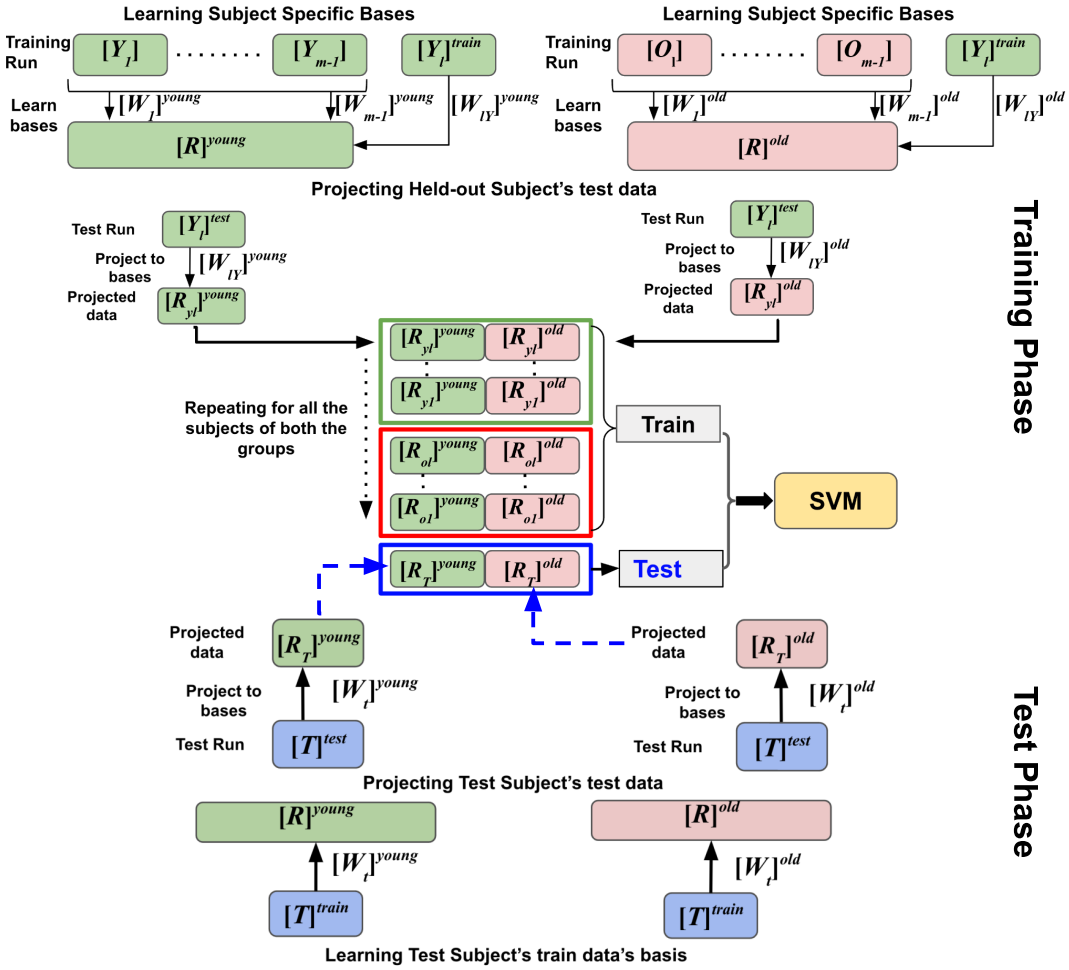

Figure 4.4 **Analytical Workflow for Age Classification Using rSRM:**
During the "training phase", separate rSRM pipelines are trained for younger (Y) and older (O) groups. Specifically, $[Y_i]^{\text{train}}$ and $[O_i]^{\text{train}}$ denote the training runs for each subject i in the younger and older cohorts, respectively, with $(Y_i, i = l)$ identifying the held-out (test) young subject. From these data, group-specific shared representations ($\mathbf{R}^{\text{young}}$ and $\mathbf{R}^{\text{old}}$) are derived, which in turn estimate subject-specific bases ($\mathbf{W}_{lY}^{\text{young}}$ and $\mathbf{W}_{lY}^{\text{old}}$) for the held-out young subject. The test run $[Y_l]^{\text{test}}$ is then projected into both $\mathbf{R}_{yl}^{\text{young}}$ and $\mathbf{R}_{yl}^{\text{old}}$, iterated for all younger subjects to form the training set for the SVM, labeled as "young" *(in green box)*. A similar procedure applies to the older group *(the red box)*. During the "test phase", a novel subject $[T]^{\text{train}}, [T]^{\text{test}}$ is projected onto both the younger and older bases, yielding $[\mathbf{R}_T]^{\text{young}}$ and $[\mathbf{R}_T]^{\text{old}}$. Concatenating these representations produces the feature vectors for an SVM that classifies the subject's age group. This framework preserves subject individuality in the training sets while discarding inter-subject variability through rSRM-based alignment.

analyses were conducted across the range of columnar divisions, decoding D1–D5 responses iteratively for each configuration.

Decoding accuracy was plotted against the number of columns, accompanied by standard deviations, to assess C-SRM's performance. A Gaussian curve was fitted to the accuracy values, with its peak indicating the optimal columnar number maximizing functional feature capture in BA1 and BA3b. This approach estimated the average columnar size required to describe somatosensory finger representations with peak accuracy, revealing age-related shifts in organization. These findings enhance our understanding of cortical columnar structure and underscore C-SRM's potential, for analyzing fine-scale functional features in the somatosensory system using UHF data.

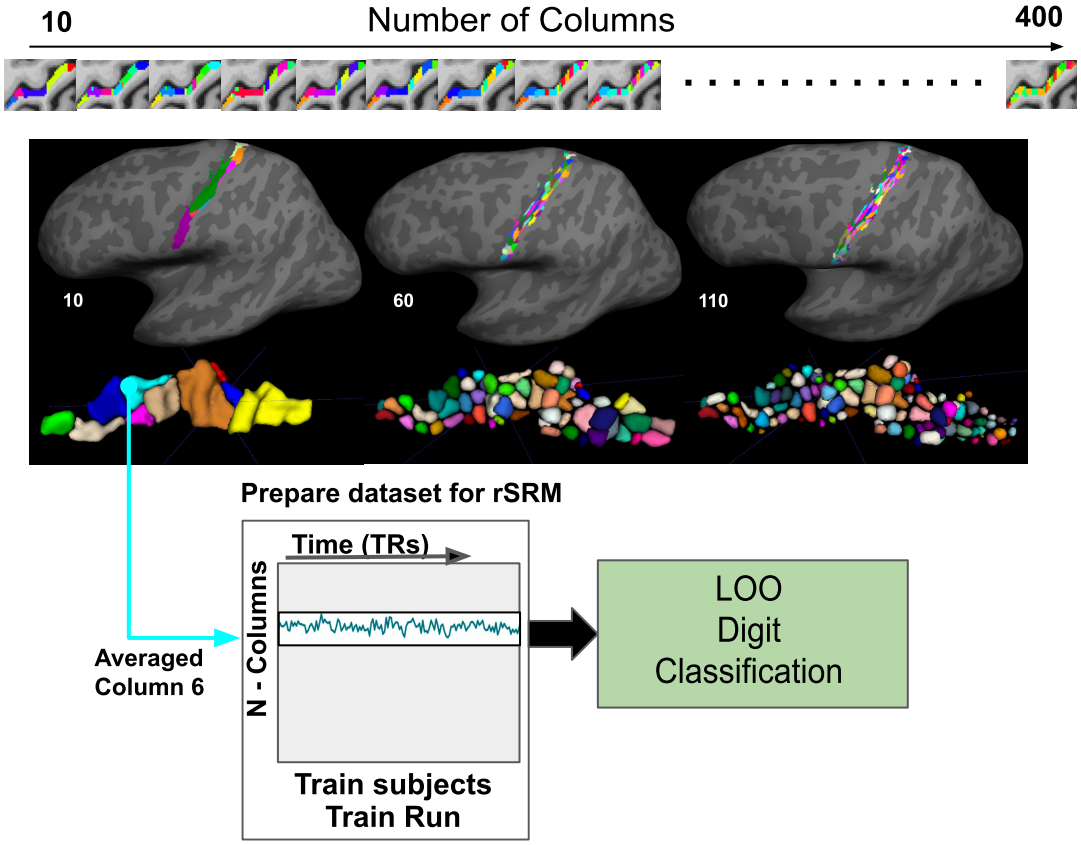

Figure 4.5 **C-SRM and Iterative Classification in BA3b:** Illustration of C-SRM in BA3b, showing projections of 10 to 400 columns and volumetric views for 10, 60, and 110 columns. A schematic depicts shared response space generation, averaging voxel time-responses within each column for two run types (D1 → D5, D5 → D1). Iterative LOSO cross-validation classifies responses across column numbers, identifying the optimal configuration for decoding. *(Adapted from Kalyani et al. [45])*

4.3.5 Statistical Analyses

To evaluate the effects of age and ROI on digit classification accuracies derived from rSRM, we conducted a two-way Analysis of Variance (ANOVA) with factors: age group (younger, older) and ROIs (BA1, BA2, BA3a, BA3b, BA4a, BA4p, BA6) in the contralateral left hemisphere. This analysis assessed the main effects of age and ROI, as well as their interaction, on digit decoding performance, focusing on ROI-specific outcomes within the sensorimotor system. Significant main effects or interactions identified by the ANOVA prompted post hoc independent-sample t-tests to pinpoint specific group or regional differences, enhancing insights into age-related precision shifts.

Statistical tests were implemented in Python using the `statsmodels` package [91], with an alpha level of $p < 0.05$ for significance. Post hoc t-tests isolated differences across age groups or ROIs, providing a detailed breakdown of ANOVA results and supporting the decoding analyses results.

To further assess the robustness of both digit and age classification models, permutation tests were performed. Target labels (digit identities or age groups) were randomly permuted to create null datasets, which were compared against the actual classification accuracies. Resulting p-values tested the null hypothesis that shared response features ($\mathbf{R}$) are independent of these labels, validating rSRM's alignment efficacy and its sensitivity to tactile representations. This non-parametric approach complemented the parametric ANOVA, ensuring a comprehensive evaluation across the 7T fMRI dataset.

For the random-design localizer data, independent-sample t-tests analyzed Euclidean distances between neighboring voxels in BA1 and BA3b, testing for significant increases along adjacent voxel pairs. This analysis, applied to thresholded voxels, validated the representational precision of neighboring activations, particularly relevant to decoding tasks and the fine-scale topography probed by C-SRM.

This statistical framework—integrating two-way ANOVA, post hoc t-tests, permutation tests, and voxel distance analyses—provided a rigorous assessment of digit and age classification models across ROIs and age groups. By leveraging both parametric and non-parametric methods, it elucidated the impacts of aging (H1) and functional topography (H2) on classification accuracy, while affirming rSRM's alignment robustness (H3) in the context of UHF 7T fMRI data.

4.4 Results

4.4.1 Finger-Specific Decoding Across Age Groups and Sensorimotor Regions

Somatosensory and motor cortices exhibit hierarchical encoding, with varying specificity to tactile stimuli across regions, reflecting topographic organization. Using rSRM, we explored finger-specific sensory representations in the contralateral left hemisphere (right-hand stimulation) across BA1, BA2, BA3a, BA3b, BA4a, BA4p, and BA6, testing H1's prediction of reduced precision in older adults and H3's validation of rSRM's alignment efficacy. The ipsilateral right hemisphere, serving as a control, showed decoding accuracies near chance (approximately 0.20) across all regions for both age groups, confirming specificity to the contralateral side (see Figure 4.6 A).

In younger and older adults, BA1 and BA3b yielded the highest mean decoding accuracies (BA1: younger, 0.46 ± 0.12; older, 0.45 ± 0.10; BA3b: younger, 0.47 ± 0.12; older, 0.42 ± 0.10), followed by BA2 (younger, 0.43 ± 0.09; older, 0.39 ± 0.10), BA4a (younger, 0.36 ± 0.08; older, 0.32 ± 0.10), and BA4p (younger, 0.35 ± 0.09; older, 0.31 ± 0.07). Lower accuracies emerged in BA6 (younger, 0.29 ± 0.06; older, 0.26 ± 0.06) and BA3a (younger, 0.32 ± 0.09; older, 0.24 ± 0.04) (Figure 4.6, panel A). These results, derived from 7T fMRI data, align with prior evidence of precise topographic finger maps in BA3b and BA1 for younger adults [89], extending this observation to older adults for the first time.

A two-way ANOVA assessed the influence of age group (younger, older) and ROI (BA1, BA2, BA3a, BA3b, BA4a, BA4p, BA6) on digit classification accuracies, revealing a significant main effect of age ($F(1) = 14.13,\ p = 2.12 \times 10^{-4}$), a significant main effect of ROI ($F(6) = 27.78$, $p = 2.17 \times 10^{-25}$), and no significant age-ROI interaction ($F(6) = 0.49$, $p = 0.815$) (Figure 4.6, panels B, C). The age effect indicated lower overall accuracies in older adults (mean: 0.34 ± 0.10) compared to younger adults (mean: 0.38 ± 0.11), consistent with H1's hypothesis of reduced representational precision with aging.

Post hoc t-tests identified hierarchical differences. In BA3b, accuracies significantly exceeded those in BA3a ($t(74) = 7.52,\ p = 1.02 \times 10^{-10}$), BA4a ($t(74) = 4.43,\ p = 3.16 \times 10^{-5}$), BA4p ($t(74) = 5.18,\ p = 1.87 \times 10^{-6}$), and BA6 ($t(74) = 8.44,\ p = 1.93 \times 10^{-12}$). Similarly, BA1 outperformed BA3a ($t(74) = 8.09,\ p = 8.61 \times 10^{-12}$), BA4a ($t(74) = 5.87,\ p = 3.02 \times 10^{-7}$), BA4p ($t(74) = 6.42$, $p = 9.15 \times 10^{-8}$), and BA6 ($t(74) = 9.16$, $p = 2.41 \times 10^{-13}$). BA2 also showed higher accuracies than BA4a ($t(74) = 3.51$, $p = 7.68 \times 10^{-4}$), BA4p ($t(74) = 4.31$, $p = 5.02 \times 10^{-5}$), and BA6 ($t(74) = 7.94$, $p = 1.66 \times 10^{-11}$) (Figure 4.6, panel B). These pairwise contrasts highlight a preserved processing hierarchy across the sensorimotor cortex.

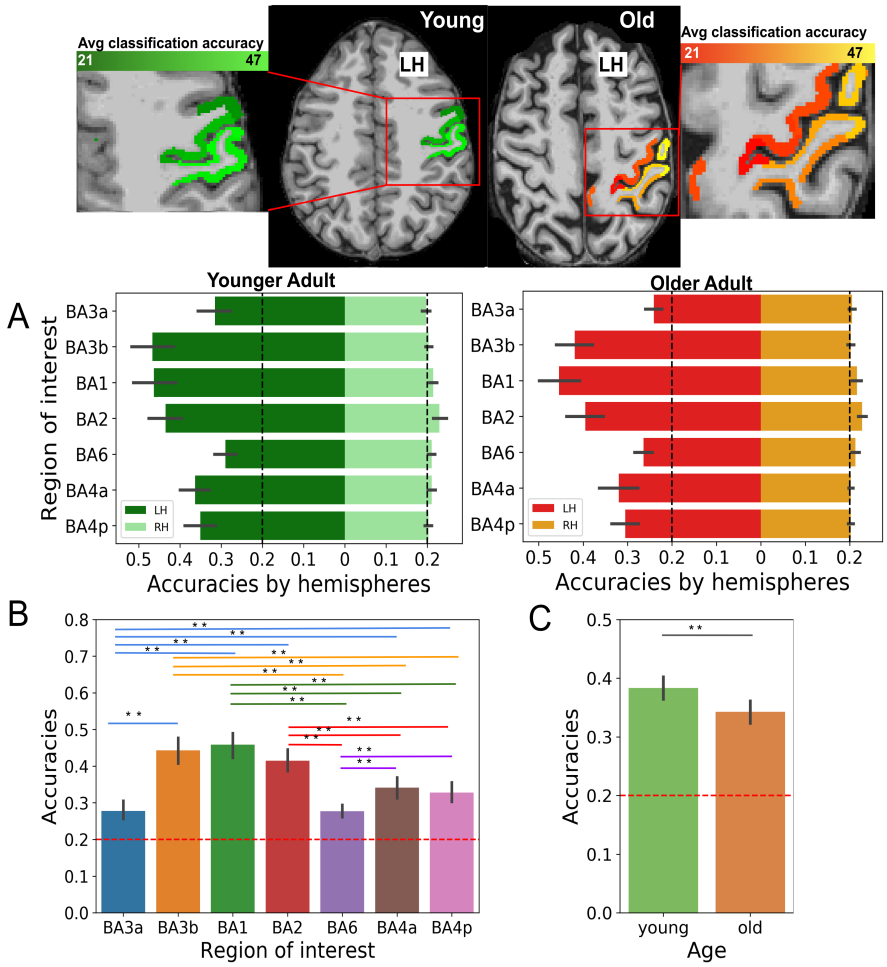

Figure 4.6 **Digit Decoding Accuracy Across Sensorimotor Regions in Younger and Older Adults:** (A) Bar plots display ROI-based decoding accuracies for D1–D5 stimulation in left (contralateral) and right (control) hemispheres for younger (green) and older (red) adults, with brain maps (top row) showing average accuracies. Dashed line denotes chance level (0.2, 5 digits). (B) Main effect of ROI on decoding accuracy, with colors representing BAs; *$p < 0.05$, **$p < 0.005$. (C) Main effect of age group (younger, green; older, orange), **$p < 0.005$, highlighting reduced precision in older adults. *(Adapted from Kalyani et al. [45])*

In summary, these findings reveal a consistent hierarchy where BA1 and BA3b exhibit the most precise digit decoding, validated by rSRM's alignment (H3), with a notable decline in older adults' accuracies across all BAs (H1). This suggests age-related changes in somatosensory precision while retaining topographic organization, extending prior insights [89, 57] with high-resolution 7T fMRI data.

4.4.2 Age-Related SI Topography Changes via rSRM Decoding

This subsection leverages rSRM to perform across-run digit and age classification, delving deeper into age-related changes in SI architecture beyond the general accuracy declines observed in previous section (Section 4.4.1). Here, we focus on specific features driving these differences, testing H1's prediction of reduced representational precision and H3's validation of rSRM's alignment efficacy in younger and older adults using 7T fMRI data.

First, we assessed how the number of significant voxels impacts digit decoding accuracy, analyzing younger and older adults separately. Increasing voxel counts expanded the feature space, enhancing the shared response's ability to capture variance. In younger adults, 500 voxels with 5 features yielded a mean accuracy of 0.42 ± 0.14, while 3000 voxels with 100 features achieved similar results (Figure 4.7, panel A). Older adults followed a comparable trend, though with lower accuracies, reflecting age effect. For ROI-based analyses, we selected an optimal $n = 500$ voxels and $k = 10$ features, balancing shared variance capture across subjects and computational time (as k is inversely proportional to computational time [15]) (Figure 4.7, panels A, B).

Using these parameters, we compared rSRM-based decoding against unaggregated time-series decoding for digits and age groups via LOSO cross-validation with SVM. For digit decoding, rSRM outperformed unaggregated methods: younger adults achieved 0.47 ± 0.11 (rSRM) vs. 0.29 ± 0.06 (unaggregated), and older adults 0.44 ± 0.16 (rSRM) vs. 0.23 ± 0.04 (unaggregated) at 500 voxels, $k = 200$ (Figure 4.7, panel C). This confirms rSRM's superior capture of shared tactile information. For age group decoding, rSRM averaged 0.90 ± 0.05, well above chance (0.5), matching dual-model results (0.90 ± 0.05) and highlighting group-specific feature extraction (Figure 4.7, panel D). With $k = 50$, left hemisphere accuracies (0.84 ± 0.26) exceeded right hemisphere (0.69 ± 0.31) (Figure 4.8, panel B), suggesting increased bilateral activation in older adults [8].

Permutation tests validated these findings: unaggregated time-series showed weak label dependency ($p = 0.068$), while rSRM features were significantly stronger ($p = 0.001$), affirming non-chance age classification (H3). Next, we calculated Euclidean distances in the shared feature space to identify age-specific topography changes. For both groups, same-digit distances were smaller than between-digit distances, indicating that digit-specific representations were maintained in the shared space (Figure 4.9, panel A). Distances increased across first (11.24 ± 2.43 younger; 8.73 ± 2.72 older), second (12.94 ± 2.45 younger; 9.99 ± 3.18 older), and third neighbors (14.77 ± 2.56 younger; 11.44 ± 3.88 older), dropping at the fourth (13.35 ± 2.44 younger; 10.07 ± 2.99 older), likely due to cyclic D5-D1 stimulation order, as D5 and D1 were directly stimulated in succession (Figure 4.9, panel B).

Random-design data analysis showed no significant distance increase beyond the third neighbor (younger: $t(18) = 1.66$, $p = 0.11$; older: $t(18) = 0.86$, $p = 0.40$) (Figure 4.12), with younger adults

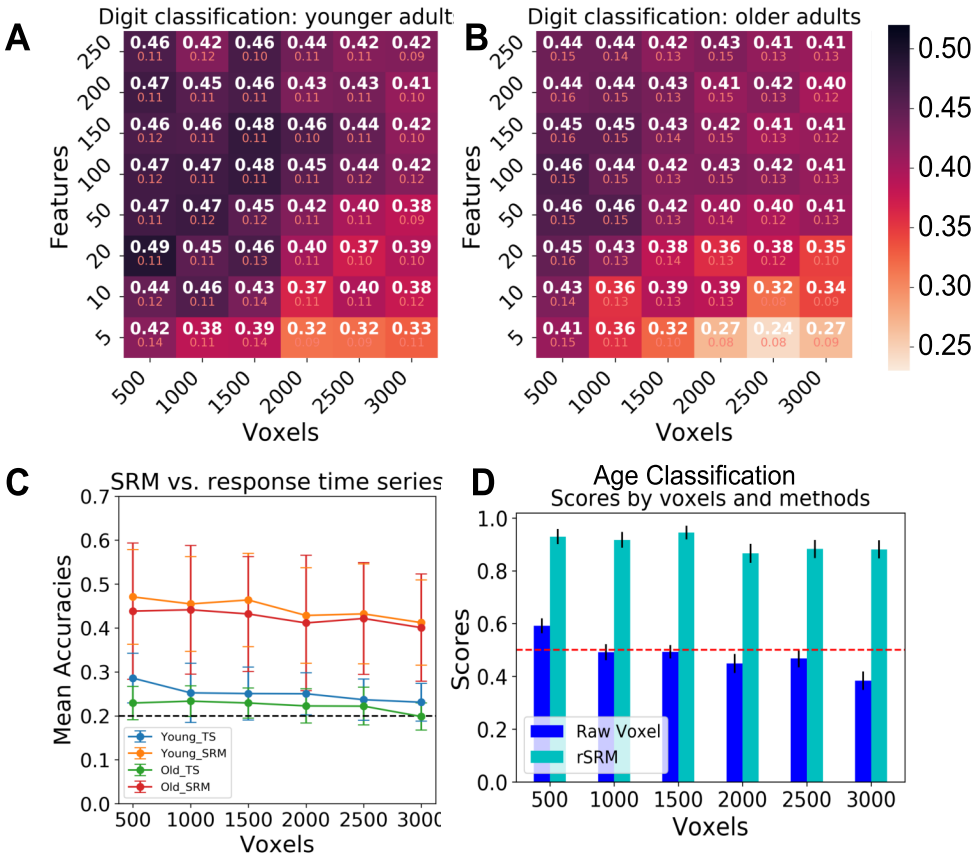

Figure 4.7 **rSRM Parameter Optimization and Decoding Performance:**
(A) Heatmap of mean digit decoding accuracies and standard deviations(SD) in younger adults across voxel and feature counts. (B) Same for older adults, showing optimal $n = 500$, $k = 10$ balancing variance and computational time. (C) Line plots of digit decoding accuracy: unaggregated time-series (blue: younger, green: older) vs. rSRM-based (orange: younger, red: older) at $k = 200$, with SD error bars. (D) Bar plots of age group decoding accuracy: unaggregated (blue) vs. rSRM-based (cyan), with standard error (SEM) error bars, chance = 0.5. *(Adapted from Kalyani et al. [45])*

consistently exhibiting higher distances for both cyclic and random design stimulations (Figure 4.9, D, and Figure 4.12).

Taken together, these results indicate that:

1. Digit decoding accuracy is generally lower for older adults compared to younger adults.

2. In the shared space, sample points representing different digits are more closely clustered to themselves, a pattern observed across both age groups (Figure 4.9, panel A).

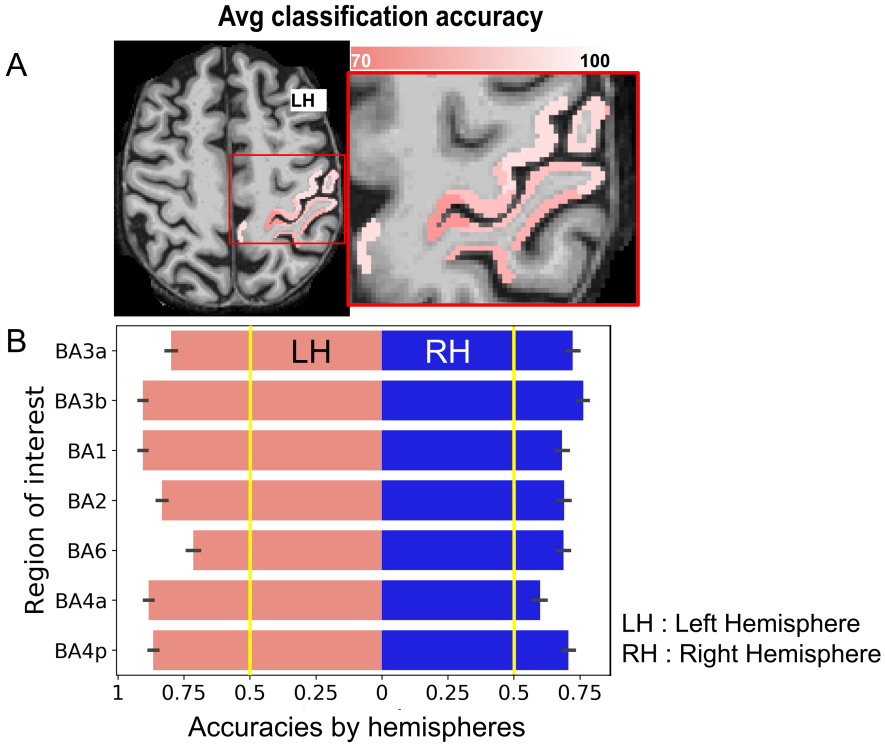

Figure 4.8 **Age Group Decoding Across Hemispheres:** (A) Brain maps (top) show mean age classification accuracies in the left hemisphere (contralateral to right-hand stimulation). (B) Bar plots compare left (contralateral) vs. right (ipsilateral) hemisphere accuracies using rSRM, with SEM error bars and chance level (0.5, yellow line), indicating bilateral effects in older adults. *(Adapted from Kalyani et al. [45])*

3. Euclidean distances between representations are lower for older adults, suggesting reduced separation between digit representations.

4. Chance-level digit decoding and lower age-group accuracy in the ipsilateral hemisphere, indicating that classification is driven by features corresponding to digit stimulation and not random factors (Figure 4.8, panel B).

4.4.3 Columnar Organization in SI: Age Effects via C-SRM

Extending the rSRM results, we next used C-SRM to probe the columnar architecture of SI at 7T. By iteratively partitioning BA 1 and BA 3b into successively finer column grids [39, 110, 109], we asked how many columns best decode finger-specific responses during passive touch in younger versus older adults—thereby testing H2 on age-dependent changes in column width.

Focusing on contralateral BA1 and BA3b (left hemisphere, right-hand stimulation), we segmented these ROIs into 10 to 400 approximately equi-volume columns using `LAYNII` and plotted decoding

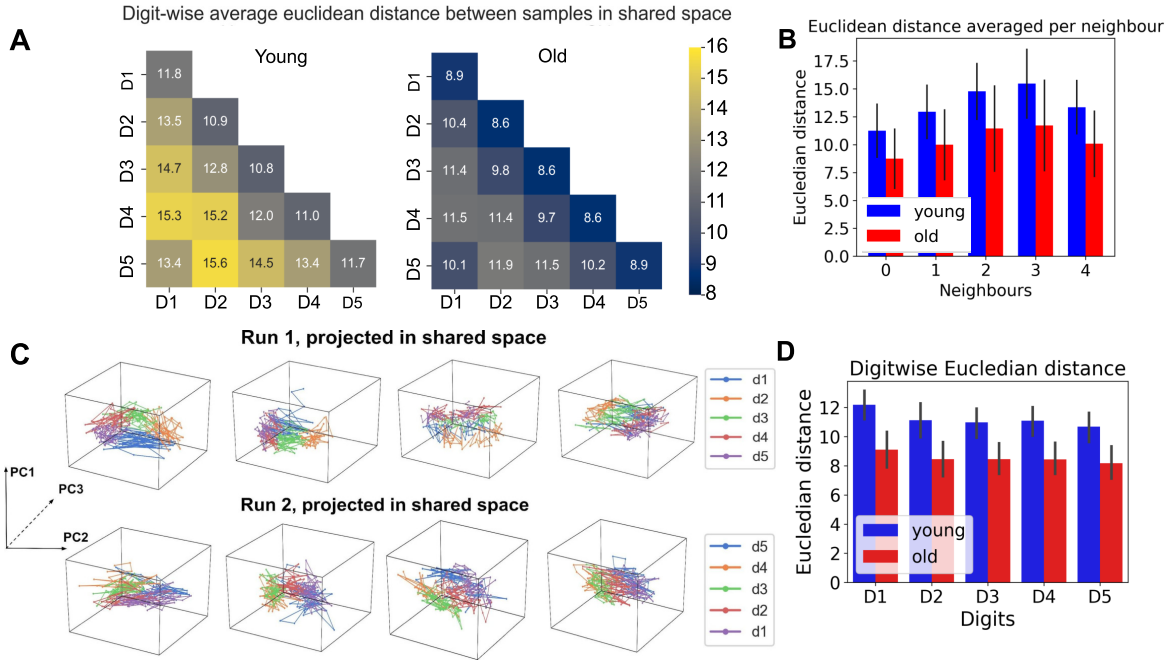

Figure 4.9 **Representation of Digit-Specific Shared Response Patterns in Younger and Older Adults:** (A) Heatmap of Euclidean distances (rSRM, $k = 5$) shows digit clustering and neighbor gradients. (B) Bar plots of distances by neighbour order (younger: blue, older: red), with SD error bars, reflecting D5-D1 order effect. (C) PCA visualization of the shared response in a 3D representational space, demonstrating the circular arrangement of digits across different subjects. NOTE: PCA was used purely for visualization purposes. (D) Digit-wise distances compare younger vs. older adults, with SEM error bars. *(Adapted from Kalyani et al. [45])*

accuracies against column counts, fitting Gaussian curves to identify peak performance. Decoding accuracies were higher in BA1 than BA3b across both age groups (Figure 4.10, panels A, B), with optimal columnar sizes differing in BA1 but consistent in BA3b. Note that "columnar size" here denotes functional units derived from T1-based modeling via `LAYNII`, not anatomically defined columns tied to structural properties like myelination [24], as this approach does not account for T1 variations across cortical areas.

In BA1, younger adults required more columns for optimal decoding (70 columns, average size: $44.26 \pm 5.06\,\text{mm}^3$) than older adults (60 columns, average size: $45.47 \pm 5.55\,\text{mm}^3$), suggesting finer computational units in the younger group. In BA3b, both groups peaked at 110 columns (younger: $28.94 \pm 3.51\,\text{mm}^3$; older: $24.49 \pm 2.40\,\text{mm}^3$), with a reference scale of $\sim 27\,\text{mm}^3$ approximating a 3x3x3 mm cube (Figure 4.10, panels A, B). These findings, combining rSRM's funtional alignment with columnar segmentation, introduce C-SRM as a novel tool to pinpoint the smallest functional units of finger differentiation in SI.

In BA3b, the stable 110-column optimum across age groups suggests robust topographic representation of finger-specific units, potentially reflecting consistent sub-finger pin responses. Conversely, BA1's age divergence (70 vs. 60 columns) indicates that younger adults may sustain higher precision or less noise in columnar organization, aligning with age related precision decline and supported by rSRM's alignment efficacy (H3; Figure 4.10, right panels). These differences, explored further in the Discussion, highlight C-SRM's potential to reveal functional columnar variations in SI using UHF data, extending prior high-resolution studies [39, 110].

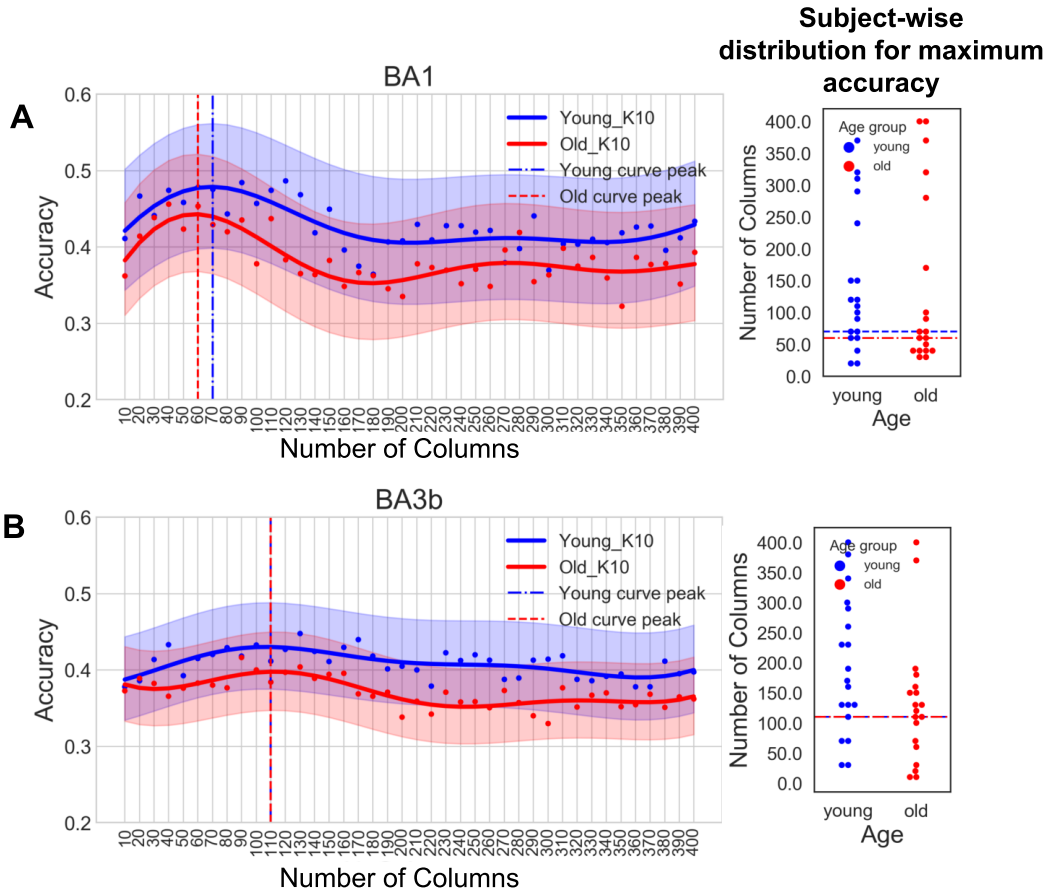

Figure 4.10 **Columnar-Shared Response Modeling: Digit Decoding in BA1 and BA3b:** (A) Mean digit decoding accuracies (solid lines) and standard deviations (shaded areas) across column counts in BA1 for younger (blue) and older (red) adults, with dashed lines marking optimal columns (70 vs. 60; H2). Right: Subject-wise peak distributions (Gaussian smoothing, window = 6). (B) Same for BA3b, showing consistent 110-column optimum across groups (H2). Results from C-SRM using LOSO cross-validation. *(Adapted from Kalyani et al. [45])*

4.5 Extended Analyses and Supporting Results

4.5.1 Application of rSRM to Random Design Data

Methodology

Analyzing fMRI data from random stimulation designs poses challenges due to inconsistent stimulation order, which can obscure shared stimulus-specific responses across subjects. To address this, we re-ordered the blocked-design fMRI time series from the random runs to synchronize brain states, enhancing alignment of shared neural responses for rSRM analysis. This preprocessing step, applied to 7T fMRI data, facilitated accurate decoding by aligning digit-specific temporal patterns across participants (Figure 4.11).

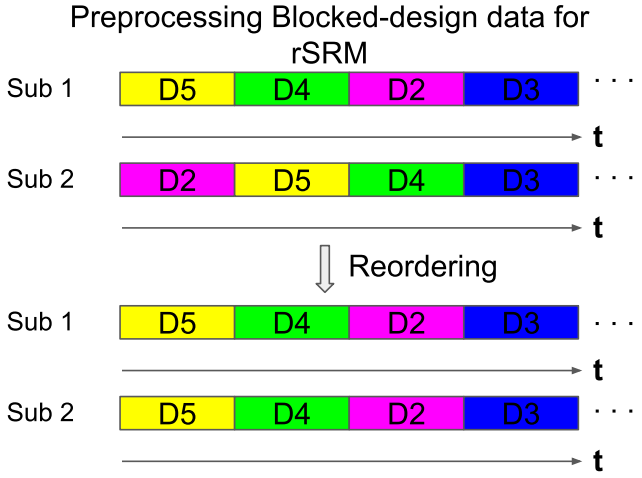

Figure 4.11 **Synchronizing Blocked-Design fMRI for rSRM Analysis:** Illustration of time-series re-ordering for two example subjects (Sub 1, Sub 2), with colors denoting digit stimulations (D1–D5). Different colors represent different digit stimulations, demonstrating the temporal alignment of digit-specific responses across subjects. This preprocessing step ensures synchronization of the time series for effective shared response estimation in subsequent analyses. *(Adapted from Kalyani et al. [45])*

Post-reordering, we trained the rSRM model on one run's data, constructing a shared response template with $K = 5$ features optimized via LOSO cross-validation to capture shared variance across subjects. The template was tested on the left-out run, transforming its data into the shared space. A linear SVM then performed LOSO classification on this transformed data, evaluating rSRM's ability to decode digit-specific patterns.

To probe the shared response space's structure, we computed Euclidean distances between sample points for digits D1–D5 in the 5-dimensional feature space. Average distances between neighboring digits (e.g., D1-D2, D2-D3) were calculated, and paired t-tests assessed significant increases across

adjacent pairs. These results, visualized in Figure 4.12, reveal how rSRM captures stimulus-specific topography in random-design data, addressing alignment challenges and supporting H3.

Results

Digit classification on the re-ordered random-design data achieved mean accuracies of approximately 45% (0.45 ± 0.09) for younger adults and 33% (0.33 ± 0.07) for older adults, exceeding chance (0.2) and indicating effective decoding of digit-specific patterns (H1; Figure 4.12, panels C, F). Permutation tests across multiple subjects showed over 75% achieved scores significantly above chance ($p < 0.05$), with actual accuracies (red dots) consistently outperforming permuted distributions (Figure 4.12, panels C, F), supporting rSRM's reliability.

Euclidean distance analysis in the 5-dimensional shared space ($K = 5$) revealed stable representational patterns. For younger adults, distances were 5.93 ± 1.2 (third neighbor) and 6.0 ± 1.3 (fourth neighbor; $t(18) = 1.66$, $p = 0.11$); for older adults, 4.01 ± 0.9 (third) and 4.03 ± 1.0 (fourth; $t(18) = 0.86$, $p = 0.40$) (Figure 4.12, panels B, E). No significant increase occurred beyond the third neighbor, suggesting a plateau in topographic separation consistent with cyclic-run findings (Section 4.4.2), though younger adults showed higher distances, aligning with H1's precision decline.

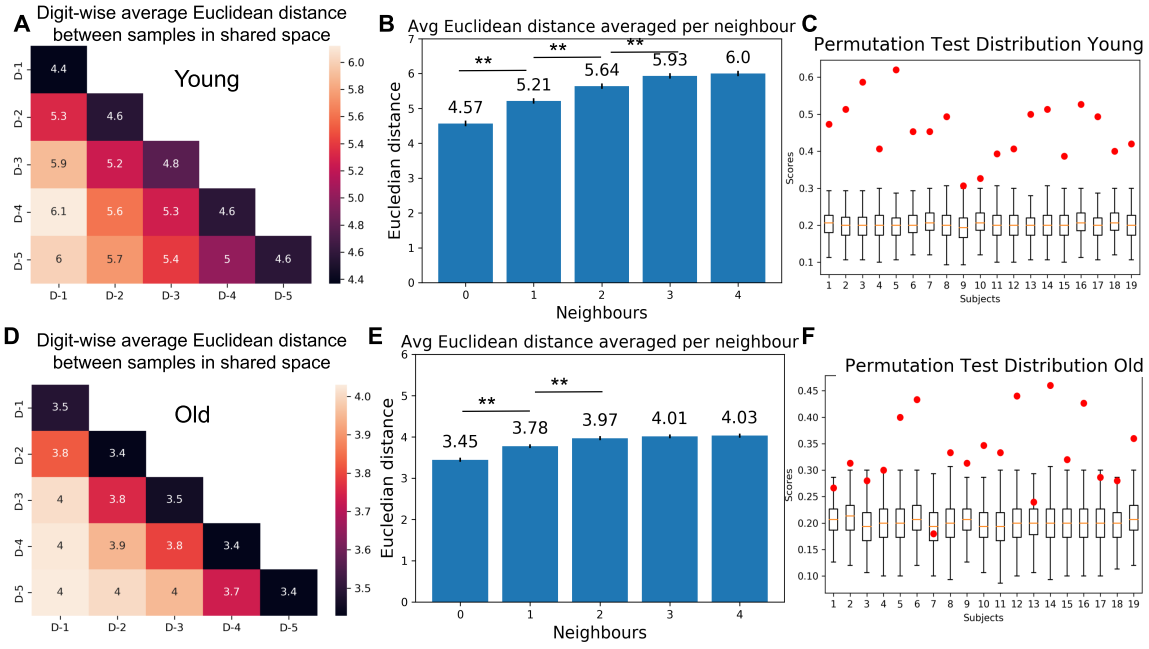

Figure 4.12 **Digit Topography and Classification in Random-Design Data:** (A, D) Heatmaps of Euclidean distances between re-ordered digit responses (rSRM, $K = 5$) for younger (A) and older (D) adults. (B, E) Bar plots of distances by neighbor order, with SEM error bars and means labeled. (C, F) Box plots of 1000 permutation test scores vs. actual accuracies (red dots) for younger (C) and older (F) adults, showing significant above-chance performance. *(Adapted from Kalyani et al. [45])*

4.5.2 Comparative Performance: Anatomical Alignment, rSRM, and C-SRM

Methodolody

To compare anatomical alignment (AA) with rSRM and C-SRM, we aligned T1-weighted MRI data using Advanced Normalization Tools (ANTs) [5] to the MNI152 1mm template, establishing a shared anatomical space as a baseline for decoding (H3). The preprocessing pipeline involved FreeSurfer-assisted skull stripping [30] and high-quality registration via the SyN algorithm, followed by co-registration of 7T functional data to these aligned anatomical images.

The BA3b ROI, defined using the Glasser atlas [33] and dilated for coverage across subjects, was extracted from the aligned dataset. Time-series data within this ROI were analyzed for digit decoding (D1–D5) using LOSO cross-validation with a linear SVM. Decoding accuracies, alongside computational times, were recorded and compared against rSRM and C-SRM results, evaluating performance and efficiency across these approaches (Table 4.1).

Results

The comparative analysis of AA, rSRM, and C-SRM across dimensions is detailed in Table 4.1. Anatomical alignment yielded a decoding accuracy of 0.31 ± 0.05, requiring 17,184 seconds (approx 4.77 hours), reflecting its computational intensity due to extensive registration processes. In contrast, rSRM improved with increasing dimensions: accuracies ranged from 0.44 ± 0.05 (100 sec) to 0.46 ± 0.05 (253 sec), peaking at 0.45 ± 0.04 (309–563 sec), then slightly declining to 0.43 ± 0.03 (2149 sec), showcasing its ability to capture shared stimulus-specific information.

C-SRM delivered stable accuracies across column counts: 0.38 ± 0.02 (41 sec), 0.40 ± 0.02 (45 sec), 0.39 ± 0.01 (45 sec), 0.40 ± 0.02 (52 sec), and 0.39 ± 0.02 (67 sec), outperforming AA in accuracy and efficiency while requiring significantly less computational time than rSRM (Table 4.1). rSRM consistently achieved higher accuracies, aligning with H3's alignment superiority, whereas C-SRM balanced moderate accuracy with rapid processing, supporting H2's columnar focus with practical utility.

These results highlight rSRM's precision in decoding digit representations (H1, H3) and C-SRM's efficiency for columnar analysis (H2), with AA as a computationally heavier baseline. The choice of method can therefore be tailored to the specific demands of a given research context.

Dimensions→ Methods↓	**10**	**60**	**70**	**110**	**250**
AA	S: 0.31 ± 0.05; T: 17,184 sec				
rSRM	S: 0.44 ± 0.05 T: 100 sec	S: 0.46 ± 0.05 T: 253 sec	S: 0.45 ± 0.04 T: 309 sec	S: 0.45 ± 0.04 T: 563 sec	S: 0.43 ± 0.03 T: 2149 sec
C-SRM	S: 0.38 ± 0.02 T: 41 sec	S: 0.40 ± 0.02 T: 45 sec	S: 0.39 ± 0.01 T: 45 sec	S: 0.40 ± 0.02 T: 52 sec	S: 0.39 ± 0.02 T: 67 sec

Table 4.1 Comparative Performance of Alignment Methods in BA3b Decoding. Table compares decoding accuracies (S, mean ± SD) and computational times (T, seconds) for AA, rSRM, and C-SRM across dimensions (10–250) in BA3b. rSRM excels in accuracy, while C-SRM balances accuracy and efficiency. *(Adapted from Kalyani et al. [45])*

4.6 Discussion

This study employed rSRM and introduced a novel C-SRM approach to probe finger-specific representations in the somatosensory cortex of younger and older adults using UHF (7T) fMRI. The overall findings indicate that the hierarchical architecture of somatosensory processing persists across age groups, in line with previous work identifying BA1 and BA3b as critical for precise tactile encoding [57, 89]. Nevertheless, the lower digit-classification accuracies observed in older adults across BAs suggest that aging diminishes representational sharpness, a result that cannot be accounted for by variations in tactile thresholds (as these were individually calibrated).

Quantification of representational distance further supports this decline in fidelity among older adults, evidenced by reduced Euclidean distances among digit-evoked responses. Notably, C-SRM revealed distinct patterns in BA1, wherein older adults showed fewer, larger columnar units than younger adults, possibly implicating broader receptive fields or diminished intracortical inhibition [77]. By contrast, BA3b's optimal columnar configuration appeared robust to age-related changes—maintaining an approximately consistent number of columns, akin to prior findings on stable sub-finger representations [89, 109, 110].

The ROI analyses extend earlier insights into the hierarchical processing of tactile inputs, confirming that BA2 integrates signals from BA3b and BA1, leading to complex receptive fields [57]. Additionally, while motor areas such as BA4a and BA4p also contributed to digit classification, their involvement was somewhat less pronounced. Ipsilateral decoding remained near chance for most regions in both age groups, though older adults exhibited a modest above-chance performance in certain areas, potentially reflecting compensatory bilateral mechanisms consistent with the HAROLD model [10].

Methodologically, rSRM significantly outperformed unaggregated time-series decoding approaches by learning a shared space that effectively captures both digit- and age-specific variance [8].

The contralateral hemisphere showed higher accuracies, unsurprisingly, given its direct involvement in tactile processing. C-SRM added a valuable dimension to the analysis, allowing quantification of how columnar-scale tuning might shift across the lifespan. While BA1 clearly diverged between younger and older groups, BA3b remained more constant, underscoring differential susceptibility among somatosensory subregions [21, 13].

These results raise intriguing questions regarding the anatomical correlates of these functional columns, including whether certain myeloarchitectonic signatures align with the larger or smaller columnar units observed in different age groups [24]. Additionally, the chosen 1 mm voxel resolution, while enabling high-fidelity classification, does not necessarily capture the full sub-millimeter scale of cortical layers [109, 110]. Future imaging protocols may explore deeper laminar or myelin-sensitive contrasts to elucidate the structural underpinnings of these functional maps.

4.7 Conclusion

Through the combined application of UHF (7T) fMRI, rSRM, and C-SRM, this chapter demonstrates both the robustness of hierarchical somatosensory processing and the subtle, yet significant, decline in digit-specific precision among older adults. While BA3b retains a stable columnar structure, BA1 reveals age-dependent shifts, requiring fewer columnar units in older adults. These findings not only validate the rSRM framework's ability to capture fine-scale features but also highlight the utility of C-SRM for examining how columnar organization changes with age.

By integrating these multivariate approaches, future research can delve further into the structural correlates of these functional columns, possibly leveraging higher spatial resolution or novel imaging contrasts. Moreover, the methods and insights gained here could inform broader clinical studies on age-related sensory decline or serve as a baseline for exploring neurodegenerative conditions that affect somatosensory organization. In essence, this work underscores the potential of advanced dimensionality reduction and functional alignment strategies for mapping the intricacies of cortical representations and how they evolve across the human lifespan.

Chapter 5

Amyotrophic Lateral Sclerosis-Related Functional Changes

5.1 Introduction

ALS often referred to as Lou Gehrig's disease—is a progressive neurodegenerative disorder that selectively targets both UMNs in the motor cortex and LMNs in the brainstem and spinal cord [2, 29]. This dual patholog y manifests in a range of symptoms, from muscle weakness and atrophy to spasticity and eventual paralysis, often culminating in respiratory failure. Symptom onset is typically focal: it may begin with bulbar impairments (affecting speech and swallowing), with upper limb dysfunction, or with lower limb difficulties, before progressively involving widespread motor pathways [82]. The median survival time is commonly three to five years, though this varies according to disease subtype and progression.

Clinically, ALS is heterogeneous and ALS typically spreads from an initially affected focal region to other areas of the motor system, ultimately leading to generalized motor impairment and respiratory failure [69]. Despite extensive research, no cure exists; current treatments modestly prolong survival and alleviate symptoms [11].

Neuroimaging has been instrumental in uncovering both structural and functional aspects of ALS pathology. For instance, magnetic resonance studies have revealed microstructural alterations such as iron accumulation in deeper cortical layers of the MI in regions initially affected by the disease [18]. Conversely, calcium deposits often appear more diffusely in upper cortical layers, while low-myelin borders—which normally demarcate the transitions between body part representations—tend to degenerate early, undermining the functional topography of MI [56, 70]. However, although structural lesions are increasingly well-documented, the corresponding *functional* disruptions remain less understood.

Resting-state fMRI studies suggest that network-level functional changes, such as altered sensorimotor connectivity, might precede overt structural damage [98]. These findings raise the possibility of detecting early functional biomarkers that could track disease progression more dynamically. Yet, fMRI data in ALS is challenging to interpret: patients may have difficulty remaining still, and symptom heterogeneity can reduce group-level coherence in traditional voxelwise analyses.

UHF (7T) fMRI and advanced multivariate analysis techniques, offers an opportunity to overcome these issues by providing higher spatial and temporal resolution, and better data aggregation techniques [6]. This makes it possible to discern finer-scale activity patterns that might be pivotal for identifying the earliest functional alterations in ALS. Despite its promise, 7T-fMRI has been employed in relatively few ALS studies, with most investigations focusing on structural assessments rather than capturing neural activation and connectivity profiles.

Recent computational advances, particularly rSRM and PLSR, can help parse these high-dimensional datasets [45, 99]. rSRM aligns individual subject data into a shared low-dimensional space, potentially improving the classification of ALS patients versus healthy controls by highlighting common and individual disease-driven signals. Meanwhile, PLSR relates large-scale brain patterns to clinical metrics such as the ALSFRS-R and Penn Upper Motor Neuron Score (PUMNS) [11, 80]. Taken together, these methods may help distinguish whether functional alterations in ALS are localized to specific cortical zones (topographic) or diffused across motor regions (atopographic).

This study aims to:

1. Classify ALS patients vs. controls using rSRM-based task-related sensorimotor activation (H4a).

2. Differentiate topographic (first-affected region) vs. atopographic functional changes in MI (H4b).

3. Identify latent variables reflecting disease severity and onset site via PLSR, comparing functional activation and connectivity (H5).

5.2 Population and Study Design

5.2.1 Pariticpants

Functional MRI data were acquired using 7T MRI from 14 ALS patients (6 females, mean age = 56.07 years, SD = 15.62) and 12 age-matched healthy controls (6 females, mean age = 61.1 years, SD = 11.9). Patients were recruited from University Hospitals in Magdeburg, Jena, and Dresden between June 2018 and January 2024, scanned post-diagnosis. Controls, sourced from the DZNE database in

Magdeburg, Germany, were matched to 12 ALS patients by age (±2 years; $t(22) = -0.15$, $p = 0.883$), handedness, gender, and education (patients: mean = 14.5 years, SD = 2.7; controls: mean = 15.4 years, SD = 2.7; $t(22) = -0.82$, $p = 0.422$). Two patients lacked matched controls due to a scanner software update.

Participants underwent 7T MRI scans and behavioral assessments, with ALS patients receiving clinical evaluations from a neurologist. The ALS cohort included 8 upper limb (UL), 3 lower limb (LL), and 3 bulbar (B, bilateral) onset cases (Table 5.1). Three patients (P1, P4, P6) had follow-up scans: P1 (5 months), P6 (7 months), P4 (8 months, 2 years 4 months). Controls were excluded for sensorimotor deficits, neurological disorders, or 7T MRI contraindications. All provided informed consent and were compensated, with the study approved by the Ethics Committee of the Medical Faculty at the University of Magdeburg.

Patient	Age	Gender	Control	Limb Onset	ALSFRS-R	King's Stage	PUMNS
P1*	50	F	Yes	UL	44	2A	1
P2	74	F	Yes	LL	25	3	22
P3	36	M	Yes	LL	45	2A	15
P4*	48	M	Yes	UL	37	2B	2
P5	53	M	Yes	B	33	3	2
P6*	66	M	Yes	UL	41	2B	3
P7	60	M	Yes	UL	40	2A	11
P8	52	F	Yes	UL	42	2B	16
P9	64	F	Yes	B	47	2A	1
P10	77	F	Yes	UL	35	2A	0
P11	72	F	Yes	B	46	2A	1
P12	73	M	Yes	UL	34	2B	9
P13	25	M	No	UL	33	3	7
P14	35	M	No	LL	17	3	12

Table 5.1 Clinical and Demographic Details of ALS Cohort. Columns list patient ID, age, gender (F = female, M = male), control matching (Yes/No), onset type (UL = upper limb, LL = lower limb, B = bulbar), ALSFRS-R score (lower = greater impairment), King's stage (2A = one region, 2B = two regions, 3 = three regions), and PUMNS score (higher = greater UMN dysfunction). *Patients with multiple scans. *(Reproduced from Kalyani et al. [46])*

5.2.2 MRI Scanning Protocol

Functional and structural MRI data were acquired using a 7 Tesla MRI scanner (Siemens Healthineers) equipped with a 32-channel head coil (Nova Medical Inc.) at Otto-von-Guericke University, Magdeburg, Germany. Each participant underwent a single scanning session that included whole-brain anatomical imaging and functional imaging during motor tasks.

Structural imaging used MP2RAGE sequences with 0.7 mm isotropic resolution. The acquisition parameters included a TR of 4800 ms, an TE of 2.01 ms, a FOV of 224 mm, flip angles of 5° and 3°, and inversion times of 900 ms and 2750 ms. A bandwidth of 250 Hz/Px was used to enhance image quality. Functional imaging employed a GE-EPI sequence for BOLD contrast, acquiring 81 slices at 1.5 mm isotropic resolution. The acquisition parameters included a TR of 2000 ms, TE of 25 ms, an FOV of 212 mm, interleaved slice acquisition, a parallel imaging acceleration factor (GRAPPA) of 2, and a Simultaneous Multi-Slice (SMS) factor of 2 to enhance temporal resolution.

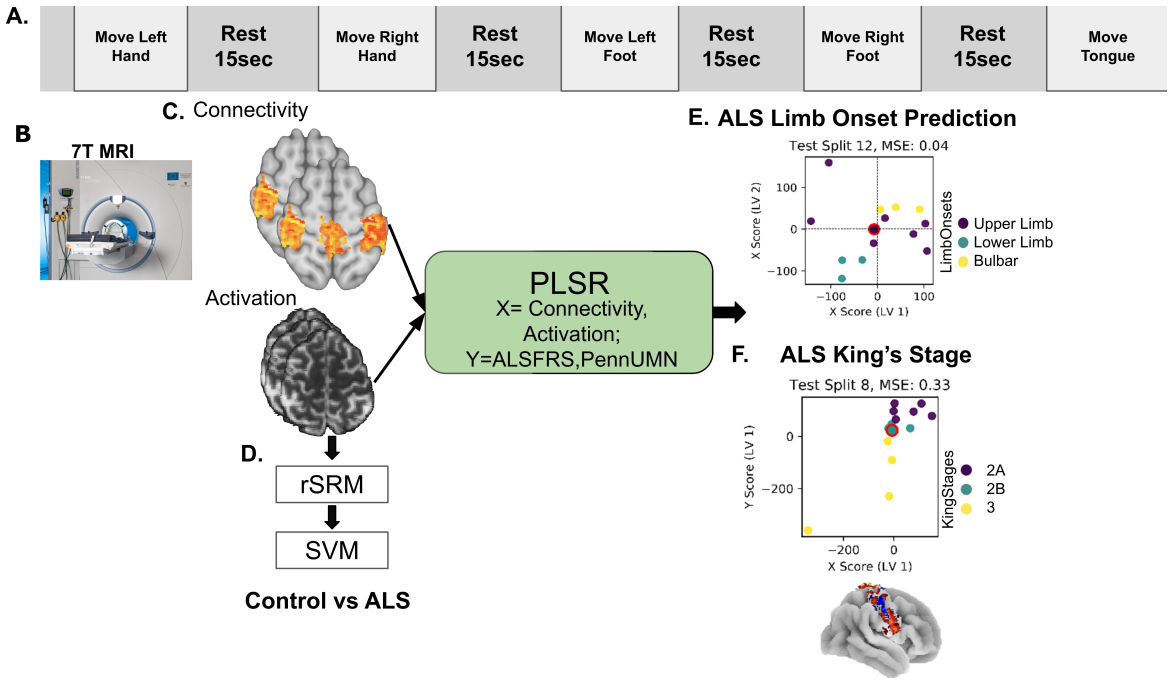

Figure 5.1 **Experimental Design and Analytical Framework:** (A) Motor tasks (12sec) alternated with rest (15sec) across body parts (left/right hand, foot, tongue/lip). (B) 7T MRI setup (C) Functional activation and connectivity maps. (D) rSRM with SVM classified ALS vs. controls. (E) Modeling disease onset site with PLSR-LV clustering (purple: upper limb; blue: lower limb; yellow: bulbar) using activation/connectivity (X) and PUMNS (Y), with LV1/LV2 scatter (MSE = 0.04, for Split 12). (F) Modeling King's stages (Y = ALSFRS) with PLSR showed X-Y latent variable clustering (purple: 2A, blue: 2B, yellow: 3; MSE = 0.33, for split 8). *(Reproduced from Kalyani et al. [46])*

5.2.3 Experiment Design

A block-design paradigm assessed sensorimotor cortex activity, alternating 12-second movement blocks (left/right foot;left/right hand; tongue) with 15-second rest periods (Figure 5.1, panel A). To ensure consistency, participants underwent pre-scan training to familiarize themselves with the movement tasks. During scanning, visual cues (black text on a gray background) were presented to instruct participants when to prepare for and execute each movement (e.g., "prepare left hand," "move left hand"). Each movement was repeated four times, resulting in 20 trials per run. To minimize unintended motion artifacts, fingerless braces were used to stabilize hand movements during scanning.

Additionally, whole-brain susceptibility-weighted imaging (SWI) was performed in a subset of patients (10 out of 14) to assess microstructural alterations. SWI scans were acquired with a voxel resolution of 0.5 mm using transversal slices with a TR of 22 ms, TE of 9 ms, an FOV of 192 mm, a flip angle of 10°, and a bandwidth of 160 Hz/Px. Two patients did not complete the SWI scans due to fatigue and discomfort, as this sequence was acquired at the end of the session. The total scanning time, including all structural and functional acquisitions, was approximately 75 minutes. Structural imaging data from this study have been published separately.

5.3 Methods

5.3.1 Preprocessing

fMRI data preprocessing was conducted using SPM12 (Statistical Parametric Mapping 12). Steps included motion correction, slice-timing correction, and spatial smoothing with a 2 mm FWHM Gaussian kernel [75]. Functional images were co-registered to 7T MP2RAGE anatomical scans using ITK-SNAP (v3.8.0) [112], with manual landmark-based adjustments as needed.

For group analyses, data were normalized to the MNI152 template [28] using the Advanced Normalization Tools (ANTs) framework [5]. The ‘antsRegistrationSyN.sh‘ script applied rigid, affine, and SyN transformations, ensuring precise inter-subject alignment while enabling reliable inter-subject comparisons.

5.3.2 Statistical Analysis

Functional Activation Analysis

Prior to statistical modeling, fMRI time-series data were band-pass filtered (0.01–0.1 Hz) to remove low-frequency drifts and high-frequency noise. A first-level GLM was applied in SPM12 to generate t-statistic maps for each body part engaged in the movement task, including the left and right hands,

left and right feet, and tongue/face regions [71, 70]. These activation maps were subsequently used as predictors to assess disease-related functional changes.

Functional Localizer Mask Generation

Functional localizer masks were generated for group-level comparisons by selecting the top 1500 most significant voxels per body part from the t-maps derived from GLM analysis. This standardized the ROI size across subjects, ensuring that patients with weaker motor performance were not disadvantaged.

To refine the masks:

1. The masks were intersected across all subjects, retaining only voxels consistently activated across participants.
2. A connected component analysis was applied to extract the largest contiguous cluster for each body part.

This ensured that the selected ROIs represented the most functionally relevant sensorimotor regions, focusing on areas closely associated with ALS progression.

Functional Connectivity Analysis

To investigate network-level changes, Eigenvector Centrality Mapping (ECM) was employed to identify regions acting as hubs in the sensorimotor network [59]. ECM assigns higher centrality values to voxels with extensive functional connections to influential regions, allowing the identification of key sensorimotor hubs affected in ALS. ECM maps were computed using Lipsia software [60], based on the task-specific functional localizer masks.

Additionally, seed-based functional connectivity analysis was performed:

1. Seeds were defined as 5-voxel-radius spheres centered on peak activation coordinates.
2. Time-series data were extracted from these seeds and correlated with all other voxels within the combined localizer masks.
3. Connectivity differences were analyzed between ALS patients and controls to detect disease-related alterations.

5.3.3 Classification of ALS Patients and Controls

To isolate functional signatures that differentiate ALS from healthy controls, all 7T fMRI runs were aligned with rSRM [99, 45]. Unlike conventional anatomical alignment, rSRM learns a compact,

low–dimensional feature space that is common across participants, suppressing idiosyncratic noise while retaining group–specific variance—an essential property for detecting the subtle, spatially distributed effects of neurodegeneration.

Two cohort–specific shared spaces were estimated. First, every ALS volume was entered into an *ALS* model, $rSRM_{\mathrm{ALS}}$; an analogous *control* model, $rSRM_{\mathrm{HC}}$, was trained on healthy participants. Within each cohort the data were pre-processed, split by body-part movement condition, and fit in a LOSO loop so that no test data influenced the learned bases. In every fold the held-out subject's time series were independently projected into *both* shared spaces, yielding two matched low-dimensional representations. A linear classifier operating on these paired projections decided whether the unknown brain belonged to the ALS or control distribution, and its performance was averaged across folds. Chance for this binary task is 0.50, mirroring the procedure used for age-group classification in Chapter 4; accuracies significantly above this threshold indicate that rSRM successfully captures disease-specific neural patterns that traditional alignments would have obscured.

5.3.4 Partial-Least-Squares Regression (PLSR)

To link brain measures to clinical status we used PLSR, a multivariate technique that extracts coupled latent components from a predictor matrix $\mathbf{X}$ and a response matrix $\mathbf{Y}$ [63, 51]. For each of the $n = 14$ participants,

$$\mathbf{X} = [\text{task activations} \mid \text{ECM connectivity}], \qquad \mathbf{Y} = [\text{ALSFRS-R} \mid \text{PUMNS}].$$

PLSR factorises the data as

$$\mathbf{X} = \mathbf{T}\mathbf{P}^{\mathsf{T}} + \mathbf{F}_X, \tag{5.1}$$

$$\mathbf{Y} = \mathbf{U}\mathbf{Q}^{\mathsf{T}} + \mathbf{F}_Y, \tag{5.2}$$

with score matrices $\mathbf{T}, \mathbf{U} \in \mathbb{R}^{n \times L}$, loadings $\mathbf{P}, \mathbf{Q}$, and residuals $\mathbf{F}_X, \mathbf{F}_Y$. Under the constraint $\mathbf{U} = \mathbf{T}\mathbf{D}$ (diagonal $\mathbf{D}$), the weights $\mathbf{W}, \mathbf{C}$ are chosen to maximise the cross-covariance of each component pair,

$$\max_{\mathbf{w},\mathbf{c}} \operatorname{cov}\big(\mathbf{X}\mathbf{w}, \mathbf{Y}\mathbf{c}\big).$$

Modelling strategy. Two LOSO-validated models were estimated:

1. **Disease severity. X** contained ECM connectivity and activation within hand, foot and bulbar masks; **Y** was the ALSFRS-R vector.

2. **Site of onset.** The same **X** was related to PUMNS sub-scores that encode upper-/lower-limb and bulbar onset.

For every left-out patient the trained model projected their data into latent-variable (LV) space, yielding clusterable coordinates for King's stage (2A, 2B, 3) and onset type. Prediction error was quantified as mean-squared error across LOSO folds. Finally, weight vectors were back-projected to voxel space; a paired t-test compared the spatial dispersion of activation- versus connectivity-derived weights, testing *H5* ("connectivity is the more sensitive marker").

5.3.5 Longitudinal Percent Signal Change Analysis

As a control analysis, the study examined whether brain response strength diminishes with ALS progression. Percent signal change was calculated for three ALS patients with multiple scans (n=3). The rest condition, averaged over the whole brain across two activity blocks, served as the baseline, with the task block as the parameter. This analysis explored changes in brain responsivity over time.

To address BOLD signal variability, voxel-level time-series were z-scored and band-pass filtered (0.01–0.1 Hz) prior to calculation [3]. These steps standardized data, reduced noise, and isolated task-related activity. However, BOLD remains a relative measure, potentially influenced by physiological and vascular factors (e.g., cerebrovascular reactivity, cerebral blood flow), necessitating cautious interpretation of longitudinal trends (H5).

5.4 Results

5.4.1 Classification of ALS Patients and Controls Based on Sensorimotor Cortex Activation

To determine whether participants could be accurately classified as ALS patients or healthy controls based on functional activation in the sensorimotor cortex, shared response patterns were extracted using rSRM, followed by classification via a SVM. The classification model achieved an overall accuracy of 0.91 ± 0.26, indicating a strong differentiation between the two groups.

Further analysis was conducted to assess whether classification accuracy was predominantly influenced by the functional representation of the initially affected body part or by regions corresponding to non-affected or later-affected areas. A comparison of classification accuracies revealed that regions corresponding to the first-affected body part exhibited significantly lower classification accuracy than regions corresponding to non-first-affected body parts (0.86 ± 0.13 vs. 0.96 ± 0.23, $t(143) = -3.92$, $p = 1.50 \times 10^{-4}$). These findings suggest that, functionally, the disease-defining signature in the sensorimotor cortex extends beyond the first-affected region (Figure 5.2).

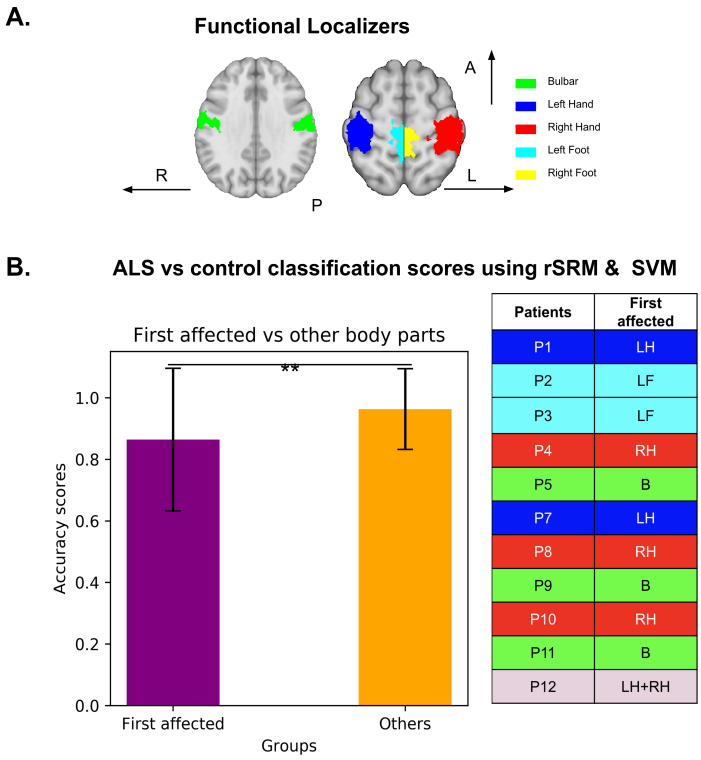

Figure 5.2 **Classification of ALS Patients vs. Controls Using Functional Activation Patterns:** Functional localizer ROIs in sensorimotor Cortex: left hand (LH, blue), right hand (RH, red), left foot (LF, light blue), right foot (RF, yellow), bulbar (B, green). (B) Bar plot of classification accuracy (rSRM + SVM) for first-affected (purple) vs. non-first-affected (orange) body parts, with lower accuracy for first-affected regions ($p < 0.01$). Adjacent table lists each patient's first-affected body part. *(Reproduced from Kalyani et al. [46])*

5.4.2 Latent Variables Identifying Disease Onset and Severity

To determine whether PLSR identifies functional signatures reflecting ALS onset and severity, and whether activation or connectivity is more sensitive (H5), the study modeled functional activation and connectivity profiles using PLSR [51]. These profiles, derived from a combined localizer mask (MI: hand, foot, tongue), were related to ALSFRS-R and PUMNS scores, assessing severity and onset clustering. Absolute mean weights evaluated regional contributions.

Modeling Disease Onset

For functional activation-based modeling, the overall MSE across LOO cross-validation splits was 1.02 ± 0.39 (mean $\pm$ SEM). The scatter plots in Figure 5.3A illustrate the clustering of ALS onset types within the latent variable (LV) space across sample test splits, with purple representing upper limb onset, cyan indicating lower limb onset, and yellow denoting bulbar onset. The first latent

variable (LV1) effectively separated lower limb onset from bulbar onset; however, upper limb onset showed less distinct clustering, often overlapping with other groups. This pattern was mirrored in the region-specific weight distributions: the tongue/face region exhibited the highest average weight ($5.3 \pm 0.1 \times 10^{-5}$), followed by the foot region ($3.8 \pm 0.1 \times 10^{-5}$), while the hand region contributed the lowest weights ($1.9 \pm 0.1 \times 10^{-5}$; Figure 5.3B). The histogram of MSE values across all splits (Figure 5.3C) revealed that the majority clustered below 3, suggesting reasonable model stability, though some splits reached MSEs as high as 6, indicating variability in performance across subjects.

In contrast, functional connectivity-based modeling resulted in an overall MSE of 1.22 ± 0.43. The scatter plots in Figure 5.3D demonstrate improved clustering of onset types compared to activation-based modeling, particularly along LV1 for lower limb versus bulbar onset. Notably, upper limb onset showed clearer separation in several test splits (e.g., splits 4, 5, 10, and 12), leading to more distinct grouping in the LV space. This enhanced clustering was reflected in the weight distributions, with the tongue/face region again showing the highest average weight ($0.86 \pm 0.1 \times 10^{-3}$), followed closely by the foot region ($0.79 \pm 0.1 \times 10^{-3}$), and the hand region contributing less ($0.45 \pm 0.1 \times 10^{-3}$; Figure 5.3E). The MSE histogram (Figure 5.3F) displayed a more consistent spread, with most values concentrated between 1 and 3 and fewer outliers compared to activation, highlighting greater stability in connectivity-based modeling.

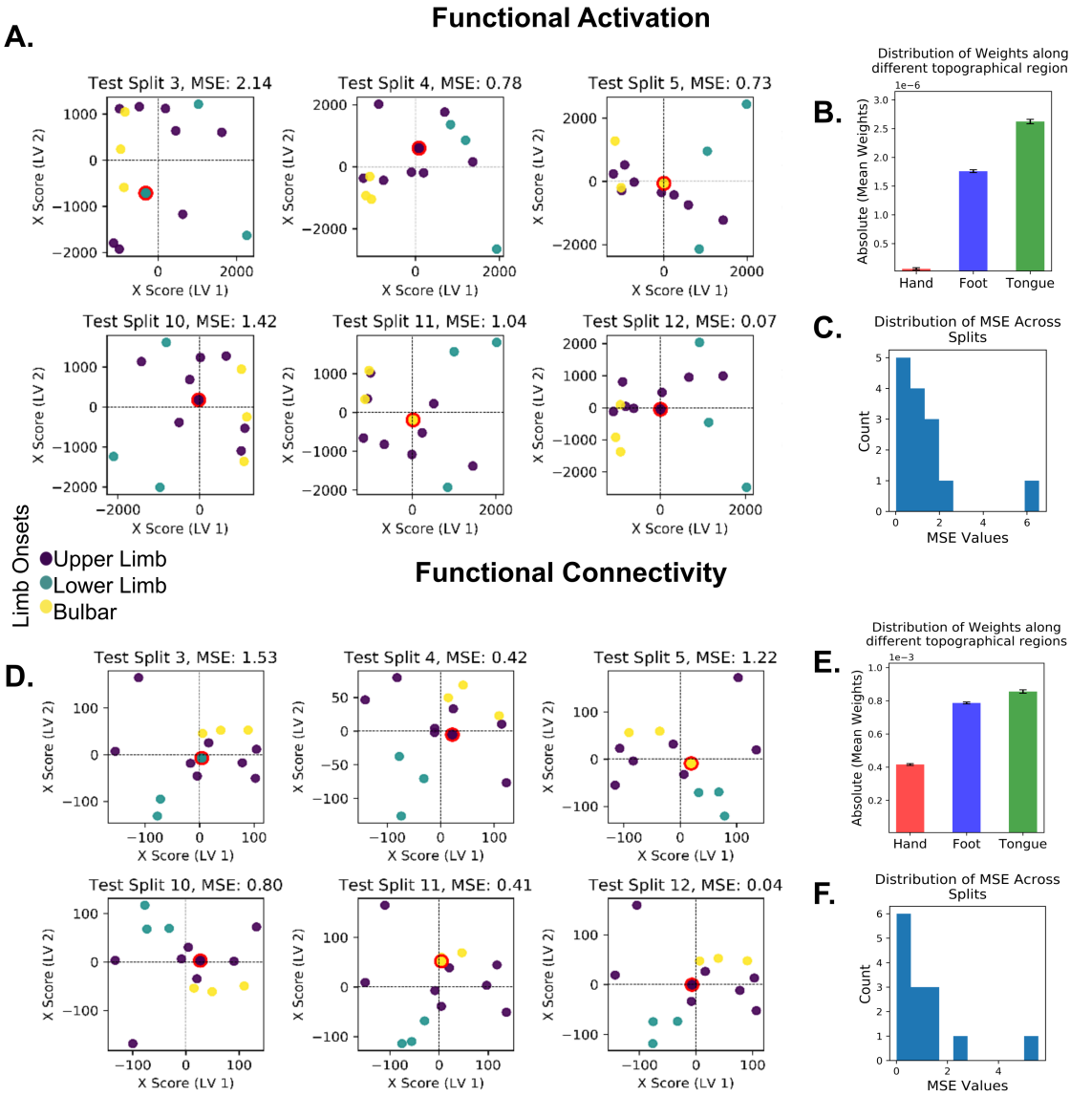

Figure 5.3 **Modeling ALS Onset Site with PLSR.** (A) LV scatter plots of onset types (upper limb: purple, lower limb: cyan, bulbar: yellow) using activation across splits, with MSE. (B) Bar graph of mean weights (hand, foot, tongue), tongue highest. (C) MSE histogram, showing variability. (D) Connectivity-based LV clustering, enhancing separation. (E) Weights, with tongue/foot dominant. (F) MSE histogram, indicating stability. *(Reproduced from [46])*

Modeling Disease Severity

For functional activation-based modeling of disease severity, the overall MSE across all cross-validation splits was 1.22 ± 0.33. However, the projection of participants onto the LV space exhibited fluctuations (Figure 5.4D), indicating instability in the model despite consistent grouping patterns observed across splits. Due to this variability, the study did not pursue further analysis of this model.

Conversely, functional connectivity-based modeling, utilizing ECM features, produced an overall MSE of 1.40 ± 0.30 across splits. This model demonstrated consistent performance in grouping participants by ALS King's stages (2A, 2B, 3). Specifically, the first latent variable (LV1) revealed distinct clusters: participants in King's stage 3 consistently grouped below 0 on the y-axis, while those in stages 2A and 2B clustered above 0 (Figure 5.4C). This grouping pattern held across multiple cross-validation splits, and test subjects' projections aligned with training data clusters (red-outlined points, Figure 5.4C), suggesting reliable generalization.

To explore this effect further, Figure 5.4F illustrates averaged functional connectivity differences between ALS patients and controls across King's stages, revealing an inverted U-shaped profile. In stage 2A, connectivity decreased relative to controls across all seed regions (left hand: -0.13, right hand: -0.11, left foot: -0.04, right foot: -0.07, tongue: -0.07). In stage 2B, connectivity increased (left hand: $+0.08$, right hand: $+0.09$, left foot: $+0.17$, right foot: $+0.16$, tongue: $+0.07$). In stage 3, connectivity dropped again (left hand: -0.16, right hand: -0.19, left foot: -0.23, right foot: -0.21, tongue: -0.18). Longitudinal data from three patients (Figure 5.5) corroborated this trend.

In summary, the study demonstrated that BOLD signal changes in sensorimotor cortex during body part movements successfully classified participants into patients versus controls (H4) and identified LV clustering patterns reflecting disease onset and severity (H5). Functional connectivity outperformed activation in clustering consistency for both onset and severity, with connectivity-based modeling showing tighter MSE distributions and better separation of onset types and stages. Additionally, connectivity changes across King's stages followed an inverted U-shape—reduced in early (2A) and late (3) stages, with a temporary increase in 2B—suggesting compensatory mechanisms in mid-stage ALS, supported by longitudinal data.

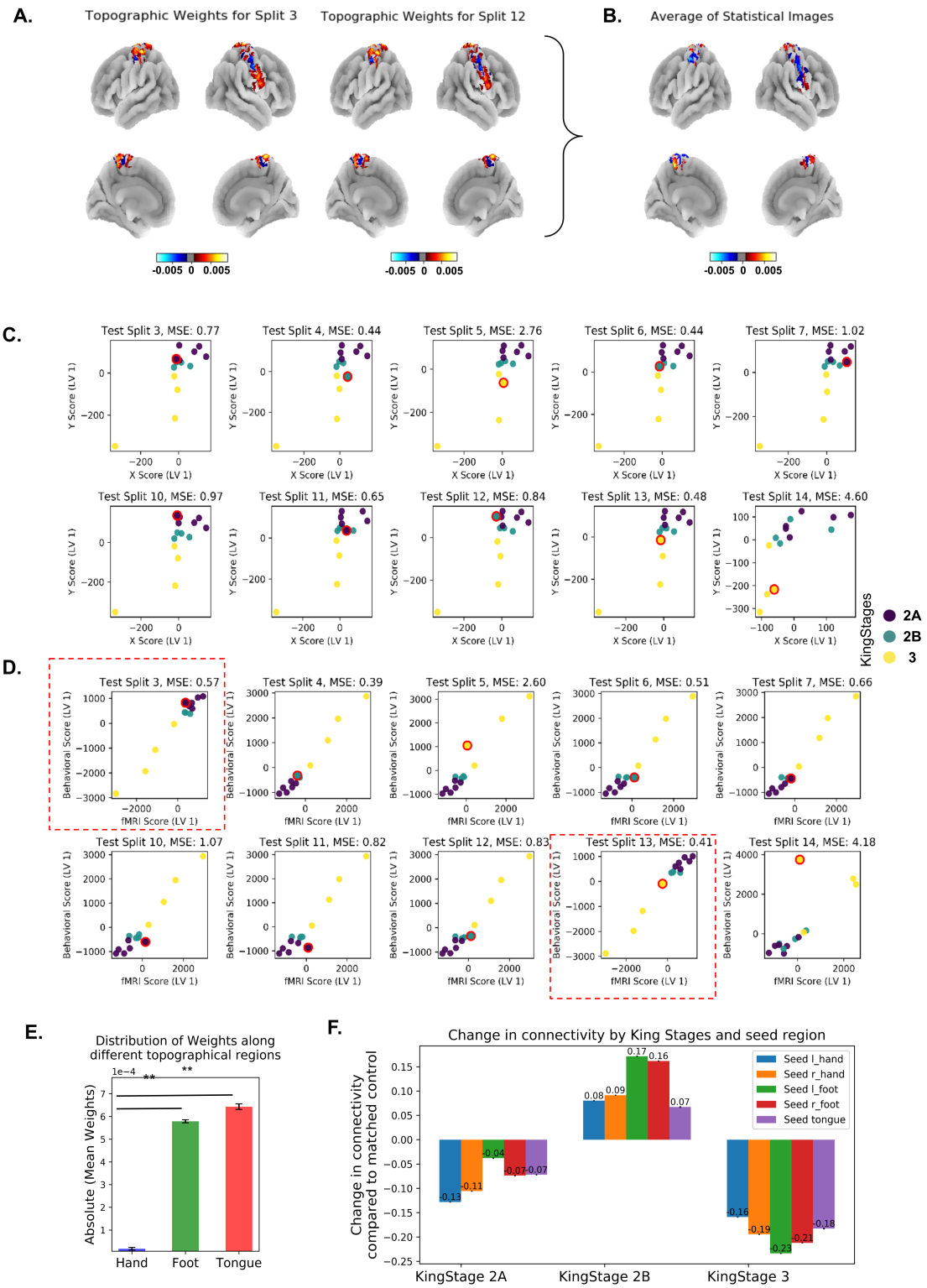

Figure 5.4 **Modeling ALS King's Stages with PLSR:** (A-B) Topographic weight maps (A: splits, B: aggregated), warmer colors for higher weights. (C-D) LV clustering by stages using connectivity (C) and activation (D); red outlines mark test subjects, connectivity MSE lower. (E) Weights (foot, tongue dominant, $p < 0.01$). (F) Connectivity changes (ALS vs. controls), inverted U-shape across stages. *(Adapted from Kalyani et al. [46])*

5.4.3 Topographic vs. Atopographic Functional Profiles in ALS

To investigate whether disease-defining functional information is specific to the first-affected topographic location in the sensorimotor cortex (i.e., topographic, potentially reflecting iron accumulation [70]) or not specific to that location (i.e., atopographic, potentially reflecting calcium accumulation [70]), and to determine whether any topographic region in the MI is strongly associated with the severity of ALS irrespective of onset site, the study conducted additional analyses. Section 5.4.1 reported that classification accuracies for distinguishing patients from controls using rSRM were higher in regions corresponding to behaviorally non-first-affected body parts compared to those of first-affected body parts. This finding already indicates that functionally disease-defining regions in MI are not most prominent in the area behaviorally affected first.

In addition, Section 5.4.2 noted higher weights in the foot and tongue/face regions compared to the hand region when modeling disease onset with PLSR. To further explore whether certain MI regions are more associated with disease severity, the study computed the weight distribution from the connectivity-based King's stage modeling and projected these weights back into voxel space using ECM-derived features [59]. This approach enabled precise identification of the regions driving severity clustering within MI. The results revealed that the highest mean weights were present in the foot ($5.7 \times 10^{-4} \pm 6.828 \times 10^{-6}$) and tongue/face ($6.4 \times 10^{-4} \pm 1.22 \times 10^{-5}$) regions, while the hand region exhibited significantly lower weights ($1.72 \times 10^{-5} \pm 5.78 \times 10^{-6}$; see Figure 5.4E). Paired t-tests between these weight distributions confirmed significant differences: hand versus foot region ($t(13) = -8.90$, $p = 6.84 \times 10^{-7}$), hand versus tongue/face region ($t(13) = -3.69$, $p = 2.72 \times 10^{-3}$), and no significant difference between foot and tongue/face regions ($t(13) = -0.49$, $p = 0.634$; see Figure 5.4E). These findings suggest that higher connectedness (i.e., centrality) in the tongue/face and lower limb regions within the brain's sensorimotor network is more strongly associated with King's stage clustering, whereas the hand region contributes less.

This consistent pattern—higher weights in the foot and tongue/face regions and lower weights in the hand region—was observed in both the modeling of disease onset and disease severity (Section 5.4.2). This indicates that the foot and tongue/face areas demonstrate the greatest functional relevance across ALS progression, irrespective of the initial onset site. Consequently, the disease-defining functional signature appears *atopographic*, not confined to the first-affected topographic location, and the foot and tongue/face regions in MI are particularly linked to severity clustering across patients.

5.4.4 Additional Analysis

Longitudinal Percent Signal Change Analysis

The study tracked neural activity in three ALS patients—P4 (11 months, 3 years post-diagnosis), P1 (5 months), P6 (7 months)—via percent signal change and ECM values. Figures 5.5A, B show activation varied more than connectivity.

For P4, hand/tongue activation peaked at 11 months, then dropped by 3 years; foot declined steadily. ECM stayed stable. For P1, activation rose across regions over 5 months; ECM was steady, tongue slightly down. For P6, hand fell, foot held, tongue rose over 7 months; ECM remained consistent (Table 5.3).

These findings indicate that functional activation undergoes more substantial changes over time than large-scale connectivity measures in ALS patients. This pattern aligns with prior research suggesting early compensatory increases in neural activity followed by a progressive decline as motor neuron degeneration advances. The dissociation between percent signal change and ECM values underscores the importance of examining both localized activation shifts and broader network connectivity when tracking ALS progression longitudinally.

Patients	**T1**	**T2**	**T3**
P4	**ALSFRS-R Total: 37** (bulbar: 12, fine: 6, gross: 7, breathing: 12), KS: **2B**	**ALSFRS-R Total: 36** (bulbar: 12, fine: 6, gross: 7, breathing: 11), KS: **2B**	**ALSFRS-R Total: 41** (bulbar: 11, fine: 10, gross: 9, breathing: 11), KS: **2B**
P1	-	**ALSFRS-R Total: 44** (bulbar: 12, fine: 9, gross: 11, breathing: 12), KS: **2A**	-
P6	**ALSFRS-R Total: 41** (bulbar: 9, fine: 9, gross: 11, breathing: 12), KS: **2B**	**ALSFRS-R Total: 38** (bulbar: 9, fine: 7, gross: 10, breathing: 12), KS: **3**	-

Table 5.2 ALS Functional Rating Scale-Revised (ALSFRS-R) scores over time for three patients. KS: King's Stage. *(Reproduced from Kalyani et al. [46])*

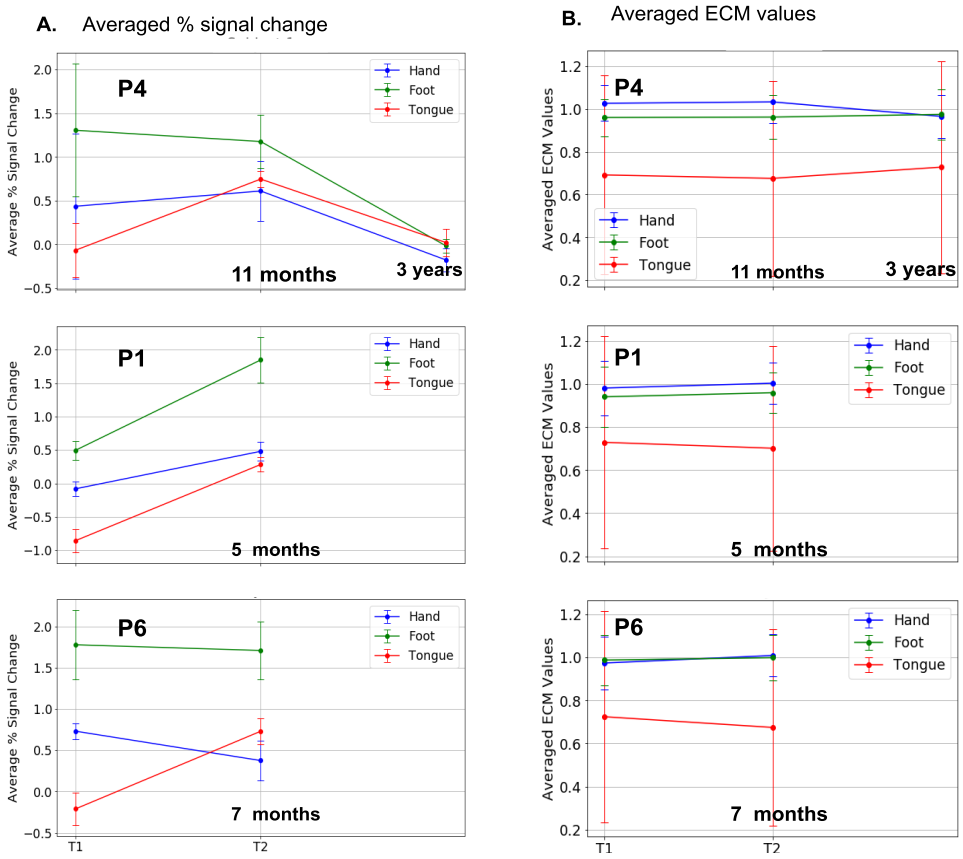

Figure 5.5 **Changes in % signal change and functional connectivity over time:** Line graphs illustrate (A) averaged % signal change and (B) ECM values in brain activity for three subjects across different time points: +11 months and +3 years after the first scan for P4, +5 months after the first scan for P1, +7 months after the first scan for P6. Data is extracted from hand (blue), foot (red), and tongue (green) regions in MI, highlighting the variations in functional activation and connectivity over time. *(Reproduced from Kalyani et al. [46])*

Patient	**Region**	**Time Point**	**Percent Signal Change (mean ± SEM)**	**ECM Values (mean ± SEM)**
P4	Hand	Baseline	0.41 ± 0.83	1.03 ± 0.08
		11 months	0.58 ± 0.34	1.03 ± 0.10
		3 years	0.18 ± 0.13	0.97 ± 0.12
	Foot	Baseline	1.26 ± 0.76	0.96 ± 0.09
		11 months	1.21 ± 0.31	0.96 ± 0.10
		3 years	0.04 ± 0.08	0.96 ± 0.10
	Bulbar	Baseline	0.02 ± 0.31	0.69 ± 0.46
		11 months	0.74 ± 0.09	0.68 ± 0.46
		3 years	0.03 ± 0.16	0.73 ± 0.50
P1	Hand	Baseline	0.15 ± 0.11	0.98 ± 0.13
		5 months	0.38 ± 0.14	1.00 ± 0.09
	Foot	Baseline	0.37 ± 0.14	0.94 ± 0.14
		5 months	1.74 ± 0.34	0.96 ± 0.09
	Bulbar	Baseline	-0.89 ± 0.17	0.73 ± 0.49
		5 months	0.25 ± 0.11	0.70 ± 0.48
P6	Hand	Baseline	0.86 ± 0.10	0.97 ± 0.12
		7 months	0.39 ± 0.24	1.01 ± 0.10
	Foot	Baseline	1.80 ± 0.42	0.99 ± 0.12
		7 months	1.82 ± 0.35	1.00 ± 0.11
	Bulbar	Baseline	0.16 ± 0.20	0.72 ± 0.49
		7 months	0.75 ± 0.16	0.67 ± 0.46

Table 5.3 Percent signal change and connectivity (ECM) changes in ALS patients over time. The table presents longitudinal variations in percent signal change and ECM values across different brain regions (Hand, Foot, Bulbar) for three ALS patients (P4, P1, P6) at various time points. *(Reproduced from Kalyani et al. [46])*

5.5 Discussion

ALS, a rapidly progressing neurodegenerative disease, involves motor control loss and cytoarchitectural changes in MI [2]. While prior studies emphasized structural alterations, this study used 7T-fMRI, rSRM, and PLSR to identify functional signatures in MI linked to ALS onset and progression. Results (1) confirm BOLD signal changes during body part movements distinguish ALS patients from controls (accuracy: 0.91 ± 0.26), (2) show functional connectivity maps better reflect disease severity and onset site than activation maps, and (3) reveal disease-defining information is atopographic, with foot and face areas in MI most tied to severity regardless of onset site. These findings deepen understanding of ALS cortical mechanisms and suggest a novel approach for future clinical studies.

The study distinguished ALS patients from controls using sensorimotor cortex activation and connectivity, supporting prior evidence of distinct motor region patterns in ALS [85, 98, 108]. This separation in latent variable space suggests neuroimaging markers could aid early diagnosis and tailored treatments.

Functional connectivity outperformed activation in modeling onset site and severity, indicating co-activated networks during movement are more sensitive to disease stage than net MI activation. Connectivity decreased in King's stage 2A, increased in 2B, and dropped in 3, aligning with early compensatory increases followed by decline [101, 19]. This inverted U-shape suggests initial network recruitment compensates for early loss, with later declines reflecting severe degeneration. Maintaining early compensation could slow progression, extending prior resting-state [65] and cognitive [20] findings to motor tasks.

Regarding topography, structural studies showed iron accumulation in first-affected MI regions [70], yet functional classification was less accurate there than in non-first-affected areas. This atopographic signature aligns with calcium accumulation in low-myelin MI borders [70, 52], suggesting disease-defining changes span beyond initial sites. Stronger classification in later-affected regions may reflect advanced pathology, emphasizing longitudinal functional tracking over static structural markers. Lack of spinal cord data limits interpretation; future studies combining modalities could clarify this.

Foot and face areas in MI best reflected onset and severity, with higher weights than the hand region, possibly due to greater vulnerability to ALS pathologies [25, 56]. The hand's resilience to age-related iron accumulation [71] or earlier behavioral detection of dysfunction may reduce its functional sensitivity. Bulbar changes, linked to shorter survival [95], further highlight face area relevance. Activating low-myelin borders could be a novel therapeutic target if confirmed in larger cohorts.

5.6 Conclusion

This chapter demonstrated that UHF 7T-fMRI, using rSRM and PLSR, effectively elucidates functional changes in the sensorimotor cortex associated with ALS. The study confirmed that BOLD signal changes during body part movements distinguish ALS patients from controls with high accuracy (H4), supporting the utility of functional neuroimaging as a diagnostic marker. Furthermore, it revealed that latent variables derived from functional connectivity maps outperform activation maps in clustering disease onset site and severity (H5), with an atopographic signature where foot and face areas in MI are most linked to progression, irrespective of initial onset site. These findings highlight the sensitivity of network-level changes to ALS stages, suggesting early compensatory mechanisms that decline with advanced degeneration. By identifying these distinct functional signatures, the study advances understanding of ALS cortical pathology beyond structural alterations and offers a novel framework for tracking progression. Future research should integrate spinal cord and brainstem data, validate these patterns in larger cohorts, and explore therapeutic strategies targeting connectivity preservation, such as enhancing low-myelin border function, to potentially slow disease advancement.

Chapter 6

General Discussion

This thesis leveraged UHF 7T-fMRI with advanced multivariate methods (rSRM, C-SRM, PLSR) to investigate how sensorimotor cortical organization adapts in healthy aging versus how it is disrupted in ALS. Overall, the findings indicate that normal aging is associated with a broadening of functional representations in SI, whereas ALS leads to widespread, non-topographic disruptions in functional networks beyond any single locus. In other words, aging effects appeared as subtle dedifferentiation within the somatosensory maps, while ALS effects were manifest at a network level rather than strictly focal to the initially affected region in the sensorimotor cortex. Below, these outcomes are discussed in light of prior high-resolution fMRI studies and relevant literature.

6.1 Reorganization in Healthy Aging: Fine-Scale Changes and Dedifferentiation

High-resolution 7T-fMRI revealed that older adults maintain overall topographic mapping of the body in SI, but show altered fine-scale organization compared to young adults [45]. The thesis provided the first evidence that the columnar architechture of human SI changes with age. Using rSRM and C-SRM, it was found that the number of functinal columns needed to best capture the the finger specific representation was lower in older adults than in younger adults in BA1, implying that the cortical clumns become larger in aged somatosensory cortex. This finding of age-enlarged columns supports the notion that the aging brain may be compensating for peripheral sensory decline by pooling information over larger areas of cortex. This is consistent with a previous study showing that older adults exhibit broader receptive fields and less precise somatosensory processing [57].

Another key finding was that older adults exhibited a relative *dedifferentiation* of finger representations in SI, as indicated by lower classification accuracy and greater overlap in neural patterns for

different fingers. This suggests that the aging brain may be less able to maintain distinct representations for individual fingers, leading to a more blurred or generalized representation of touch. This is consistent with previous research showing that aging is associated with reduced somatosensory acuity and poorer tactile discrimination [44, 57]. A particular interesting finding was that the age group based classification in the left and right hemisphere was above chance levels which aligns with a prior theory that older brains show less focal activation and more bilateral or diffuse recruitment (e.g. the HAROLD model of reduced hemispheric asymmetry) [10].

Crucially, these high-resolution findings were only detectable with advanced methods that preserve fine detail without blurring across individuals. Traditional group fMRI analyses require spatial smoothing and normalization, which can obscure age differences in sub-millimeter functional architecture. By applying Shared Response Modeling (SRM) to align individuals in a common response space, it was possible to compare detailed topographic features across age groups. Notably, despite dedifferentiation, older adults in our study maintained the hierarchical distinction between Brodmann areas: as in young adults, their BA 3b and BA 1 still showed more precise finger representations than higher-order area 2. Such preservation of overall map structure alongside local broadening suggests that the aging SI undergoes targeted reorganization – potentially an experience-driven adjustment to mitigate declining peripheral or neural precision.

The absence of clear-cut over activation in older cohort, aligns with the structural evidence that the human sensorimotor cortex allows flexibility: the 3D microstructural architecture of the human SI hand area is largely non-topographic at the fine scale [24]. Unlike non-human primates, humans lack firm internal myeloarchitectonic borders for each finger within area 3b, as shown by [24]. All fingers share a similar layer-specific myelin and iron profile, with no structural separations between them. This implies the cortex has reduced structural constraints and a high degree of flexibility for reorganization. In the context of aging, such flexibility could allow cortical circuits to remap or broaden representations in response to neural attrition or sensory decline, helping to preserve function. In sum, healthy aging the functional somatosensory maps “blur” slightly and columns enlarge, reflecting both the loss of specificity and compensatory plasticity within a structurally flexible cortical framework.

6.2 Functional Disruption in ALS: Network-Level Changes & Non-Topographic Pattern

Using 7T-fMRI during motor tasks, ALS patients and controls could be distinguished by widely distributed changes in both activation and connectivity across the motor network [46]. The differences in brain activity related to ALS were not confined to the cortical representation of the initially affected

limb. Instead, disease-related functional alterations appeared "atopographic": the most informative changes occurred in multiple regions of MI that did not strictly correspond to the patient's limb onset. For example, even in patients with hand-onset ALS, the foot and face areas of MI showed the strongest deviations (in terms of model weights obtaine via PLSR) related to disease severity and progression. This suggests that ALS is a network-level disorder, where the pathology extends beyond the initially affected region and involves widespread changes in functional connectivity and activation patterns.

Such a finding is consistent with the known multi-system nature of ALS. Neuroimaging and neuropathological studies have established that ALS involves a multi-system degeneration extending beyond the MI [78]. The finding in this thesis aligns with this view: the disease signature was network-wide, suggesting that once clinical symptoms emerge in one body part, the underlying disease has likely already impacted interconnected regions of the sensorimotor network [46, 78]. Supporting this, an ultra-high-field MRI study mapping microstructural changes in early ALS found layer-specific abnormalities throughout MI, rather than a single focal lesion [70]. In that study, Northall et al. (2024) reported increased iron in deeper layers of MI specifically in the cortical field corresponding to patients' limb onset, but also found widespread calcium accumulation in the low-myelin borders between MI subregions, a pattern not respecting the topographic boundaries of hand, foot, or face areas. This layer-specific pathology supports a model of ALS spread that is non-topographic – pathological processes (e.g. calcium-mediated degeneration) appear to propagate along cortical pathways that link multiple body representations. The functional data used in this thesis mirror this: the regions between body part representations seem to carry significant disease-related signals, implying that ALS perturbs the integrated network of motor areas rather than simply eroding one homuncular segment at a time.

Many ALS resting-state show decreased connectivity within the sensorimotor network and frontotemporal networks, alongside increased connectivity in regions like the cerebellum and default-mode network (possibly reflecting compensatory recruitment) [78, 92]. Through the analysis of task-based fMRI, we provide additional evidence that motor network activity in ALS exhibits atypical patterns. Interestingly, we observed an inverted-U pattern of connectivity changes with disease progression: patients in early stage (King's stage 2A) showed lower connectivity than controls, those in mid-stage (2B) showed a paradoxical increase (suggesting transient hyper-connectivity or compensation), and in late stage (3) connectivity dropped again sharply. This trajectory is consistent with the idea of an early compensatory upregulation of network connectivity – the brain initially recruits additional circuits to maintain function as motor neurons are lost, leading to heightened connectivity – followed by a collapse of connectivity as neurodegeneration overwhelms these compensatory mechanisms. Such a compensatory early increase has been hinted at by prior studies: for example, Douaud et al. (2011) found increased functional connectivity in premotor and thalamic networks in ALS, interpreted as compensatory or disinhibition effects [26].

Our results extend those resting-state findings to a task context (*an area that has been relatively underdeveloped compared to resting-state studies*), implying that during actual movement attempts, ALS patients initially engage a broader network (perhaps to compensate for weak output), but as the disease progresses, even this broader network can no longer be enlisted, resulting in connectivity decline. Clinically, this suggests that maintaining network connectivity in early ALS might prolong function, whereas loss of network integrity is a harbinger of advanced disease. It also aligns with EEG/MEG studies showing early changes in oscillatory network activity in ALS [94, 79].

Most existing ALS neuroimaging studies have focused on resting-state fMRI connectivity, owing in part to the practical challenges of scanning patients during tasks. Resting-state acquisitions are short, require no active participation, and can be more easily pooled across sites. Indeed, a large body of ALS literature has mapped intrinsic connectivity alterations – for example, decreased sensorimotor network coherence and increased default-mode connectivity, as reviewed earlier [78]. However, resting-state data alone cannot reveal how functional networks perform during active movement or cognitive engagement. Task-based fMRI provides complementary insight by directly probing the brain's ability to execute functions that are failing behaviorally. Our 7T task paradigm (involving attempted movements of affected and unaffected body parts) proved feasible even for patients and yielded robust markers of dysfunction. We acknowledge that task-based fMRI in ALS is challenging – patients' motor disabilities and fatigue can limit task performance, and severe cases may be unable to perform tasks at all [103]. These limitations have understandably made resting-state approaches attractive. Nevertheless, our findings demonstrate that carefully designed tasks (e.g. simple finger or ankle movements) at high field can successfully capture meaningful network changes. This therefore calls for more task-based neuroimaging studies in ALS to complement resting-state results.

6.3 Comparative Insights: Aging vs. ALS

To effectively compare the findings from healthy aging and ALS, it is important to note that the two conditions are not directly comparable. Aging is a gradual process that affects all individuals, while ALS is a specific neurodegenerative disease with a distinct pathology. However, both conditions share some commonalities in terms of their effects on the sensorimotor cortex. In both cases, the sensorimotor cortex exhibits changes in functional organization, but the nature and extent of these changes differ.

While healthy aging might involve a gradual blurring of functional boundaries, ALS seems to induce a more significant breakdown of network integrity, often accompanied by compensatory mechanisms [9]. Studies have reported both increased and decreased functional connectivity in the sensorimotor network in ALS [115], suggesting a complex pattern of network disruption rather

than simple dedifferentiation. Notably, research [70] has highlighted layer-specific pathology in the motor cortex in ALS, particularly affecting layers V and VI, which may be a key differentiator from the microstructural changes seen in healthy aging. Furthermore, the phenomenon of cortical hyperexcitability is a well-documented feature of ALS [17], which is not typically observed in healthy aging to the same extent. This suggests that the nature of sensorimotor cortex reorganization in ALS involves a combination of neurodegenerative processes, compensatory responses, and altered neuronal excitability that distinguishes it from the more subtle changes associated with typical aging.

The findings from this thesis suggest that aging and ALS may represent two ends of a spectrum of functional organization in the sensorimotor cortex. Aging appears to involve a gradual dedifferentiation and broadening of representations, while ALS leads to more abrupt and widespread disruptions in network connectivity. This highlights the importance of considering both localized and network-level changes when studying brain function in aging and neurodegenerative diseases.

6.4 Advanced Multivariate Methods and High-Field Imaging: Benefits and Insights

A unifying theme in our approach was the use of multivariate analytical methods (rSRM, C-SRM, PLSR) to capitalize on the richness of 7T-fMRI data. Standard univariate analysis often averages signals over regions or subjects, potentially blurring individual differences or fine-grained effects. In contrast, rSRM allowed us to align functional data across individuals without spatial smoothing, preserving sub-millimeter information [99]. By projecting each subject's 7T responses into a common low-dimensional space, rSRM made it feasible to perform group comparisons of fine topographies in the aging and ALS study. The success of this method was evident in our ability to detect subtle age differences in columnar organization. Furthermore, we introduced a column-specific extension (C-SRM) to quantify how many distinct columns were present, revealing age effects on cortical columns. This demonstrates that multivariate decomposition techniques can greatly enhance group-level analyses in ultra-high-resolution fMRI, where one cannot simply blur or average data as is done at 3T.

In the ALS study, we employed PLSR to identify the most informative regions for distinguishing patients from controls. The decision to employ PLSR for modeling and clustering, rather than prediction, in our ALS study was a deliberate one, grounded in the complex nature of this neurodegenerative condition. ALS is characterized by significant phenotypic heterogeneity, with variations in disease onset, progression rate, and the specific motor symptoms that manifest [111]. Given this variability, constructing a predictive model that accurately forecasts disease outcomes across all individuals with ALS presents a substantial challenge, often requiring very large and carefully stratified datasets.

Instead, our primary objective was to leverage the strengths of PLSR in identifying latent variables and grouping individuals based on shared patterns of functional connectivity or activation within the sensorimotor network [46]. PLSR is particularly well-suited for analyzing high-dimensional neuroimaging data, such as fMRI, by reducing its complexity and revealing underlying relationships between brain activity and experimental variables or subject characteristics [14]. This approach allowed us to explore the intrinsic organization of the sensorimotor network in ALS and identify distinct subgroups of patients exhibiting similar patterns of functional alteration.

The use of PLSR in our ALS study also aligns with the growing recognition of the need for individualized approaches in neurodegenerative disease research. By focusing on the shared patterns of functional connectivity and activation, we aimed to uncover the unique disease signatures that characterize ALS, which may ultimately inform personalized treatment strategies and improve patient outcomes. This approach is particularly relevant in the context of ALS, where understanding the heterogeneity of disease presentation and progression is crucial for developing targeted interventions.

The combination of high-resolution imaging and advanced multivariate methods allowed us to capture the intricate details of sensorimotor cortical organization in both healthy aging and ALS. By leveraging the strengths of 7T-fMRI and sophisticated analytical techniques, we were able to uncover subtle changes in functional organization that would have been difficult to detect using traditional methods. This highlights the potential of high-field imaging and multivariate approaches to advance our understanding of brain function in both normal aging and neurodegenerative diseases.

6.5 Challenges and Limitations

We acknowledge several limitations in our study. The relatively small sample size, particularly of ALS patients, limits the generalizability of our findings (though they are supported by exiting literature). Recruiting patients in the early stages of ALS is especially challenging, so our cohort was small and may not represent the full spectrum of the disease. Small sample sizes can undermine statistical power and the replicability of results in fMRI research. These factors constrain the conclusions we can draw from our data.

Moreover, the demands of task-based fMRI imposed additional constraints. Advanced ALS patients often have difficulty performing precise or prolonged movements, which can compromise data quality. During scanning, factors such as muscle fatigue or slowness may have introduced variability. We chose overt finger-movement tasks to directly probe sensorimotor function, but this approach has trade-offs: motor impairments could confound task performance, and strict performance requirements may bias the sample toward higher-functioning participants.

Methodologically, our reliance on overt movement tasks represents a trade-off. While overt tasks provide clear behavioral paradigms, they require patient compliance and exclude those unable to move. By contrast, resting-state fMRI or motor imagery paradigms reduce movement demands but introduce interpretive challenges, as spontaneous or imagined activity may engage different neural circuits. Future work should consider comparing these approaches to better accommodate patient limitations while capturing relevant neural dynamics.

Another limitation is our narrow anatomical focus. We limited analysis to primary sensorimotor regions to target the motor cortex and somatosensory cortex specifically. However, age-related and ALS-related changes likely involve broader neural networks, including premotor, parietal, or subcortical regions. By focusing on the sensorimotor cortex alone, we may have overlooked important changes elsewhere. Future studies might use whole-brain analyses or include additional cortical areas to provide a more complete view of functional reorganization. We also recognize technical and analytical constraints. We used advanced multivariate alignment methods (such as SRM and C-SRM) to improve cross-subject alignment, but these complex models complicate interpretation; it is not always clear how the transformations affect the observed patterns.

Moreover, the fMRI BOLD signal is an indirect proxy for neural activity. Because BOLD depends on hemodynamic changes, it has limited temporal precision (on the order of seconds) and can be influenced by vascular factors. These constraints mean we cannot directly infer fast neural dynamics from our data. To address these limitations, future work should integrate complementary approaches and collaborations. Multimodal imaging — for example, combining fMRI with EEG or MEG for higher temporal resolution, or with diffusion MRI for structural connectivity — could compensate for the weaknesses of any single modality. Larger, multicenter studies would also be beneficial: pooling data across sites can increase sample size, improve statistical power, and capture a more diverse patient population. Such collaborative efforts would enable longitudinal tracking of ALS progression and strengthen the validity of any biomarkers identified.

6.6 Implications for Future Research and Clinical Applications

To better understand the distinct and shared mechanisms underlying changes in the sensorimotor cortex, future research should include studies directly comparing the longitudinal progression of functional changes in healthy aging and ALS within the same individuals (if feasible) or using carefully matched cohorts. Additionally, multimodal investigations combining fMRI, Diffusion Tensor Imaging (DTI), and MEG/EEG could identify unique and overlapping microstructural and electrophysiological correlates of the observed functional changes in both aging and ALS. Table 6.1

outlines concrete projects that flow from this work, from longitudinal column tracking in ageing to multimodal biomarkers in ALS.

Research Question/Area	**Suggested fMRI Technique(s)**	**Potential Multivariate Methods**	**Significance/ Rationale**
Functional impairments in sensory-motor and cognitive domains	Task-based paradigms	MVPA, PLSR	Identify functional deficits and precision loss to guide targeted interventions.
Changes in cortical columnar organization	Ultra-high-field (7T) task-based fMRI	SRM, Column-based decoding	Detect early biomarkers or adaptive mechanisms through column-level disruptions.
Longitudinal tracking of cortical network changes	Resting-state, Task-based fMRI	Dynamic functional connectivity, PLSR, ICA	Track connectivity changes for early biomarkers of ALS progression and aging decline.
Integration of structural and functional cortical changes	Multimodal (fMRI + Structural MRI/DTI)	Joint ICA, Parallel ICA	Link structural and functional changes to understand neurodegeneration and aging.
Identification of neuroimaging-based subgroups and clinical phenotypes	Task-based, Resting-state fMRI	Clustering algorithms, PLSR	Personalize diagnostics and treatment strategies.
Neuroimaging-guided therapeutic interventions	Task-based fMRI	SRM, PLSR	To evaluate and develop interventions, such as targeted cognitive training or neurofeedback, aimed at refining cortical representations and compensatory mechanisms impaired by ALS or aging.

Table 6.1 Potential Future Research Directions for fMRI in ALS & Aging

6.7 Conclusion

Synthesizing the two lines of investigation, we see that aging and ALS each provoke distinct changes in the sensorimotor cortex—yet in both cases, the disruptions are best understood by looking beyond localized activity. In aging, the *overall* topographic framework endures while granularity declines, consistent with compensatory broadening of cortical representation. In ALS, functional connectivity dissolves in a non-topographic pattern, often preceding overt clinical symptoms in certain regions. These findings suggest that neuroimaging should increasingly emphasize network-level metrics and columnar precision when studying age-related or disease-related brain changes. In turn, the robust alignment and dimensionality-reduction techniques showcased here provide a roadmap for future studies aiming to detect nuanced shifts in brain organization at ultra-high spatial resolution. Such research is essential to moving from purely observational science to targeted strategies for intervention—be it rehabilitative therapies for older adults or novel diagnostic and tracking tools in ALS. In short, leveraging multivariate, high-resolution neuroimaging offers a powerful window into the functional architecture of the human sensorimotor cortex under both normal and pathological conditions, illuminating pathways toward improved clinical outcomes and deeper theoretical insights.

References

[1] Agosta, F., Valsasina, P., Absinta, M., Riva, N., Sala, S., Prelle, A., Copetti, M., Comola, M., Comi, G., and Filippi, M. (2011). Sensorimotor functional connectivity changes in amyotrophic lateral sclerosis. *Cerebral cortex*, 21(10):2291–2298.

[2] Al-Chalabi, A., Hardiman, O., Kiernan, M. C., Chiò, A., Rix-Brooks, B., and van den Berg, L. H. (2016). Amyotrophic lateral sclerosis: moving towards a new classification system. *The Lancet Neurology*, 15(11):1182–1194.

[3] Aquino, K. M., Fulcher, B., Oldham, S., Parkes, L., Gollo, L., Deco, G., and Fornito, A. (2022). On the intersection between data quality and dynamical modelling of large-scale fmri signals. *NeuroImage*, 256:119051.

[4] Ashburner, J., Barnes, G., Chen, C., Daunizeau, J., Flandin, G., Friston, K., Gitelman, D., Kiebel, S., Kilner, J., Litvak, V., et al. (2012). Spm8 manual. *Functional Imaging Laboratory, Institute of Neurology*.

[5] Avants, B. B., Tustison, N., Song, G., et al. (2009). Advanced normalization tools (ants). *Insight j*, 2(365):1–35.

[6] Barry, R. L., Babu, S., Anteraper, S. A., Triantafyllou, C., Keil, B., Rowe, O. E., Rangaprakash, D., Paganoni, S., Lawson, R., Dheel, C., et al. (2021). Ultra-high field (7t) functional magnetic resonance imaging in amyotrophic lateral sclerosis: a pilot study. *NeuroImage: Clinical*, 30:102648.

[7] Bowman, C. R., Chamberlain, J. D., and Dennis, N. A. (2019). Sensory representations supporting memory specificity: Age effects on behavioral and neural discriminability. *Journal of Neuroscience*, 39(12):2265–2275.

[8] Brodoehl, S., Klingner, C., Stieglitz, K., and Witte, O. W. (2013). Age-related changes in the somatosensory processing of tactile stimulation—an fmri study. *Behavioural brain research*, 238:259–264.

[9] Brooks, B. R., Bushara, K., Khan, A., Hershberger, J., Wheat, J. O., Belden, D., and Henningsen, H. (2000). Functional magnetic resonance imaging (fmri) clinical studies in als–paradigms, problems and promises. *Amyotrophic Lateral Sclerosis and Other Motor Neuron Disorders: Official Publication of the World Federation of Neurology, Research Group on Motor Neuron Diseases*, 1:S23–32.

[10] Cabeza, R. (2002). Hemispheric asymmetry reduction in older adults: the harold model. *Psychology and aging*, 17(1):85.

[11] Cedarbaum, J. M., Stambler, N., Malta, E., Fuller, C., Hilt, D., Thurmond, B., Nakanishi, A., Group, B. A. S., complete listing of the BDNF Study Group, A., et al. (1999). The alsfrs-r: a revised als functional rating scale that incorporates assessments of respiratory function. *Journal of the neurological sciences*, 169(1-2):13–21.

[12] Chadwick, M. J., Bonnici, H. M., and Maguire, E. A. (2012). Decoding information in the human hippocampus: a user's guide. *Neuropsychologia*, 50(13):3107–3121.

[13] Chaimow, D., Uğurbil, K., and Shmuel, A. (2018). Optimization of functional mri for detection, decoding and high-resolution imaging of the response patterns of cortical columns. *NeuroImage*, 164:67–99.

[14] Chen, C., Cao, X., and Tian, L. (2019). Partial least squares regression performs well in mri-based individualized estimations. *Frontiers in neuroscience*, 13:1282.

[15] Chen, P.-H. C., Chen, J., Yeshurun, Y., Hasson, U., Haxby, J., and Ramadge, P. J. (2015). A reduced-dimension fmri shared response model. *Advances in neural information processing systems*, 28.

[16] Chenji, S., Jha, S., Lee, D., Brown, M., Seres, P., Mah, D., and Kalra, S. (2016). Investigating default mode and sensorimotor network connectivity in amyotrophic lateral sclerosis. *PloS one*, 11(6):e0157443.

[17] Chmiel, J. and Stępień-Słodkowska, M. (2025). Resting-state eeg oscillations in amyotrophic lateral sclerosis (als): Toward mechanistic insights and clinical markers. *Journal of Clinical Medicine*, 14(2):545.

[18] Cosottini, M., Donatelli, G., Costagli, M., Ienco, E. C., Frosini, D., Pesaresi, I., Biagi, L., Siciliano, G., and Tosetti, M. (2016). High-resolution 7t mr imaging of the motor cortex in amyotrophic lateral sclerosis. *American journal of neuroradiology*, 37(3):455–461.

[19] Dash, D., Teplansky, K., Ferrari, P., Babajani-Feremi, A., Calley, C. S., Heitzman, D., Austin, S. G., and Wang, J. (2024). Automatic detection of als from single-trial meg signals during speech tasks: a pilot study. *Frontiers in Psychology*, 15:1114811.

[20] De Marchi, F., Carrarini, C., De Martino, A., Diamanti, L., Fasano, A., Lupica, A., Russo, M., Salemme, S., Spinelli, E. G., and Bombaci, A. (2021). Cognitive dysfunction in amyotrophic lateral sclerosis: can we predict it? *Neurological Sciences*, 42(6):2211–2222.

[21] De Martino, F., Moerel, M., Xu, J., et al. (2018). High-resolution functional mri at 7t: Challenges and solutions. *NeuroImage*, 168:330–341.

[22] de Moraes, F. H. P., Sudo, F., Carneiro Monteiro, M., de Melo, B. R., Mattos, P., Mota, B., and Tovar-Moll, F. (2024). Cortical folding correlates to aging and alzheimer's disease's cognitive and csf biomarkers. *Scientific Reports*, 14(1):3222.

[23] Diedrichsen, J., Wiestler, T., and Krakauer, J. W. (2013). Two distinct ipsilateral cortical representations for individuated finger movements. *Cerebral Cortex*, 23(6):1362–1377.

[24] Doehler, J., Northall, A., Liu, P., Fracasso, A., Chrysidou, A., Speck, O., Lohmann, G., Wolbers, T., and Kuehn, E. (2023). The 3d structural architecture of the human hand area is nontopographic. *Journal of Neuroscience*, 43(19):3456–3476.

[25] Donatelli, G., Costagli, M., Cecchi, P., Migaleddu, G., Bianchi, F., Frumento, P., Siciliano, G., and Cosottini, M. (2022). Motor cortical patterns of upper motor neuron pathology in amyotrophic lateral sclerosis: A 3 t mri study with iron-sensitive sequences. *NeuroImage: Clinical*, 35:103138.

[26] Douaud, G., Filippini, N., Knight, S., Talbot, K., and Turner, M. R. (2011). Integration of structural and functional magnetic resonance imaging in amyotrophic lateral sclerosis. *Brain*, 134(12):3470–3479.

[27] Eisen, A. (2021). The dying forward hypothesis of als: tracing its history. *Brain sciences*, 11(3):300.

[28] Evans, A. C., Janke, A. L., Collins, D. L., and Baillet, S. (2012). Brain templates and atlases. *Neuroimage*, 62(2):911–922.

[29] Filippi, M., Basaia, S., Canu, E., Imperiale, F., Magnani, G., Falautano, M., Comi, G., Falini, A., and Agosta, F. (2020). Changes in functional and structural brain connectome along the alzheimer's disease continuum. *Molecular psychiatry*, 25(1):230–239.

[30] Fischl, B. (2012). Freesurfer. *Neuroimage*, 62(2):774–781.

[31] Fjell, A. M., Walhovd, K. B., Westlye, L. T., Østby, Y., Tamnes, C. K., Jernigan, T. L., Gamst, A., and Dale, A. M. (2010). When does brain aging accelerate? dangers of quadratic fits in cross-sectional studies. *Neuroimage*, 50(4):1376–1383.

[32] Gardner, E. P., Martin, J. H., et al. (2000). Coding of sensory information. *Principles of neural science*, 4:411–429.

[33] Glasser, M. F., Coalson, T. S., Robinson, E. C., Hacker, C. D., Harwell, J., Yacoub, E., Ugurbil, K., Andersson, J., Beckmann, C. F., Jenkinson, M., et al. (2016). A multi-modal parcellation of human cerebral cortex. *Nature*, 536(7615):171–178.

[34] Guntupalli, J. S., Feilong, M., and Haxby, J. V. (2018). A computational model of shared fine-scale structure in the human connectome. *PLoS computational biology*, 14(4):e1006120.

[35] Haxby, J. V. (2012). Multivariate pattern analysis of fmri: the early beginnings. *Neuroimage*, 62(2):852–855.

[36] Haxby, J. V., Guntupalli, J. S., Halchenko, Y. O., Conroy, B. R., Gobbini, M. I., Hanke, M., and Ramadge, P. J. (2014). Decoding neural representational spaces using multivariate pattern analysis. *Annual Review of Neuroscience*, 37:435–456.

[37] Haxby, J. V., Guntupalli, J. S., Nastase, S. A., and Feilong, M. (2020). Hyperalignment: Modeling shared information encoded in idiosyncratic cortical topographies. *elife*, 9:e56601.

[38] He, J. L., Fuelscher, I., Coxon, J., Chowdhury, N., Teo, W.-P., Barhoun, P., Enticott, P., and Hyde, C. (2019). Individual differences in intracortical inhibition predict motor-inhibitory performance. *Experimental brain research*, 237:2715–2727.

[39] Huber, L., Finn, E. S., Handwerker, D. A., Bönstrup, M., Glen, D. R., Kashyap, S., Ivanov, D., Petridou, N., Marrett, S., Goense, J., et al. (2020). Sub-millimeter fmri reveals multiple topographical digit representations that form action maps in human motor cortex. *Neuroimage*, 208:116463.

[40] Huber, L. R., Poser, B. A., Bandettini, P. A., Arora, K., Wagstyl, K., Cho, S., Goense, J., Nothnagel, N., Morgan, A. T., van den Hurk, J., et al. (2021). Laynii: A software suite for layer-fmri. *NeuroImage*, 237:118091.

[41] In, M.-H., Posnansky, O., and Speck, O. (2016). Psf mapping-based correction of eddy-current-induced distortions in diffusion-weighted echo-planar imaging. *Magnetic resonance in medicine*, 75(5):2055–2063.

[42] Janko, D., Thoenes, K., Park, D., Willoughby, W., Horton, M., and Bolding, M. (2022). Somatotopic mapping of the fingers in the somatosensory cortex using functional magnetic resonance imaging: A review of literature. *Frontiers in Neuroanatomy*, 16:866848.

[43] Kaas, J. H. (2004). Somatosensory system. *The human nervous system*, pages 1059–1092.

[44] Kalisch, T., Ragert, P., Schwenkreis, P., Dinse, H. R., and Tegenthoff, M. (2009). Impaired tactile acuity in old age is accompanied by enlarged hand representations in somatosensory cortex. *Cerebral Cortex*, 19(7):1530–1538.

[45] Kalyani, A., Contier, O., Klemm, L., Azañon, E., Schreiber, S., Speck, O., Reichert, C., and Kuehn, E. (2023). Reduced dimension stimulus decoding and column-based modeling reveal architectural differences of primary somatosensory finger maps between younger and older adults. *NeuroImage*, 283:120430.

[46] Kalyani, A., Northall, A., Schreiber, S., Brüggemann, J., Vielhaber, S., Al Dubai, M., Benramadan, A., Mattern, H., Speck, O., Reichert, C., et al. (2025). Individualized phenotyping of functional als pathology in sensorimotor cortex. *bioRxiv*, pages 2025–01.

[47] Kandel, E. R., Schwartz, J. H., Jessell, T. M., Siegelbaum, S., Hudspeth, A. J., Mack, S., et al. (2000). *Principles of neural science*, volume 4. McGraw-hill New York.

[48] Kassraian, P., Rabe, F., Enz, N., Maathuis, M., and Wenderoth, N. (2022). Prior information improves tactile representation in primary somatosensory cortex. *bioRxiv*, pages 2022–10.

[49] Kolasinski, J., Makin, T. R., Jbabdi, S., Clare, S., Stagg, C. J., and Johansen-Berg, H. (2016). Investigating the stability of fine-grain digit somatotopy in individual human participants. *Journal of Neuroscience*, 36(4):1113–1127.

[50] Kreitz, S., Mennecke, A., Konerth, L., Rösch, J., Nagel, A. M., Laun, F. B., Uder, M., Dörfler, A., and Hess, A. (2023). 3t vs. 7t fmri: capturing early human memory consolidation after motor task utilizing the observed higher functional specificity of 7t. *Frontiers in Neuroscience*, 17:1215400.

[51] Krishnan, A., Williams, L. J., McIntosh, A. R., and Abdi, H. (2011). Partial least squares (pls) methods for neuroimaging: A tutorial and review. *NeuroImage*, 56(2):455–475.

[52] Kuehn, E., Dinse, J., Jakobsen, E., Long, X., Schäfer, A., Bazin, P.-L., Villringer, A., Sereno, M. I., and Margulies, D. S. (2017). Body topography parcellates human sensory and motor cortex. *Cerebral Cortex*, 27(7):3790–3805.

[53] Kuehn, E., Haggard, P., Villringer, A., Pleger, B., and Sereno, M. I. (2018). Visually-driven maps in area 3b. *Journal of Neuroscience*, 38(5):1295–1310.

[54] Kuehn, E. and Pleger, B. (2020a). Encoding schemes in somatosensation: from micro-to meta-topography. *NeuroImage*, 223:117255.

[55] Kuehn, E. and Pleger, B. (2020b). Will 7t fMRI benefit clinical neuroscience? *Frontiers in Human Neuroscience*, 14:234.

[56] Kwan, J. Y., Jeong, S. Y., Van Gelderen, P., Deng, H.-X., Quezado, M. M., Danielian, L. E., Butman, J. A., Chen, L., Bayat, E., Russell, J., et al. (2012). Iron accumulation in deep cortical layers accounts for mri signal abnormalities in als: correlating 7 tesla mri and pathology. *PloS one*, 7(4):e35241.

[57] Liu, P., Chrysidou, A., Doehler, J., Hebart, M. N., Wolbers, T., and Kuehn, E. (2021). The organizational principles of de-differentiated topographic maps in somatosensory cortex. *Elife*, 10:e60090.

[58] Lockhart, S. N. and DeCarli, C. (2014). Structural imaging measures of brain aging. *Neuropsychology review*, 24:271–289.

[59] Lohmann, G., Margulies, D. S., Horstmann, A., Pleger, B., Lepsien, J., Goldhahn, D., Schloegl, H., Stumvoll, M., Villringer, A., and Turner, R. (2010). Eigenvector centrality mapping for analyzing connectivity patterns in fmri data of the human brain. *PloS one*, 5(4):e10232.

[60] Lohmann, G., Müller, K., Bosch, V., Mentzel, H., Hessler, S., Chen, L., Zysset, S., and von Cramon, D. Y. (2001). Lipsia—a new software system for the evaluation of functional magnetic resonance images of the human brain. *Computerized medical imaging and graphics*, 25(6):449–457.

[61] Luo, C., Chen, Q., Huang, R., Chen, X., Chen, K., Huang, X., Tang, H., Gong, Q., and Shang, H.-F. (2012). Patterns of spontaneous brain activity in amyotrophic lateral sclerosis: a resting-state fmri study.

[62] Maćkiewicz, A. and Ratajczak, W. (1993). Principal components analysis (pca). *Computers & Geosciences*, 19(3):303–342.

[63] McIntosh, A. R. and Lobaugh, N. J. (2004). Partial least squares analysis of neuroimaging data: Applications and advances. *NeuroImage*, 23:S250–S263.

[64] McKeown, M. J., Hansen, L. K., and Sejnowsk, T. J. (2003). Independent component analysis of functional mri: what is signal and what is noise? *Current opinion in neurobiology*, 13(5):620–629.

[65] Metzger, M., Dukic, S., McMackin, R., Giglia, E., Mitchell, M., Bista, S., Costello, E., Peelo, C., Tadjine, Y., Sirenko, V., et al. (2024). Functional network dynamics revealed by eeg microstates reflect cognitive decline in amyotrophic lateral sclerosis. *Human Brain Mapping*, 45(1):e26536.

[66] Nasseroleslami, B., Dukic, S., Broderick, M., Mohr, K., Schuster, C., Gavin, B., McLaughlin, R., Heverin, M., Vajda, A., Iyer, P. M., et al. (2019). Characteristic increases in eeg connectivity correlate with changes of structural mri in amyotrophic lateral sclerosis. *Cerebral cortex*, 29(1):27–41.

[67] Nastase, S. A., Liu, Y.-F., Hillman, H., Norman, K. A., and Hasson, U. (2020). Leveraging shared connectivity to aggregate heterogeneous datasets into a common response space. *NeuroImage*, 217:116865.

[68] Norman, K. A., Polyn, S. M., Detre, G. J., and Haxby, J. V. (2006). Beyond mind-reading: multi-voxel pattern analysis of fmri data. *Trends in Cognitive Sciences*, 10(9):424–430.

[69] Norris, F., Shepherd, R., Denys, E., Kwei, U., Mukai, E., Elias, L., Holden, D., and Norris, H. (1993). Onset, natural history and outcome in idiopathic adult motor neuron disease. *Journal of the neurological sciences*, 118(1):48–55.

[70] Northall, A., Doehler, J., Weber, M., Tellez, I., Petri, S., Prudlo, J., Vielhaber, S., Schreiber, S., and Kuehn, E. (2024). Multimodal layer modelling reveals in vivo pathology in amyotrophic lateral sclerosis. *Brain*, 147(3):1087–1099.

[71] Northall, A., Doehler, J., Weber, M., Vielhaber, S., Schreiber, S., and Kuehn, E. (2023). Layer-specific vulnerability is a mechanism of topographic map aging. *Neurobiology of aging*, 128:17–32.

[72] Odierna, G. L., Vucic, S., Dyer, M., Dickson, T., Woodhouse, A., and Blizzard, C. (2024). How do we get from hyperexcitability to excitotoxicity in amyotrophic lateral sclerosis? *Brain*, 147(5):1610–1621.

[73] Pavey, N., Hannaford, A., van den Bos, M., Kiernan, M. C., Menon, P., and Vucic, S. (2024). Distinct neuronal circuits mediate cortical hyperexcitability in amyotrophic lateral sclerosis. *Brain*, 147(7):2344–2356.

[74] Penfield, W. and Rasmussen, T. (1950). The cerebral cortex of man; a clinical study of localization of function.

[75] Penny, W. D., Friston, K. J., Ashburner, J. T., Kiebel, S. J., and Nichols, T. E. (2011). *Statistical parametric mapping: the analysis of functional brain images*. Elsevier.

[76] Petitet, P., Spitz, G., Emir, U. E., Johansen-Berg, H., and O'Shea, J. (2021). Age-related decline in cortical inhibitory tone strengthens motor memory. *Neuroimage*, 245:118681.

[77] Pleger, B., Wilimzig, C., Nicolas, V., Kalisch, T., Ragert, P., Tegenthoff, M., and Dinse, H. R. (2016). A complementary role of intracortical inhibition in age-related tactile degradation and its remodelling in humans. *Scientific reports*, 6(1):27388.

[78] Proudfoot, M., Bede, P., and Turner, M. R. (2019). Imaging cerebral activity in amyotrophic lateral sclerosis. *Frontiers in neurology*, 9:1148.

[79] Proudfoot, M., Colclough, G. L., Quinn, A., Wuu, J., Talbot, K., Benatar, M., Nobre, A. C., Woolrich, M. W., and Turner, M. R. (2018). Increased cerebral functional connectivity in als: a resting-state magnetoencephalography study. *Neurology*, 90(16):e1418–e1424.

[80] Quinn, C., Edmundson, C., Dahodwala, N., and Elman, L. (2020). Reliable and efficient scale to assess upper motor neuron disease burden in amyotrophic lateral sclerosis. *Muscle & nerve*, 61(4):508–511.

[81] Raimondo, L., Priovoulos, N., Passarinho, C., Heij, J., Knapen, T., Dumoulin, S. O., Siero, J. C., and van der Zwaag, W. (2023). Robust high spatio-temporal line-scanning fmri in humans at 7t using multi-echo readouts, denoising and prospective motion correction. *Journal of Neuroscience Methods*, 384:109746.

[82] Ravits, J. M. and La Spada, A. R. (2009). Als motor phenotype heterogeneity, focality, and spread: deconstructing motor neuron degeneration. *Neurology*, 73(10):805–811.

[83] Roski, C., Caspers, S., Langner, R., Laird, A. R., Fox, P. T., Zilles, K., Amunts, K., and Eickhoff, S. B. (2013). Adult age-dependent differences in resting-state connectivity within and between visual-attention and sensorimotor networks. *Frontiers in aging neuroscience*, 5:67.

[84] Roski, C., Caspers, S., Lux, S., Hoffstaedter, F., Bergs, R., Amunts, K., and Eickhoff, S. B. (2014). Activation shift in elderly subjects across functional systems: an fmri study. *Brain Structure and Function*, 219:707–718.

[85] Rubio, M. A., Herrando-Grabulosa, M., and Navarro, X. (2022). Sensory involvement in amyotrophic lateral sclerosis. *International journal of molecular sciences*, 23(24):15521.

[86] Ruitenberg, M. F., Cassady, K. E., Reuter-Lorenz, P. A., Tommerdahl, M., and Seidler, R. D. (2019). Age-related reductions in tactile and motor inhibitory function start early but are independent. *Frontiers in Aging Neuroscience*, 11:193.

[87] Schneider, F. C., Pailler, M., Faillenot, I., Vassal, F., Guyotat, J., Barral, F.-G., and Boutet, C. (2016). Presurgical assessment of the sensorimotor cortex using resting-state fmri. *American Journal of Neuroradiology*, 37(1):101–107.

[88] Schweizer, R., Braun, C., Fromm, C., Wilms, A., and Birbaumer, N. (2001). The distribution of mislocalizations across fingers demonstrates training-induced neuroplastic changes in somatosensory cortex. *Experimental Brain Research*, 139:435–442.

[89] Schweizer, R. and Frahm, J. (2009). High-resolution mapping of finger representations in human primary somatosensory cortex using fmri in 10 min. *NeuroImage*, 47:S131.

[90] Schweizer, R., Voit, D., and Frahm, J. (2008). Finger representations in human primary somatosensory cortex as revealed by high-resolution functional mri of tactile stimulation. *Neuroimage*, 42(1):28–35.

[91] Seabold, S. and Perktold, J. (2010). Statsmodels: econometric and statistical modeling with python. *SciPy*, 7(1):92–96.

[92] Seeley, W. W., Crawford, R. K., Zhou, J., Miller, B. L., and Greicius, M. D. (2009). Neurodegenerative diseases target large-scale human brain networks. *Neuron*, 62(1):42–52.

[93] Smith, S. M., Hyvärinen, A., Varoquaux, G., Miller, K. L., and Beckmann, C. F. (2014). Group-pca for very large fmri datasets. *Neuroimage*, 101:738–749.

[94] Sorrentino, P., Rucco, R., Jacini, F., Trojsi, F., Lardone, A., Baselice, F., Femiano, C., Santangelo, G., Granata, C., Vettoliere, A., et al. (2018). Brain functional networks become more connected as amyotrophic lateral sclerosis progresses: a source level magnetoencephalographic study. *NeuroImage: Clinical*, 20:564–571.

[95] Stegmann, G. M., Hahn, S., Liss, J., Shefner, J., Rutkove, S., Shelton, K., Duncan, C. J., and Berisha, V. (2020). Early detection and tracking of bulbar changes in als via frequent and remote speech analysis. *NPJ digital medicine*, 3(1):132.

[96] Stelzer, J., Buschmann, T., Lohmann, G., Margulies, D. S., Trampel, R., and Turner, R. (2014). Prioritizing spatial accuracy in high-resolution fmri data using multivariate feature weight mapping. *Frontiers in neuroscience*, 8:66.

[97] Trojsi, F., Di Nardo, F., D'Alvano, G., Caiazzo, G., Passaniti, C., Mangione, A., Sharbafshaaer, M., Russo, A., Silvestro, M., Siciliano, M., et al. (2023). Resting state fmri analysis of pseudobulbar affect in amyotrophic lateral sclerosis (als): motor dysfunction of emotional expression. *Brain imaging and behavior*, 17(1):77–89.

[98] Trojsi, F., Monsurro, M. R., Esposito, F., and Tedeschi, G. (2012). Widespread structural and functional connectivity changes in amyotrophic lateral sclerosis: insights from advanced neuroimaging research. *Neural Plasticity*, 2012(1):473538.

[99] Turek, J. S., Ellis, C. T., Skalaban, L. J., Turk-Browne, N. B., and Willke, T. L. (2018). Capturing shared and individual information in fmri data. In *2018 IEEE International Conference on Acoustics, Speech and Signal Processing (ICASSP)*, pages 826–830. IEEE.

[100] Uğurbil, K., Xu, J., Auerbach, E. J., Moeller, S., Vu, A. T., Duarte-Carvajalino, J. M., Lenglet, C., Wu, X., Schmitter, S., Van de Moortele, P.-F., Strupp, J., Sapiro, G., De Martino, F., Wang, D., Harel, N., Garwood, M., Chen, W., Kim, S.-G., Garwood, M., and Van de Moortele, P.-F. (2013). Pushing spatial and temporal resolution for functional and structural mri in the 7 tesla human connectome project. *NeuroImage*, 80:80–104.

[101] van den Bos, M. A., Geevasinga, N., Higashihara, M., Menon, P., and Vucic, S. (2019). Pathophysiology and diagnosis of als: insights from advances in neurophysiological techniques. *International journal of molecular sciences*, 20(11):2818.

[102] van den Bos, M. A., Menon, P., Pavey, N., Higashihara, M., Kiernan, M. C., and Vucic, S. (2024). Direct interrogation of cortical interneuron circuits in amyotrophic lateral sclerosis. *Brain*, page awae317.

[103] Verstraete, E. and Foerster, B. R. (2015). Neuroimaging as a new diagnostic modality in amyotrophic lateral sclerosis. *Neurotherapeutics*, 12(2):403–416.

[104] Verstraete, E., Van Den Heuvel, M. P., Veldink, J. H., Blanken, N., Mandl, R. C., Hulshoff Pol, H. E., and van den Berg, L. H. (2010). Motor network degeneration in amyotrophic lateral sclerosis: a structural and functional connectivity study. *PloS one*, 5(10):e13664.

[105] Verstraete, E., Veldink, J. H., Hendrikse, J., Schelhaas, H. J., Van Den Heuvel, M. P., and Van Den Berg, L. H. (2012). Structural mri reveals cortical thinning in amyotrophic lateral sclerosis. *Journal of Neurology, Neurosurgery & Psychiatry*, 83(4):383–388.

[106] Wang, L., Zhang, Z., Okada, T., Li, C., Chen, D., Funahashi, S., Wu, J., and Yan, T. (2021). Population receptive field characteristics in the between-and within-digit dimensions of the undominant hand in the primary somatosensory cortex. *Cerebral Cortex*, 31(10):4427–4438.

[107] Worsley, K. J. (1994). Local maxima and the expected euler characteristic of excursion sets of χ 2, f and t fields. *Advances in Applied Probability*, 26(1):13–42.

[108] Xie, M., Pallegar, P. N., Parusel, S., Nguyen, A. T., and Wu, L.-J. (2023). Regulation of cortical hyperexcitability in amyotrophic lateral sclerosis: focusing on glial mechanisms. *Molecular neurodegeneration*, 18(1):75.

[109] Yacoub, E., Harel, N., and Uğurbil, K. (2008). High-field fmri unveils orientation columns in humans. *Proceedings of the National Academy of Sciences*, 105(30):10607–10612.

[110] Yang, J., Huber, L., Yu, Y., Chai, Y., Khojandi, A., and Bandettini, P. A. (2019). High-resolution fmri maps of columnar organization in human primary somatosensory cortex. In *Proc Intl Soc Mag Reson Med*, volume 27, page 0617.

[111] Yoganathan, K., Dharmadasa, T., Northall, A., Talbot, K., Thompson, A. G., and Turner, M. R. (2025). Asymmetry in amyotrophic lateral sclerosis: clinical, neuroimaging and histological observations. *Brain*, page awaf121.

[112] Yushkevich, P. A., Gao, Y., and Gerig, G. (2016). Itk-snap: An interactive tool for semi-automatic segmentation of multi-modality biomedical images. In *2016 38th annual international conference of the IEEE engineering in medicine and biology society (EMBC)*, pages 3342–3345. IEEE.

[113] Zanette, G., Tamburin, S., Manganotti, P., Refatti, N., Forgione, A., and Rizzuto, N. (2002). Changes in motor cortex inhibition over time in patients with amyotrophic lateral sclerosis. *Journal of neurology*, 249:1723–1728.

[114] Zhang, H., Chen, P.-H., Chen, J., Zhu, X., Turek, J. S., Willke, T. L., Hasson, U., and Ramadge, P. J. (2016). A searchlight factor model approach for locating shared information in multi-subject fmri analysis. *arXiv preprint arXiv:1609.09432*.

[115] Zhou, C., Hu, X., Hu, J., Liang, M., Yin, X., Chen, L., Zhang, J., and Wang, J. (2016). Altered brain network in amyotrophic lateral sclerosis: a resting graph theory-based network study at voxel-wise level. *Frontiers in neuroscience*, 10:204.

[116] Zuppichini, M. D., Hamlin, A. M., Zhou, Q., Kim, E., Rajagopal, S., Beltz, A. M., and Polk, T. A. (2024). Gaba levels decline with age: a longitudinal study. *Imaging Neuroscience*, 2:1–15.